



University
of Glasgow

Hay, Rebecca (2017) *Optimising optical tweezers for tracking and force measurement experiments*. PhD thesis.

<http://theses.gla.ac.uk/8624/>

Copyright and moral rights for this work are retained by the author

A copy can be downloaded for personal non-commercial research or study,
without prior permission or charge

This work cannot be reproduced or quoted extensively from without first
obtaining permission in writing from the author

The content must not be changed in any way or sold commercially in any
format or medium without the formal permission of the author

When referring to this work, full bibliographic details including the author,
title, awarding institution and date of the thesis must be given

Enlighten:Theses
<http://theses.gla.ac.uk/>
theses@gla.ac.uk

Optimising Optical Tweezers for Tracking and Force Measurement Experiments

Rebecca Hay

A thesis submitted in fulfilment of the requirements for the degree of
Doctor of Philosophy

School of Physics and Astronomy
College of Science and Engineering
University of Glasgow

December 2017

Abstract

Optical Tweezers are a useful tool in many aspects of biology, including cell manipulation and microrheology [1, 2]. They are often used as piconewton force transducers, and are an effective tool for measuring forces acting upon optically trapped particles [3–7]. To measure such forces, knowledge of the displacement of the particle from the trap centre is always needed. However, due to Brownian motion, a trapped particle is constantly moving and never at rest. In this case, one must track a bead over a set time, so as to gain an average displacement.

In this thesis, we have improved and optimised this tracking procedure for biological samples in different ways.

In Chapter 1 we discuss how Optical Tweezers work, how they are set up, and how we measure forces using them.

In Chapter 2 we redesign a commercial Optical Tweezer Product to improve tracking data results. We also incorporate fluorescence imaging using a compact, low cost, LED illumination source.

In Chapter 3 we combine fluorescence microscopy with state of the art Scientific cameras, to increase tracking frame rates and potentially improve our tracking data

of fluorescent stained cells. This was part of a collaboration, where I helped to build the setup, took the data (using programs produced by one of my collaborators), and was part of the team to analyse it.

In Chapter 4, we look at Low Reynolds number environments and discuss the benefits of viscous forces, and how it may be possible to make non-invasive, less harmful traps for biological samples. Again, this was part of a collaboration, where I was in charge of the experimental part. Here, I built in the static tweezer trap into a tweezer system, took position data and analysed it. A collaborator took control of analysing velocity data.

Finally, in Chapter 5, we measure the accuracy of tracking in three dimensions using a stereomicroscope, by placing a Spatial Light Modulator (SLM) at the Fourier plane in the imaging arm. Again, this was a collaboration. I designed and manufactured the illumination head, helped design an acquisition program, and took the data.

We discuss how all of these could optimise and advance the tracking of optically trapped particles, especially biological samples. Despite the obvious applications in biology, to allow a fair evaluation of the different tracking techniques, all of our experiments used samples of spherical beads, as they have known specifications, including fluorescence excitation and emission wavelengths, size, and amount of fluorophore stain.

Contents

Abstract	i
Contents	iii
List of Figures	v
Acknowledgements	xiv
Declaration of Authorship	xvi
Publications	xvii
1 Introduction	1
1.1 Theory	3
1.1.1 Optical Tweezers - Ray Optics	3
1.1.2 Optical Tweezer Set Up	8
1.1.3 Holographic Optical Tweezers (HOT)	9
1.1.4 Force Measurements Using Optical Tweezers	15
1.1.5 Particle Position Tracking	20
1.2 Objectives of the Thesis	23
1.2.1 Structure of the Thesis	23
2 The Redesign of the Meadowlark Cube	25
2.1 Background	26
2.2 Optical Configurations of the two HOT Designs	30
2.3 Conclusion	36
3 Comparing EMCCD and sCMOS cameras for low-light high-speed position tracking of optically trapped fluorescing particles	37
3.1 Introduction	38
3.2 Method	42
3.2.1 Experimental setup	42
3.2.2 Data Acquisition and Analysis	44

3.3	Results	47
3.4	Discussion	51
3.4.1	Validation by comparing fluorescence tracking to brightfield	54
3.5	Conclusion	55
4	‘Lissajous-like’ trajectories in optical tweezers due to the competition between optical elastic forces and hydrodynamic interactions	58
4.1	Introduction	60
4.1.1	The Langevin Equation	63
4.2	Experimental Method	66
4.3	Results	69
4.3.1	Experimental	69
4.3.2	Simulated	75
4.4	Discussion	77
4.4.1	Energy Transfer between the Probe and Actuator	80
4.5	Conclusions	82
5	Four directional stereo-microscopy for 3D particle tracking with real-time error evaluation	84
5.1	Introduction	85
5.2	Methods	91
5.2.1	Experimental set-up	91
5.2.2	Using parallax calculations to find 3D position coordinates	93
5.2.3	Data Acquisition	99
5.3	Results	101
5.4	Discussion	102
5.5	Conclusion	108
6	Conclusions	110
6.1	Future work	115

List of Figures

1.1	When the bead is displaced from the centre of the optical trap, the change in the direction of the refracted light pushes the bead back towards the equilibrium position. a) An example ray generating a lateral component of the optical trapping force. b) Example rays generating an axial component of the trapping force.	4
1.2	An optical trapping force can be described like a spring, with a spring constant k_{trap} . A trap has an optical restoring force, F_{trap} . The trap's restoring force acting on a trapped bead follows Hookes' law and is proportional to the distance the bead is from the centre of the trap (Δx). Hookes Law can only be used for small displacements from equilibrium position (~ 1 radius of the beam width). Note that the trap centre is slightly above the focus of the beam.	6
1.3	Schematic of a generic Optical Tweezer setup with a steerable mirror in the Fourier plane used to control the trap position. It is based upon an inverted microscope. The laser beam is expanded, using a 4f beam expander. It then reaches the steerable mirror, which allows movement of the trap position. Its then travels through a Fourier lens and travels through a Dichroic filter, and reaches the tube lens. The beam is then focused in the objective lens, and a trap is formed in the sample. The sample is then imaged, with light travelling back through the Objective and Tube lenses. It is then reflected at the Dichroic, reaches an image plane before being re-imaged again through a 4f setup.	10
1.4	Schematic of a generic Holographic Optical Tweezer (HOT) setup. The steerable mirror (as seen in Figure 1.3) has been replaced by a Spatial Light Modulator (SLM), a grey scale liquid crystal display that projects hologram patterns. This allows the Optical Trap to be shifted in all three dimensions, as prisms do, with ease computationally. . . .	11
1.5	Example hologram images created using the 'grating and lenses' algorithm. a) Hologram to create and position the optical trap veritcally. b) hologram to create and position the optical trap horizontally. c) mod. 2π addition of the above holograms to create and position one optical trap laterally. d) Complex addition of the above holograms to create two independent optical traps. Also shown in c) and d) are the corresponding Fourier transform, giving the trap arrangements in each case.	13

1.6	An example of a power spectrum for x and y tracking data in bright-field, with low noise in the system. Note that the curve is similar to a Lorentzian curve, and so reading a corner frequency, and thus finding the optical trap stiffness, can be done with ease.	17
1.7	An example of an autocorrelation function for x tracking data in fluorescence, with noise in the system. This data is taken from Chapter 2. Note that the fit is straight up until the fourth data point, before the gradient changes. This is when noise begins to show. At this point, the noise in the system should be considered and factored in. Information about the value of κ is taken from the decay of the slope.	18
1.8	An example of the intensity of an image, in the x axis, through the thresholding process. A threshold is placed on the original intensity chart, with every intensity below the threshold set to zero. However, noise can result in large fluctuations at the points where the threshold is applied. A solution is to subtract the background from the original intensity, leading to no intensity within the image to be less than zero, which then gives our new thresholded intensity. The position of the centre of the particle is then at the centre of this new intensity chart.	21
2.1	(a) is an image taken from the Cube of a focussed spot without any aberration correction. (b) is the hologram placed on the SLM to correct for the aberration. (c) is an image taken with the Cube with the aberration hologram on the SLM [8]. This aberration correction hologram is no longer required with the new Cuboid design, reducing cross talk and ghost traps.	28
2.2	Schematic of the original Meadowlark Cube. The laser is expanded to fill the SLM. One of the beam expander lenses is then reused as the Fourier lens, leading to aberrations, causing the degrading of the traps before aberration corrections are added to the SLM. After the Fourier lens the laser light is coupled into the microscope with a dichotic filter. A high speed camera allows accurate position tracking of trapped objects.	31
2.3	3D models of the original Meadowlark Cube tweezer system. With it being only one cubic foot in size, yet still allowing multiple HOT trapping, it's main selling point is that it is compact, stand-alone and portable. However, there are aberration issues due to using the same lens as both a beam expander and a Fourier lens, so that the product can stay portable. Figure from Reference [8]. A space for a filter holder is left to allow filters to be added to epi-fluorescence illumination.	32
2.4	Schematic of the new Cuboid. The laser is expanded to fill the SLM. There are two distinct lenses in place of one for the beam expansion and the Fourier lens. After the Fourier lens the laser light is coupled into the microscope with a dichotic filter. A reconfigurable filter holder is found in the camera arm, allowing the use of epi-illumination for Fluorescence microscopy and imaging.	33

2.5	Live image of two optically trapped fluorescing $1.5\mu\text{m}$ silica beads taken from the imaging and data tracking Labview program. See that the beads are circularly symmetrical in shape. Here we see a highly fluorescing bead and a dimmer fluorescing bead. This is due to the dimmer bead performing less excitation, either due to a lack of fluorescence coating or less blue excitation light reaching the dimmer bead. This image was taken using the Dalsa Genie camera running at a frame rate of 18 frames per second.	35
3.1	Schematic of the setup used. The laser output beam is expanded, slightly overfilling the aperture of the Spatial Light Modulator (SLM) (Boulder nonlinear optics, XY series 512x512 pixels). After the Fourier lens, the light diffracted by the SLM is re-imaged onto the back focal plane of the objective lens, 100x 1.3NA, (Nikon, Plan-Fluor), which focuses the trapping laser beam in the sample cell. The fluorescence excitation source is a blue LED (Luxeon Rebel) filtered with a 485/10 nm filter and is coupled through the objective using a dichroic beam splitter. Within the same filter cube a 510/10nm filter ensures that only the fluorescence is detected. We used both sCMOS (Hamamatsu ORCA-Flash4.0 V2+) and EMCCD (Andor iXon3 897) cameras to image the fluorescence. A camera port selector determines which camera is used.	43
3.2	Photo of experimental setup.	44
3.3	An example of the x and y displacement data for a 4s interval of data at the highest fluorescence intensity (5650 photons/frame) for the EMCCD camera (blue) and the sCMOS camera (red). The approximation of noise, and hence the error on each x, y position measurement is 10.5nm. This is approximately a factor of 10 larger than the error of from the more general brightfield tracking, which usually has errors of around 1nm. This is due to the limited number of photons in each image.	46
3.4	Autocorrelation against time graphs for the sCMOS and the EMCCD camera for different fluorescent levels. The x-axis is time (measured in seconds). At higher fluorescent levels, the cameras give similar results for the autocorrelation gradients and y-intercepts. At lower fluorescent levels the cameras are in overall agreement for what concerns the y-intercepts but not for the gradients. The error bars are one standard deviation over 10 samples of 4 second durations (equating to 1000 frames)	48

- 3.5 Graphs to show how the average autocorrelation gradients (left) and y-intercepts (right) change with respects to different fluorescent intensities, as well as their standard deviations. What we would hope to see is both a constant y-intercept and gradient, as the trap power and stiffness is constant throughout the experiment. What we find is that at higher fluorescence intensities (more than 3000 photons/frame), the two cameras yield autocorrelations that are in close agreement with each other, both in terms of their y-axis intercepts and gradients. This changes at lower intensities where it is evidence to suggest that the sCMOS camera slightly underperforms the EMCCD especially in terms of the gradient of the autocorrelation, until at the lowest intensity it proved impossible using the sCMOS camera to record images of sufficient quality in which to run standard centroid tracking algorithms, therefore no autocorrelation could be calculated. At low intensities the EMCCD camera images were of a sufficient quality to measure the standard deviation of the bead motion, but the gradient of the autocorrelation was subject to significant uncertainty. 49
- 3.6 Single frames and summed successive co-registered frames images (left and right respectively) at a fluorescence level of ~ 5650 photons/frame. Images at the corner of the summed image represent the intensity at the cross-section of the summed image (the dotted line). The summed images appear circularly symmetric, with a slight reduction in intensity at the centre (as seen in the intensity cross-sections) due to the bead being surface labelled. The central reduction in intensity should therefore not affect the numerical calculation of the centroid position. 51
- 3.7 The power spectra produced by the tracking data for the EMCCD camera (above) and the sCMOS camera (below) at a fluorescence level of approximately 4690 photons/frame. Note that the the spectra are very noisy, and although not impossible, much more difficult to read a corner frequency than a gradient on an autocorrelation. 52
- 3.8 Autocorrelation function obtained from 4s interval of data (1000 frames) using the EMCCD camera at an intensity of 4690 photons/frame. The number of data points depends on the time taken between camera frames. The gradient of the autocorrelation is determined by fitting to the first 4 data points. If more (noise) data points were used for the fit, the gradient would be skewed. 53
- 3.9 Autocorrelation against time graphs for the sCMOS with fluorescence (at a photon level of >5000 photons/frame) and brightfield centroid tracking data. Again, a 40s dataset was divided into 4s intervals, the autocorrelations being calculated for each interval and then averaged over each dataset. The camera gave similar results for the fluorescence and brightfield tracking. 56

- 4.1 Examples of the two main ‘actuator’ bead paths with respect to their corresponding ‘probes’. The left shows the circular non time-reversal (the path going forward in time is not identical to the path that would go back in time) symmetric actuator path. The right shows the horizontal time-reversal (the paths going forward in time and backwards in time are identical) symmetric actuator path. 63
- 4.2 Schematic showing how a trajectory of a microsphere is calculated at each simulation time-step from the balance of external forces, F_{ext} (such as hydrodynamic and stochastic thermal forces), optical forces, F_{opt} , and frictional forces, $F_{friction}$ 65
- 4.3 Schematic of the dual beam holographic optical tweezers system. Our optical tweezers system is built around a custom-made inverted microscope with a Zeiss halogen illumination module (100 Watt). The holographic actuator trap is created by expanding a diode pumped solid state (DPSS) infra-red 1064 nm wavelength laser beam to overfill a nematic liquid crystal spatial light modulator (SLM) (BNS XY series, 512 x 512 pixels, 200Hz frame-rate). The SLM is placed in the Fourier plane of the sample and telescopically re-imaged onto and overfilling the back aperture of the objective lens (Nikon 100x oil immersion, 1.3 NA) using a Fourier lens (L1) of 250 mm focal length and a tube lens of focal length 100 mm. The single beam trap is provided by a green DPSS 532 nm wavelength laser. Its position can be manually controlled using a kinematic mirror mount, and the beam also overfills the back aperture of the objective lens. The sample is viewed using a high-speed CMOS camera (Dalsa Genie gigabit ethernet), and any reflected infra-red and green laser light is filtered out. The top left inset shows a schematic of the relative optical trap positions and trajectories within the sample. 67
- 4.4 Experimentally measured probe microsphere trajectories when subjected to a time-reversible flow-field. (a) The trajectory of the probe over a single time-reversal symmetric actuator cycle. (b) and (e) 2D occupancy histograms showing the number of visits the probe made to each 10 nm wide bin over the course of 100 actuator cycles. The white scale bars represent 100 nm. (b) is the first half of the cycle, (e) is the second half of the cycle. (c) and (f) The average drift velocity of the probe as it passes through each 10 nm x 10 nm histogram bin. (d) and (g) The magnitude and direction of the drift velocity of the probe bead. 70
- 4.5 Experimentally measured probe microsphere trajectories when subjected to a non-time-reversible flow-field. (a) The trajectory of the probe over a single non time-reversal symmetric actuator cycle. (b) A 2D occupancy histogram showing the number of visits the probe made to each 10 nm wide bin over the course of 100 actuator cycles. The white scale bar represents 100 nm. (c) The average drift velocity of the probe as it passes through each 10 nm x 10 nm histogram bin. (d) The magnitude and direction of the drift velocity of the probe bead. 71

- 4.6 Experimental trajectories for (a) horizontal oscillatory actuator motion, (b) oscillatory actuator motion with x y displacement ratio equal to 5, and (c) circular motion respectively. ‘x’ on the experimental trajectory graphs represents the probe trap position. When looking at (a) we see a ‘figure of eight’ probe trajectory, where the probe moves in both x and y, even though, the actuator only moves in x. It moves a distance in x of around $1\mu\text{m}$, and in y of around $0.3\mu\text{m}$. When looking at (b), we see one of the lobes produced in (a) reduced in size. This happens until the lobe disappears entirely, to form the ‘D’ shape, as seen in (c). Again the horizontal distance of around $1\mu\text{m}$ in x, but now a $2\mu\text{m}$ in y. 73
- 4.7 Averaged experimental trajectory of a trapped probe being driven by an actuator travelling with circular motion are at the same height of 10 (top left), 15 (top right), 20 (bottom left) and $25\mu\text{m}$ (bottom right) from the surface. Colour scale represents the velocity. Grey line represents a single trajectory before averaging. The average was taken over 200 trajectories. It appears that the trajectory get larger when it is moved away from the surface. This is due to less surface friction acting upon the bead. 74
- 4.8 Averaged experimental trajectory of a trapped probe being driven by an actuator travelling with circular motion are at the same height of 10 (top left), 15 (top right), 20 (bottom left) and $25\mu\text{m}$ (bottom right) from the surface. Colour scale represents the velocity. Grey line represents a single trajectory before averaging. The average was taken over 200 trajectories. Again, it appears that when the probe moves away from the sample cell’s surface, the trajectory get larger. Again, this is due to less surface friction acting upon the bead. 75
- 4.9 Averaged probe trajectories where the actuator paths are at different locations with respect to the probe. (a) Illustration of the actuator position and path with a circular system configuration with respects to the probe bead and trap (b) the corresponding experimental probe trajectories, with information about the speed the probe is travelling, using the colour velocity scale to the right of the charts. Note that all probe trajectories are ‘D’ in shape, only with some tilting occurring when the actuator trajectory is placed either to the left or the right of the probe. We find that the bead travels quickest when travelling in the y-direction and no movement in the x-direction. 76
- 4.10 Simulated trajectories of the probe with respects to actuator paths. The left probe path corresponds to the time-reversal symmetric actuator trajectory (horizontal sinusoidal motion) and the right probe path corresponds to the non time-reversal actuator trajectory (circular motion). The zero point on the graphs corresponds to the trap centre. Colour chart corresponds to the beads speed during the trajectory, here the bead is travelling at its slowest when the path is blue, and quickest when its path is red. 77

4.11	Illustrations showing the relative positions of the probe microspheres with respects to the position and movement of the actuator in its path for (a) the time-reversal symmetric actuator trajectory (horizontal sinusoidal motion) and (b) non time-reversal symmetric actuator trajectory (circular sinusoidal motion). Once again, for clarity, the relative size of the probe trajectory has been exaggerated compared to both the probe size, and the actuator trajectory.	78
4.12	Simulation of the accumulated potential energy of the probe trap in the absence of Brownian motion for the (a) actuator in circular motion (non time-reversible symmetric) case and (b) actuator in periodic horizontal motion (time-reversible symmetric) case. Each case shows the evolution of the energy stored in the system when the probe is initially positioned at rest at the centre of the trap. Work is done on the bead in the white stripes, and energy is released by the bead in the blue stripes.	81
5.1	By illuminating the sample from different directions, multiple images are produced, each individual image corresponding to one illumination direction. When an object moves up and down in the z direction of the sample, the sample appears to move in the x and y direction in the corresponding 2D images.	87
5.2	Stereo-microscopy is a technique that enables a sample to be imaged from two directions simultaneously, allowing the tracking of microscopic objects in three dimensions. This can be done by either one illumination and two objective lenses or two illuminations and one objective lens. By illuminating the sample from different directions, multiple images are produced, each individual image corresponding to one illumination direction.	89
5.3	Layout of previous Stereomicroscopy system including wedge prisms to separate the superimposed images and to send them in different directions. This works best for two illumination directions, so is convenient to use an SLM so that we can use more illuminators.	90
5.4	(a) Examples of the illuminator heads designed with Sketchup and 3D printed using the Ultimaker 2.0 3D printer. Note that the three heads cover a range of angles. (b) Example of one illuminator head holding the four optical fibres used as light guides.	93

5.5	Schematic of the optical layout. It is based on a transmission light microscope with an SLM placed in the Fourier plane of the image. The sample is illuminated from four directions with red LEDs (Luxeon Rebel, peak emission at 636 nm) coupled into light guides. Light transmitted through the sample is collected by the objective lens (Zeiss Plan-Neofluar, 100 \times , 1.3 NA). The polarising beamsplitter selects light of the correct polarisation for the SLM. An iris in a conjugate image plane controls the field-of-view to ensure all images fit adjacently onto the camera. A narrowband filter (635 nm / 10 nm) minimises dispersion of the images when diffracted from the SLM. The polarising beamsplitter is also used to couple in a single beam optical tweezer ($\lambda = 635$ nm). The focal lengths of the lenses are: L1 = 120 mm, L2 = 150 mm and L3 = 200 mm.	94
5.6	a) Illustration of the four illumination paths through the system. Here the SLM is shown as a transmissive element rather than reflective, for clarity. The SLM diffracts light corresponding to each illumination direction to a separate region of the camera sensor. (b) A representative phase pattern on the SLM. (c) The resulting image on the camera. Undiffracted zero-order light is sent to the central region. The scaling is 73.5 nm per pixel.	95
5.7	The relationship between micro-bead's 3D position to its projected image on the focal plane. The measured motion of the image parallel to x in the focal plane is given by $x_m = A + \delta x$, where $A = \delta z \tan \phi \cos \theta$. Likewise the measured motion of the image parallel to y is given by $y_m = B + \delta y$, where $B = \delta z \tan \phi \sin \theta$	98
5.8	Images of the front panel of the Labview program. The left shows the illumination intensity control and the full image viewed by the CMOS camera. The right shows the four separated first order images (indicated by the green square in the left image) and the tracking setup controls. These controls include the illuminators' azimuthal and polar angles, tracking area test size, and a tracking off and on switch. . . .	100
5.9	Accuracy of 3D particle tracking using stereo-microscopy. Top left, top right and bottom left show traces of the measured x , y and z positions respectively. In each case the two independent measurements (green and blue lines) are overlaid by subtracting their mean positions. The red trace indicates the difference between the measurements. Bottom right shows a zoom in on the highlighted region of the bottom left to more clearly observe the similarity of the measurements.	101
5.10	Accuracy of 3D particle tracking using stereo-microscopy in each dimension with respects to (a) the level of spatial filtering (aperture size in terms of a percentage of the SLM screen space) and (b) the exposure time of the camera (measured in microseconds).	102

5.11	Accuracy of 3D particle tracking using stereo-microscopy in each dimension depending on each pair of illuminators with respects to the level of spatial filtering (aperture size in terms of a percentage of the SLM screen space) and the exposure time of the camera (measured in microseconds). The top illustration describes each set of illuminator pairs. The pair of opposite illuminators appear to give the more accurate results than each set of orthogonal pairs.	103
5.12	(a) shows a column of four images of a micro-bead at different heights with a spatial filter diameter of 2.5 mm. (b) shows the same micro-bead with a reduced diameter spatial filter. In (b) the images are now more symmetrical, facilitating accurate tracking.	104
5.13	A vertical cross-section through a z -stack of images (200 images recorded at 100 nm height separations) of a $2\ \mu\text{m}$ diameter micro-bead illuminated by a single off axis illuminator. The approximate position of the micro-bead is marked with a dashed white circle. Optimum tracking is achieved by choosing the most symmetrical horizontal plane for centre of symmetry tracking.	106
5.14	Graphs showing the trajectory paths of the tracked $2\ \mu\text{m}$ polystyrene bead in z , with the illuminators at approximately 30 degrees. Here, we have manually moved the stage axially over a large distance in a short period. The left graph corresponds to when the SLM override is switched off, and so the apertures are not changing with respect to the bead position. The right graph has the SLM override switched on, where the SLM is continually updating its apertures to allow the bead to always stay in focus. As with figure 5.10, each case the two independent measurements (green and blue lines) are overlaid. The red trace indicates the difference between the measurements. We see a bigger difference between measurements when the override is switched on.	108

Acknowledgements

This research would not have been made possible without the help and guidance of others. In particular I would like to thank my supervisors Prof. Miles Padgett and Dr. Jonathan Taylor for being good natured, fun and patient - I realise my stupidity and anxiety must have been frustrating at times! I would also like to thank Dr. Graham Gibson for his reassurance, help and many an interesting conversation on experimental ideas relating to design. I would like to thank Dr. Stephen Oxburgh for interesting and entertaining conversations unrelated to Optics, and for the multiple cups of tea he has made for me (apart from that one cup he put salt in as a joke: he will never be forgiven for ruining that cup of tea). I would also like to thank him for thesis template ideas. I would also like to thank Dr. Rair Macedo, for agreeing to be my reading partner and friend four years ago, and for the useful (and useless) chats we have had ever since about our work and pop culture.

I would like to thank my friends and family for supporting me and smiling and nodding during my scientific rants, even when they have not always followed what I have said. I especially want to thank Katherine Rae for putting up with my nonsense and living with me during my PhD, Sam Jackson for always thinking my work was cool, even when I didn't, and Peter Corley for being there to moan at when science

hasn't gone the way I had hoped. Without these people, along with my parents and my close friends from outside of Physics Suzanne Hall, Bryan Jackson and Cassie White, the past four years would have been much tougher.

Finally, this work was supported by the Engineering and Physical Sciences Research Council.

Declaration of Authorship

I hereby declare that this thesis is the result of my own work, except where explicit reference is made to the work of others, and has not been presented in any previous application for a degree at this or any other institution.

Rebecca Hay

Publications

What follows is a list of papers written during my PhD which have been published.

1. R. F. Hay, G. M. Gibson, S. H. Lee, M. J. Padgett and D. B. Phillips, “Four-directional stereo-microscopy for 3D particle tracking with real-time error evaluation”.
2. R. F. Hay, G. M. Gibson, S. H. Simpson, M. J. Padgett and D. B. Phillips,, “Lissajous-like’ trajectories in optical tweezers”. *Optics Express* **23.25**, 31716-31727, 2015
3. M. Dienerowitz, L. V. Cowan, G. M. Gibson, R. Hay, M. J. Padgett and V. R. Phoenix, “Optically Trapped Bacteria Pairs Reveal Discrete Motile Response to Control Aggregation upon Cell - Cell Approach”. *Current microbiology* **69**, 669-674, 2014
4. Y. Zhang, G. M. Gibson, R. Hay, R. W. Bowman and M. J. Padgett, “A fast 3D reconstruction system with a low-cost camera accessory”. *Scientific Reports* **5**, 2015.

“So dense that light bends around her”

Malcolm Tucker (adapted)

Chapter 1

Introduction

Optical Tweezers are a useful tool in many aspects of biology, including cell manipulation and micro-rheology [2, 9, 10]. An example of a microrheology experiment in biology, is the Watts et al. paper ‘Investigating the micro-rheology of the vitreous humor using an optically trapped local probe’ [11]. Here they used a trapped silica bead as a probe to measure the micro-rheology of the vitreous humor, by observing the motion of Brownian motion of the bead.

They are also often used as pico-Newton force transducers, and are an effective tool for measuring forces acting upon optically trapped particles [3–7]. An example of a force transducer in Biology is Dienerowitz et al. paper ‘Optically trapped bacteria pairs reveal discrete motile response to control aggregation upon cell-cell approach’ [1], where forces were measured between 2 microbes in optical trap, to investigate how they interact with each other.

It is possible to trap microscopic particles using coherent focussed light, by which we mean a light source has a constant phase difference and a constant frequency, as long as the object is bigger than the wavelength used [3, 12, 13]. In Optical Tweezers, the coherent light source is a laser beam, which is tightly focussed using a high numerical

aperture objective lens, to a point in the sample [14, 15]. The reason for why this light is able to trap microscopic and nanoscopic particles can be explained via ray optics.

If an external force acting on a particle (cell or bead), it would cause a displacement from the centre of the trap, the extent of the displacement being dependent upon the trap stiffness and the applied force [16, 17]. These displacements and hence forces can be easily measured if the particle is at equilibrium with respect to the centre of the optical trap. However, as the position of the particle is constantly changing due to thermal noise, an accurate measurement of the trap centre requires the positions to be averaged over multiple measurements. Similarly, if this thermal motion is itself to be used for micro-rheology studies, the position of the particle needs to be measured on a time scale which is fast compared to its motion, and thus multiple measurements are needed over short time scales [9, 18]. Measuring these multiple positions can be done using a process called particle tracking. This can be achieved simply, by taking fast frame rate video of the trapped particle, and measuring the position of the bead centre in each frame.

In this chapter, we describe how Optical Tweezers and optical trapping works. We look at the typical Optical Tweezer setup, and describe how Holographic Optical Tweezers differ, and how they can allow much more flexibility in micro-manipulation. We delve into how one can calculate the trap stiffness of an optical trap, and hence calibrate the trap to measure pico-Newton forces. We also detail how centroid video tracking works, which is a key necessity for the work detailed in this thesis. Lastly, we discuss the objectives set out during this research and discuss the structure of the thesis.

1.1 Theory

1.1.1 Optical Tweezers - Ray Optics

Ray optics modelling can provide a good insight into the physics of optical tweezers [3]. Each photon in a laser trapping beam carries linear momentum $\rho=h/\lambda$, where h is Planck's constant and λ is the wavelength of the laser light. This momentum can be changed by two processes: reflection and refraction. Here, the law of reflection states that the angle of reflection is equal to the angle of incidence with respects to the normal plane perpendicular to a reflective surface. This can be written as:

$$\theta_i = \theta_r \quad (1.1)$$

Where θ_i is the angle of incidence and θ_r is the angle of reflection. The law of refraction refers to the change of angle and velocity of a light wave when light moves between different boundaries of different refractive indices, such as light moving between air and glass. This relationship can be described using Snell's law:

$$n_1 \sin\theta_1 = n_2 \sin\theta_2 \quad (1.2)$$

Where n_1 and n_2 are the refractive indices of two media the light is travelling through and θ_1 and θ_2 are the angle of incidence and angle of refraction respectively.

If the laser light hits a transparent particle, reflection and refraction will occur, thus there will be a change in momentum of the light. Newton's second law states that momentum should be conserved, therefore there must be a change in momentum on the particle, and thus a reaction force acting on it. This refracted and reflected light in the ray optics model can be described using the Fresnel Equations.

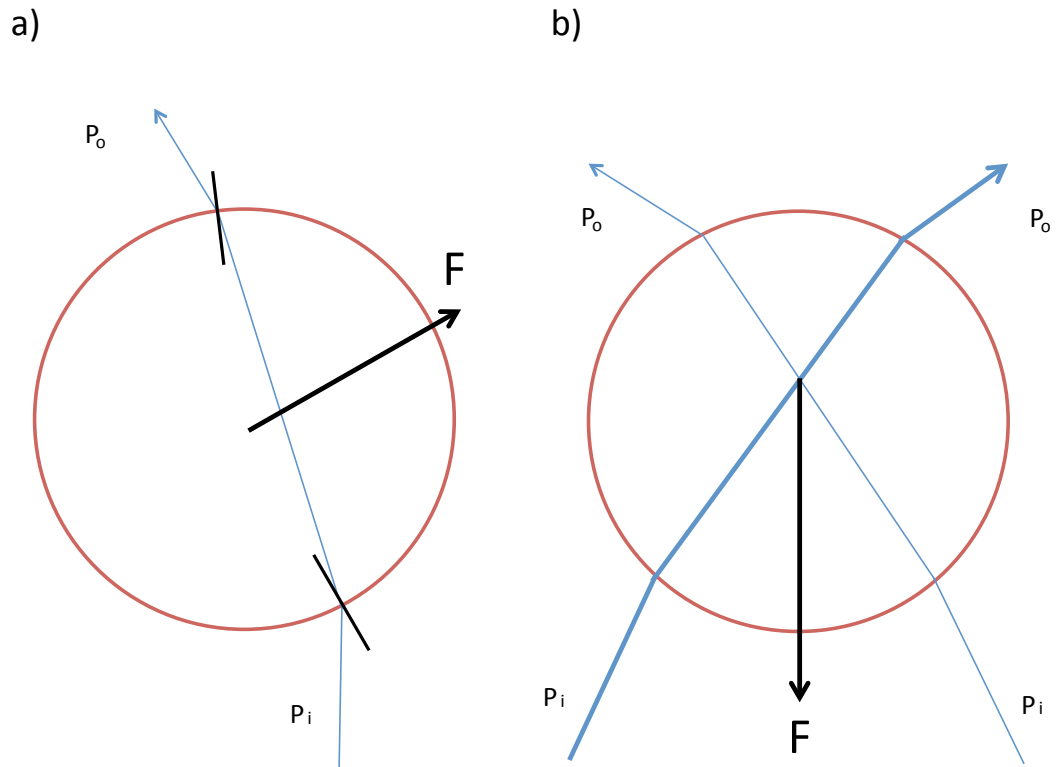


FIGURE 1.1: When the bead is displaced from the centre of the optical trap, the change in the direction of the refracted light pushes the bead back towards the equilibrium position. a) An example ray generating a lateral component of the optical trapping force. b) Example rays generating an axial component of the trapping force.

To think of it in more simplistic terms, let's imagine we have a glass football. If we were to shine a laser right through the centre of the football, the laser light would just travel straight through, with little reflection and no refraction. This is because both θ_1 and θ_2 from equation 1.2 are equal to zero. Therefore $\sin\theta_1$ and $\sin\theta_2$ are equal to zero, even though their refractive indices may differ, as the light reaches the ball when it is perpendicular to the plane. However, if we were to move the ball slightly to one side, the direction of the light propagation and the plane of the surface of the ball where the light hits will no longer be perpendicular to each other, and hence refraction will occur, along with some reflection. This refraction will cause the light to change direction when travelling through the ball, due to Snell's law, as the

refractive index of glass is higher than that of air. This change in direction means that the light has a change in velocity. There is also a change of momentum, since

$$\vec{p} = m\vec{v} \quad (1.3)$$

where p is momentum, m is the mass of the photon and v is the velocity of the coherent laser light. If there is a change in velocity then the light must be accelerating. This fact, and knowing that there is also a change in momentum on the photons in the light over time, means there must be a force acting on the light, due to

$$\vec{F} = \frac{d\vec{p}}{dt} = m\frac{d\vec{v}}{dt} = m\vec{a} \quad (1.4)$$

Where F is force, $\frac{dp}{dt}$ is change of momentum over time, m is mass, $\frac{dv}{dt}$ is change in velocity over time, and a is acceleration.

Newton's third law states that for every action, there is an equal and opposite reaction, meaning that in every interaction, there is a pair of equal and opposite forces acting on the two interacting objects, in this case the light and the ball. Therefore, if there is a force on the laser light there must also be a force acting on the ball. In this large macroscopic case, the force acting on the ball due to the momentum change would be tiny and therefore negligible. However, if we were to shrink the ball down to the microscopic scale, this force is important and large with respect to the object size. Figure 1.1 shows the different trapping mechanisms in optical tweezers.

When the light enters a microscopic object, free to move in a fluid, it goes from a low to a higher refractive index, n . Therefore the light is bent towards the interface normal. If the light was travelling along the normal (the equilibrium position), there

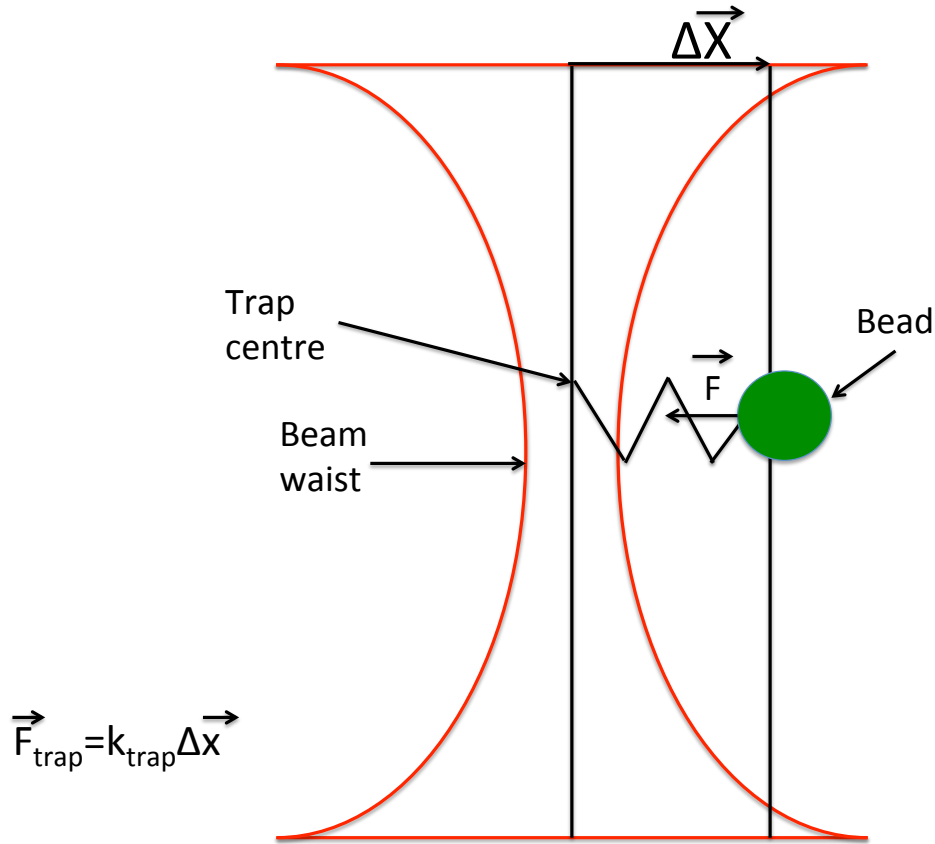


FIGURE 1.2: An optical trapping force can be described like a spring, with a spring constant k_{trap} . A trap has an optical restoring force, F_{trap} . The trap's restoring force acting on a trapped bead follows Hooke's law and is proportional to the distance the bead is from the centre of the trap (Δx). Hooke's Law can only be used for small displacements from equilibrium position (~ 1 radius of the beam width). Note that the trap centre is slightly above the focus of the beam.

would be no bending of the light. When a particle is displaced away from the equilibrium, there would be a change in the vector velocity of the light, meaning there is a change in momentum ρ , due to Equations 1.3 and 1.4. This results in a reaction force pushing the object back towards the trap's equilibrium, so that momentum is conserved, thus allowing lateral trapping [19]. This force acts like a restoring spring force, which is equal to:

$$F = -\kappa \Delta \vec{x} \quad (1.5)$$

Where κ is the optical trap stiffness, similar to that of a spring constant, and Δx is the displacement of the bead with respect to the trap centre (the centre of the laser beam). It is negative due to it being a restoring force, which is acting in the opposite direction to the trapped bead's motion, i.e. away from the trap centre. As long as the displacement of the trapped particle is within a similar scale to the radius of the beam width, further displacement of the particle from the equilibrium position results in a bigger reaction restoring force acting on the particle (figure 1.2).

If we were to use only a weakly focussed Gaussian beam, the particle is only trapped laterally, with radiation pressure pushing the particle along the axial direction. However, when the beam is tightly focussed using a high numerical aperture (NA) objective (more than or equal to 1.3NA), the particle can be trapped both laterally and axially.

Axial trapping is achieved when the negative reaction force (often referred to as the gradient force) on the bead, due to the refraction of the tightly focussed laser, is greater than the scattering force due to reflection. This force acts to keep the bead close to the region of highest intensity. For the case of the weakly focussed beam, stable 3-dimensional trapping can still be achieved by balancing the scattering forces on the particle from opposing beams. This is described by Ashkin et al. [20]. However, all the experiments described in this thesis use gradient optical traps and use silica bead sample where the scattering forces are minimised compared to other commonly used sample such as polystyrene.

Within the trap, particles will still move due to random Brownian kicks [21], from collisions with the fast-moving atoms or molecules in the sample fluid. This motion can be tracked and recorded using a high speed camera and computer algorithm, that can acquire and process images at kHz frame rates [22]. Measuring the Brownian

motion of a trapped microbead can be used to calibrate the trap, allowing piconewton forces to be measured.

1.1.2 Optical Tweezer Set Up

For a single gradient beam trap to be used in a light microscope, it is essential to have a laser, and a beam expander. The beam expander adjusts the beam width, so that it slightly overfills the Fourier plane and the back aperture of the objective lens. We are able to adjust our trap position in the sample plane, by placing a steerable mirror at the Fourier plane, allowing the user to have some control over the trap. The laser trap light then travels through a dichroic filter and tube lens, and passes through a high Numerical Aperture (NA) objective lens, where the laser beam is tightly localised, thus forming a gradient trap in which microscopic objects can be trapped in three dimensions.

This trapped object can then be viewed, using the microscope, with the image light travelling back through the objective and tube lens, and is then reflected at the dichroic. The light then goes through a 4f imaging system before reaching the camera, allowing the image to be viewed and recorded via a computer. An schematic of this setup is shown in Figure 1.3.

The steerable mirror in the trapping arm of the system can be replaced with many other components. For example, two bi-prisms or a beamsplitter could be placed in the Fourier plane, producing two separate static optical traps. Unfortunately, there would not be much control of the positions of these traps within the sample. Options for producing time varying optical traps, where the traps are more easy to position, include using Acousto-Optic Deflectors (AODs) or piezoelectric (piezo) mirror mounts. AODs and piezos allow rapid movement of a trapping laser at a

number of trapping sites (ideally suited for more than two trapping sites) based on a time sharing configuration [6, 23, 24]. Due to the high speed, the laser is much faster than the trapped bead can respond, and it can appear that there are two traps at once, even though the trap is only in one spot at a time. However, this trap movement is not typically smooth, nor is it sinusoidal. To produce more than two optical traps simultaneously, or produce smooth time-varying optical traps, while still having some choice in their initial positions, it is convenient to place a Spatial Light Modulator (SLM) in the Fourier plane, to produce a Holographic Optical Tweezer (HOT).

1.1.3 Holographic Optical Tweezers (HOT)

For some Optical Tweezer experiments, multiple traps or time-varying traps are required. This was difficult to do traditionally. A way to add multiple traps, where the number of traps and their positions can be defined by the user, is to place a hologram in the Fourier plane, rather than steerable mirrors, in the laser arm of the Optical Tweezer system. This setup is called Holographic Optical Tweezers (HOT) [25–27]. An example of this set up can be seen in Figure 1.4.

HOT uses an optical element called a Spatial Light Modulator (SLM), a re-programmable liquid crystal display (typically 512x512 grey scale pixels), that displays hologram patterns. These SLMs are typically phase only modulators and hence the SLM can shift or steer the laser beam, without significantly affecting its intensity, in the same way as a prism can be used. Many SLM displays can run as quickly as a 200 frames per second, or even 1000 frames per second with the aid of overdrive software [28]. This does not only make it safer to use the setup (as we can control the trap position remotely away from the laser), but it also allows flexibility in our control of optical traps. We can design holograms for our desired trap positions and characteristics in three dimensions, as well as design holograms to correct for trap aberrations, such as

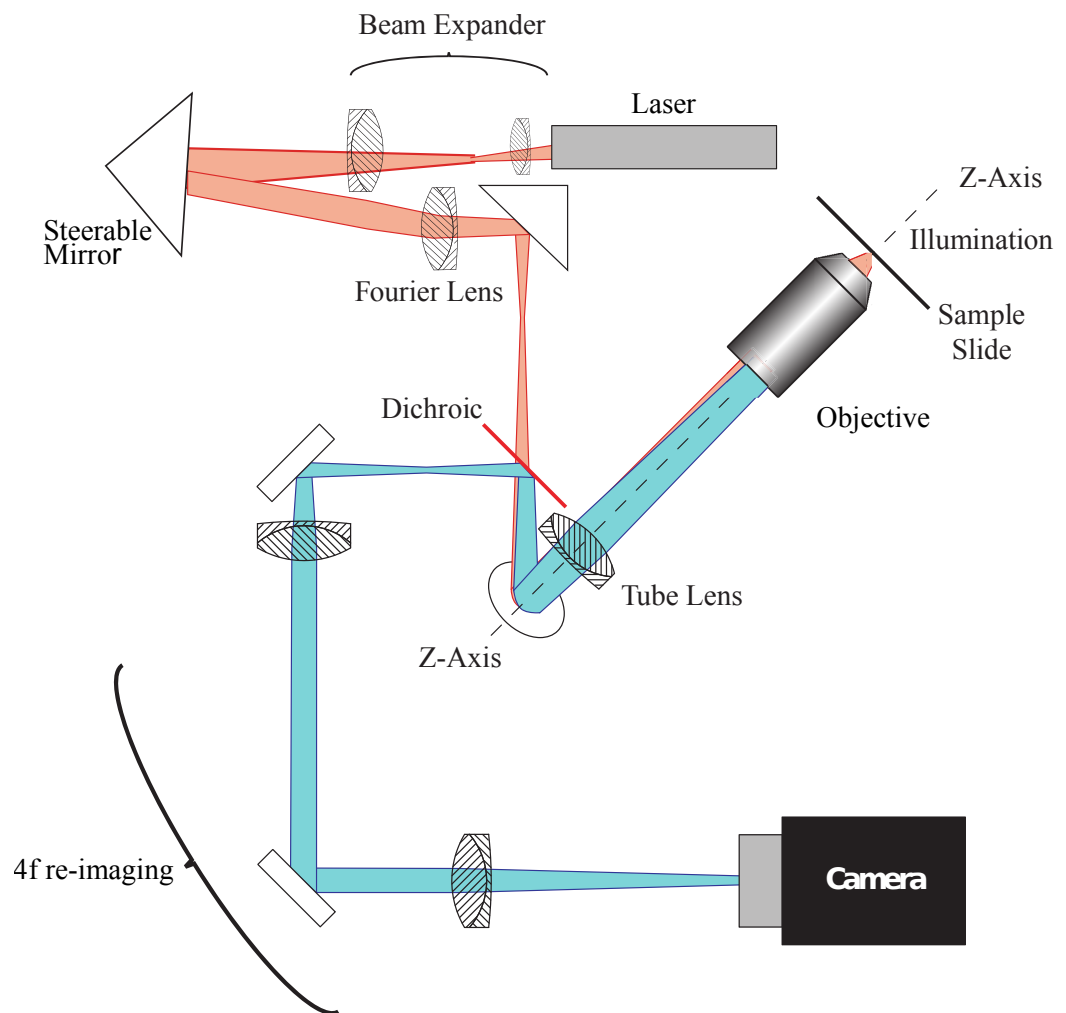


FIGURE 1.3: Schematic of a generic Optical Tweezer setup with a steerable mirror in the Fourier plane used to control the trap position. It is based upon an inverted microscope. The laser beam is expanded, using a 4f beam expander. It then reaches the steerable mirror, which allows movement of the trap position. It then travels through a Fourier lens and travels through a Dichroic filter, and reaches the tube lens. The beam is then focused in the objective lens, and a trap is formed in the sample. The sample is then imaged, with light travelling back through the Objective and Tube lenses. It is then reflected at the Dichroic, reaches an image plane before being re-imaged again through a 4f setup.

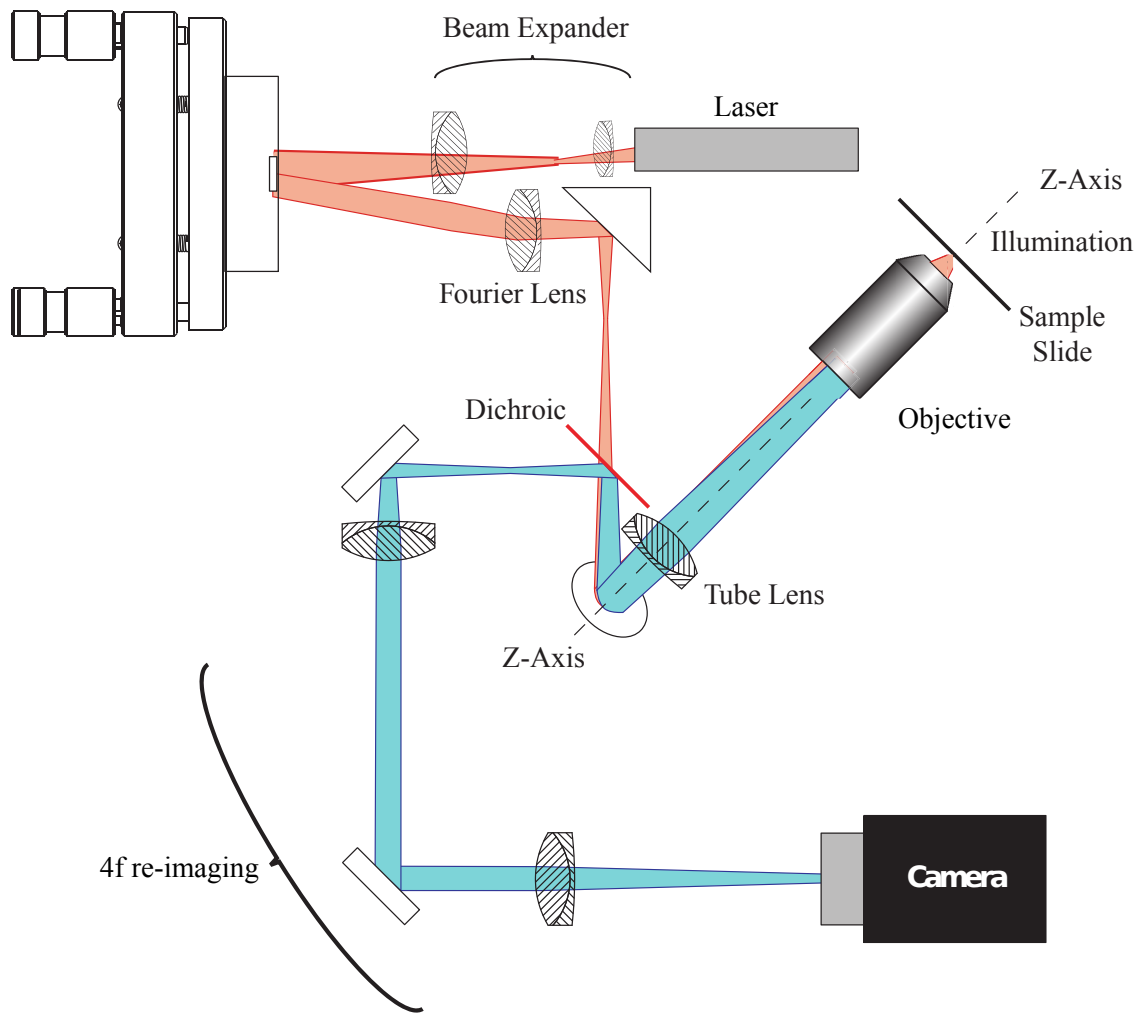


FIGURE 1.4: Schematic of a generic Holographic Optical Tweezer (HOT) setup. The steerable mirror (as seen in Figure 1.3) has been replaced by a Spatial Light Modulator (SLM), a grey scale liquid crystal display that projects hologram patterns. This allows the Optical Trap to be shifted in all three dimensions, as prisms do, with ease computationally.

spherical aberrations, where not all the trapping laser light is focussed to the same trapping spot. This causes a decrease in the trap power, making a trapped object more loosely trapped, making it easier to escape. It is also possible to create complex trap profiles to suit particular experiments.

When the SLM is placed in the Fourier plane, and no hologram is displayed, the SLM just functions as a stationary mirror. A hologram can then be designed that corresponds to the interference of the required plane waves at the Fourier plane,

resulting in a diffraction grating that can be used to control the number and lateral positions of the traps. In addition, a lens hologram can also be added to shift the plane of the traps to another height in the sample, allowing arrangements of traps to be created and controlled in three dimensions [29].

To create or change the position of a HOT trap one can use the ‘Grating and Lenses’ algorithm [29]. This algorithm combines the individual holograms for each axial (z) and lateral (x,y) shifts, as shown in equation 1.6. This gives the phase shift (ϕ) required to move a trap position x, y, z as a function of the SLM pixels u and v (vertical and horizontal respectively). Figure 1.5 shows some examples of holograms used to create and position optical traps.

$$\phi_{xyz}(u, v) = \left(\frac{ku}{f}\right)x + \left(\frac{kv}{f}\right)y + \left(\frac{k(u^2 + v^2)}{2f^2}\right)z \text{ mod } 2\pi \quad (1.6)$$

Where k is the wavenumber equal to $\frac{2\pi}{\lambda}$ and f is the focal length of the Fourier transfer lens after the SLM. For multiple traps, we use equation 1.7 to combine the phase shifts together.

$$\phi_{total} = \text{arg}\left(\sum_i A_i \exp(j\phi_i)\right) \quad (1.7)$$

In equation 1.7, the light fields are represented as complex numbers, each with amplitude (A) and a phase (ϕ) [30]. i in the equation represents the trap number. We only require the argument of the equation (the real part).

In theory, an SLM can produce of the order of 1000 traps. However, due to the finite power produced by the incident laser, which would have to be shared between all traps, the number of traps that can be produced is much less. Still, a laser having the power of a few watts can be used to produce in excess of 100 traps, of suitable

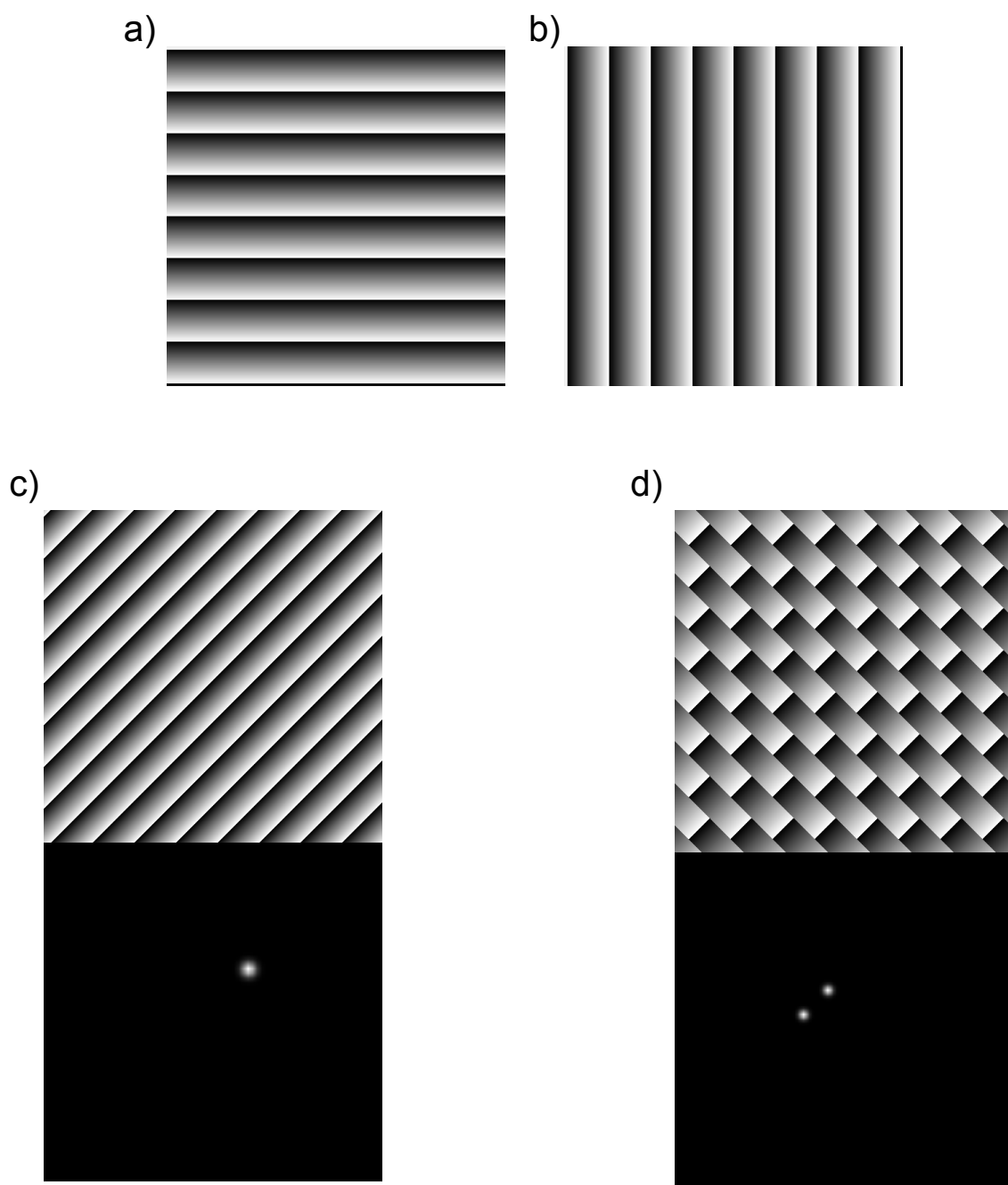


FIGURE 1.5: Example hologram images created using the ‘grating and lenses’ algorithm. a) Hologram to create and position the optical trap vertically. b) hologram to create and position the optical trap horizontally. c) $\text{mod}.2\pi$ addition of the above holograms to create and position one optical trap laterally. d) Complex addition of the above holograms to create two independent optical traps. Also shown in c) and d) are the corresponding Fourier transform, giving the trap arrangements in each case.

strength for applications. It is not only the distribution of the available laser power that limits the number of optical traps that can be produced. Each trap requires a hologram and these all have to be combined to produce the corresponding hologram to achieve the desired trap distribution. For distributions of more than 100 traps, the computational problems associated with combining the individual holograms becomes harder, resulting in a significant reduction in hologram update rate on the SLM.

Although this method produces desired spots, it also produces undesired spots. As we only modulate the phase and not the magnitude, there is too much light on some parts of the hologram. The extra light appears as ‘ghost orders’ and produces ‘ghost traps’ that are not intentional. Ghost orders can become a problem in many trapping experiments, especially in highly symmetric trap arrays, where amplitudes are identical. Ghost orders become more problematic at more complex hologram designs.

Another way of designing a phase shifting hologram to allow trap movement is to use an iterative algorithm, such as the Gerchberg-Saxton algorithm [31]. The method uses Fourier Transforms to retrieve the phase when the intensity of light is known at the source, and the desired intensity and image is known for the target. In our case the target is the sample and the desired target intensity is the desired trap arrangement. The Gerchberg-Saxton method is more mathematical and computationally intensive compared to ‘Gratings and Lenses’, and thus can be more time consuming, which has been mentioned in Di Leonardo et al. [32]. However, we can use the positive aspects of both methods and use a combination of the Gratings and Lenses method and the Gerchberg-Saxton method, to optimise the hologram design, and thus the optical traps.

1.1.4 Force Measurements Using Optical Tweezers

Optical tweezers are a useful tool in many aspects of biology, including cell manipulation and active micro-rheology. They are often described as pico-Newton sensitive force transducers, and when used in this way, they can be an effective tool in measuring forces acting upon a trapped object [3, 4, 6, 7].

The way these forces can be measured is fairly simple, if the trapped object is at an equilibrium with respects to its corresponding optical trap's centre, and if the object's position can be easily measured, is to equate external forces acting on the object to the optical trap force. This trap force is equal to:

$$\vec{F}_{trap} = -\kappa_{trap}\Delta\vec{x} \quad (1.8)$$

where κ_{trap} is the stiffness of the optical trap, and $\Delta\vec{x}$ is the displacement of the trapped object with respects to the optical trap centre. An average position over a longer period of time needs to be calculated, to follow the Brownian motion of the trapped particle. If we do this over a long period and record the timing data, this average is called the Mean Square Displacement (MSD). If we do this over a shorter period, and do not record the timings, the average position is the variance.

To measure forces and use Optical Tweezers in experiments, we must determine a value for κ , and thus must calibrate the tweezer [33]. There are many way to do this. Normally it is calculated, for each degree of freedom, using Eq. 1.9, which is known as the equipartition of energy theorem:

$$\frac{1}{2}k_bT = \frac{1}{2}\kappa \langle x^2 \rangle \quad (1.9)$$

where k_b is the Boltzmann's constant, T is the absolute temperature (usually 293K, room temperature), and $\langle x^2 \rangle$ represents the variance (as it is not time dependent). By measuring the average position of the trapped object with respects to the trap centre we are able to rearrange Eq. 1.9 to calculate κ . This gives an numerical answer for κ without needing to know the sample fluid's viscosity. However, for the equipartition theorem to be valid, the sample fluid must be at thermodynamic equilibrium, meaning no other reactions must occur in the fluid other than friction. Unfortunately, this is not the case for some biological fluids, as some chemical reactions may occur. Therefore the equipartition theorem would give incorrect results, and would therefore not be a desired way to calculate optical trap stiffness in biological applications.

The equipartition theorem only applies, for small displacements from equilibrium position, as Hookes' law can only be used under this condition. We can therefore use the theorem with the variance of the bead, and therefore can be used in force transducer experiments. It cannot be applied with MSD, and therefore cannot be used for micro-rheological experiments.

Another process to measure κ , and hence forces acting on trapped objects, is by finding the relationship between the power of the trap and the frequency of the movement of the trapped object, and hence finding the power spectrum of the trap [22, 34]. This measurement is in the frequency domain, where the corner frequency (ω_c) of the produced spectrum provides information the stiffness of the optical trap divided by the viscosity ($\omega_c = \kappa/\gamma$). If the corner frequency is very distinct and measurable, it is much easier to find a numerical answer for κ . An example of a power spectrum is shown in figure 1.6.

However, this power spectrum process only works if the fluid is Newtonian and its viscosity is known, which is not always the case for optical tweezer experiments. Another issue with the power spectrum procedure is the apparent noise. Spectra

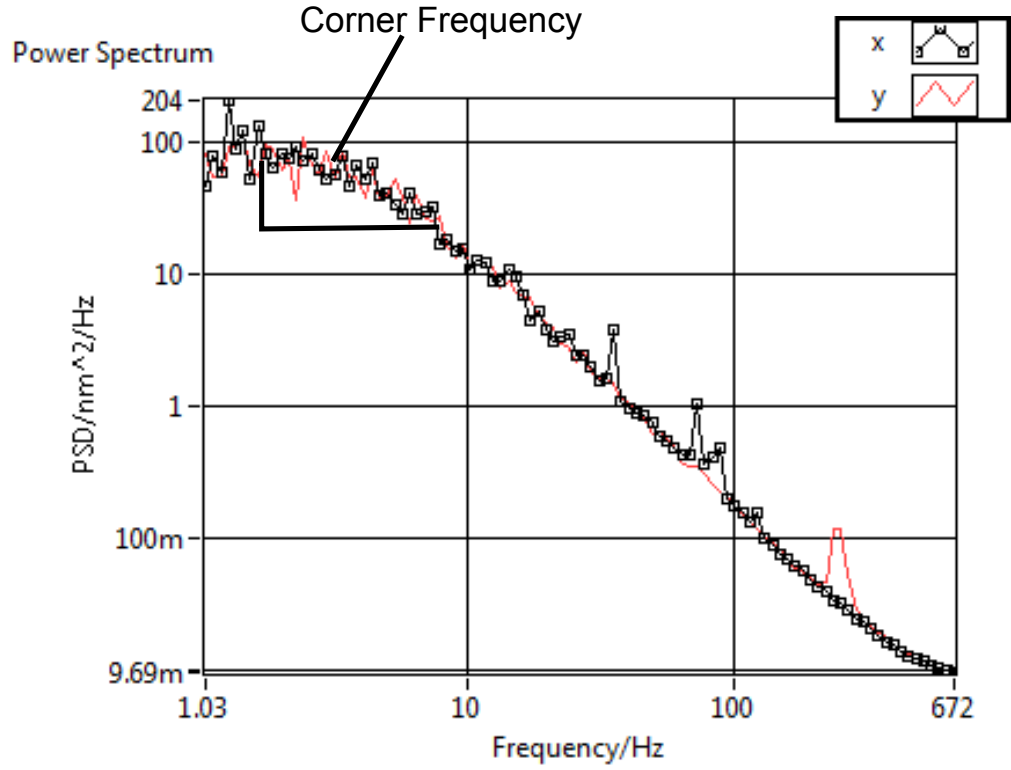


FIGURE 1.6: An example of a power spectrum for x and y tracking data in brightfield, with low noise in the system. Note that the curve is similar to a Lorentzian curve, and so reading a corner frequency, and thus finding the optical trap stiffness, can be done with ease.

produced are usually very noisy, and must be fitted to a Lorentzian. Care must be taken when fitting a Lorentzian, particularly if the fluid is non-Newtonian or the fluid is not at thermodynamic equilibrium. If the fit is wrong, κ results will be skewed and incorrect. This has a bigger effect with higher frame rates.

Another way to find κ is to track the position of the trapped object over time and find the autocorrelation of the displacement [35]. This procedure is done in the time domain. This autocorrelation is found using equation 1.10.

$$\langle x(0)x(t) \rangle = \langle x^2 \rangle \exp\left(\frac{-t}{\tau}\right) \quad (1.10)$$

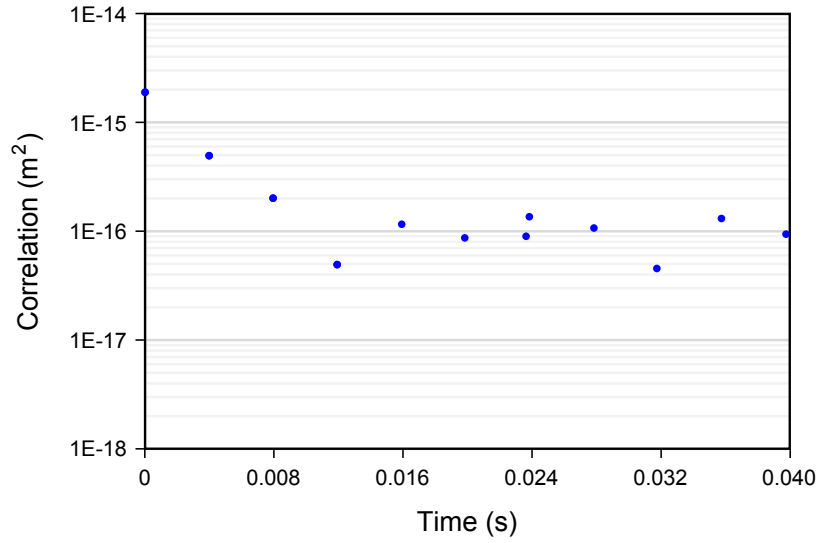


FIGURE 1.7: An example of an autocorrelation function for x tracking data in fluorescence, with noise in the system. This data is taken from Chapter 2. Note that the fit is straight up until the fourth data point, before the gradient changes. This is when noise begins to show. At this point, the noise in the system should be considered and factored in. Information about the value of κ is taken from the decay of the slope.

where $\langle x^2 \rangle$ is the variance of the trapped object displacement from the centre of the trap, and τ is the characteristic decay time of the system. This decay gives two independent parameters: trap stiffness (κ) which can be calibrated using Equation 1.9, and the drag force coefficient (γ) which is directly proportional to fluid viscosity [10]. The y-intercept of the autocorrelation produced using the equation equates to the variance of the particle motion. We can calculate κ using Equation 1.9 and hence use Equation 1.10 to find the fluid viscosity, as:

$$\tau = -\frac{6\pi r\eta}{\kappa} \quad (1.11)$$

where r is the radius of the trapped object, and η is the fluid viscosity.

If we were to use this procedure, we would take a long measurement, then split the data up into smaller time segments and build up a table of averages. The autocorrelation of the particle position also gives information about the standard deviation of

the bead motion via the y-axis intercept value .

The noise in this correlation is clearly visible, as it after the constant gradient correlation. Therefore it can easily be taken into consideration when calculating κ , which is an advantage when it comes to fitting. The fluids in this method do not necessarily need to be Newtonian either, and works for visco-elastic fluids, which would be helpful in some biological experiments.

As the position of the trapped particle is constantly moving due to the thermal motion, we need statistically valid measurements, so all three processes require the knowledge of the trapped particle's position over a set length of time, to find the particle's average position, and hence high speed tracking of the particle is required.

There are methods of measuring optical trap stiffness, and hence force without tracking particle position [23, 36, 37]. One method is taking a drag force trap stiffness measurement. For the drag force method, a trapped bead is moved at a constant velocity through the sample fluid. The force acting on the bead is proportional to the velocity of the bead as:

$$F = 6\pi\eta Rv_s \tag{1.12}$$

Where η is fluid viscosity again, R is the radius of the trapped particle, and v_s is the particle velocity. This force moves the bead away from the trap centre until the drag force is in equilibrium with the optical trapping force. Therefore, by using equation 1.8, we are able to calculate κ . Forces can also be measured by slowly accelerating the trapped particle, until it escapes the trap. The optical force can then be equated to the drag force, using the velocity of the bead at the point of escape. For both, a known and constant fluid viscosity is required for this method.

It is important to point out that this method requires a relatively clear sample such that no contaminant particles affect the measurement of the escape force of the trap, in addition to assuming a uniform sample fluid viscosity. It is therefore less suited to applications requiring point measurements.

1.1.5 Particle Position Tracking

In early high-speed tracking work, Quadrant Photodiodes (QPDs) were commonly used to track a particle's position at rates of several thousand frames per second [36, 38, 39] due to their extremely sensitive way of measuring the position of a trapped particle. This can be done by detecting displacement of a trapped bead by measuring the displacement of the laser spot in the back focal plane of the condenser, using a QPD. This consists of four detector quadrants, and measures the total intensity that reaches each quadrant (due to the laser beam deflection). Differential amplifiers are used to work out the lateral position of a particle, while summing amplifiers can be used to work out its axial positions. The QPD tracking method has precision reportedly of up to $1 \times 10^{-10} \text{m}$ [40]. This technology however does not allow you to simultaneously view the trapped particle while recording data and can be difficult to calibrate, especially when used to measure the axial displacement of a particle.

The development of high-speed CMOS video cameras has allowed QPD technology to be replaced with video microscopy, allowing one to view the particle while recording its tracking position data. If the region of interest on the CMOS is significantly reduced in size so as to only image the particles of interest, we are able to get tracking frame rates of up to a few thousand frames per second [41], and even tens of thousands of frames per second for more sophisticated cameras [42]. Another advantage to using CMOS for video tracking rather than QPD is that video tracking programs can be easily extended to track multiple particles simultaneously, High-speed video-tracking

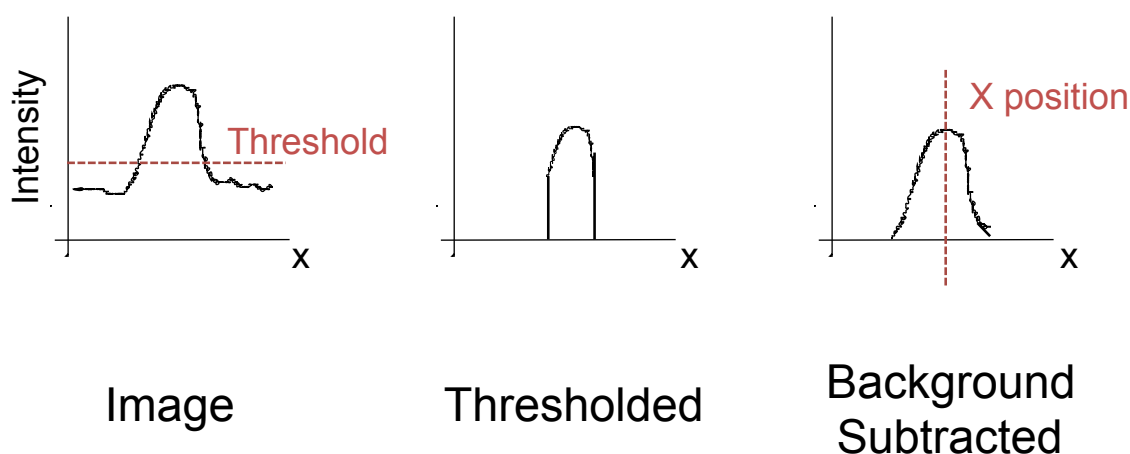


FIGURE 1.8: An example of the intensity of an image, in the x axis, through the thresholding process. A threshold is placed on the original intensity chart, with every intensity below the threshold set to zero. However, noise can result in large fluctuations at the points where the threshold is applied. A solution is to subtract the background from the original intensity, leading to no intensity within the image to be less than zero, which then gives our new thresholded intensity. The position of the centre of the particle is then at the centre of this new intensity chart.

is also fairly simple to calibrate, enabling an absolute measurement of the transverse displacement of the particle [22, 43, 44], and can achieve a precision of approximately 1nm (1/100 of a pixel) [45]. These examples of high-speed video tracking are an extension of earlier particle tracking work, which had previously been limited to standard video rates due to the available technology at the time [46].

The vast majority of this previous work utilising video tracking in optical tweezers was performed using brightfield microscopy. Video particle tracking is easy to implement in brightfield, as long as the trapped particles are both uniform and spherical (such as a bead), and there is a clear centre of mass or symmetry [46]. At this point, the video can be thresholded, where the pixel is set to black if the intensity is below a certain level. This is so that only the centre of the particle is viewable, eliminating any background light. An example of the intensity of light during this process is illustrated in figure 1.8.

At this point, a centroid, centre of mass or centre of symmetry algorithm can be performed on the ‘thresholded’ video data, to find the mean position of the particle over time. There has been various studies on the effect these algorithms may have on errors [47, 48], and so one should choose the optimum algorithm with care, but approximately these algorithms can give tracking data with precision in the order of nm [22].

In this work we mainly used a centroid tracking algorithm. This is a very simple but efficient way of finding the position data of a trapped particle. For example, let’s call the intensity of a pixel at position (x,y) $I_{x,y}$. The sum of the intensities of all the pixels is given by:

$$S_I = \sum_x \sum_y I_{x,y} \quad (1.13)$$

Then if we evaluate the sum of the intensities multiplied by x and y each time as:

$$S_x = \sum_x \sum_y x \times I_{x,y} \quad (1.14)$$

$$S_y = \sum_x \sum_y y \times I_{x,y} \quad (1.15)$$

we can weight the points by their intensities. We can then find the position of the centre as:

$$\left(\frac{S_x}{S_I}, \frac{S_y}{S_I} \right) \quad (1.16)$$

1.2 Objectives of the Thesis

In this thesis, we investigate ways of improving and optimising the tracking of microparticles for various optical tweezers applications. We discuss how we could optimise and advance the tracking of optically trapped biological samples. Despite some of the applications to biology, all of the experiments here were compared using carefully calibrated spherical and symmetrical silica microbead samples. This includes investigating imaging and tracking in fluorescence, and asking the question which is the best type of camera for high speed video microscopy in very low light conditions. We investigate the possibility of producing non-invasive traps, predominantly hydrodynamic traps, and so observe different models of how hydrodynamic forces can affect statically trapped beads. We also look at the precision of three dimensional tracking using Optical Tweezers combined with stereo-microscopy.

By optimising the more generic Optical Tweezer setup (by sometimes making small changes to the original setup) we will obtain new and more precise data and information, and may be able to perform new and interesting experiments, especially within Microbiology and Micro-rheology.

1.2.1 Structure of the Thesis

In Chapter Two, I will describe a commercial Holographic Optical Tweezer system that I redesigned. I will discuss the changes that were made, and how this resulted in a system that was more reliable and easier to maintain and troubleshoot. In addition, optical aberrations were reduced and the effects of crosstalk between holographic traps minimised. A low cost fluorescence illumination setup was added to allow future applications of the tweezers in tracking biological samples.

In Chapter Three, I will investigate particle tracking at very low light levels, specifically in fluorescence. I will demonstrate the best process to use to calculate the trap stiffness κ , as well as discuss how using two state of the art Scientific cameras, the sCMOS and the EMCCD, can increase tracking frame rates, and provide more accurate tracking data than using a more generic CMOS camera. We also ask the question, which of these two camera types is best to use.

In Chapter 4 I discuss how trapped particles behave under time-varying hydrodynamic forces. I look at two main hydrodynamic flow systems, and link these simple models to water living bacteria, that live in low Reynolds number environments. I discuss whether hydrodynamic trapping could be a viable option for future biological trapping experiments, providing a method of creating traps that are much less invasive compared to their laser based equivalents. Part of this work has been discussed in the Hay et al. Optics Express paper “‘Lissajous-like’ trajectories in optical tweezers” [5].

Chapter 5 is based on the work discussed in the Hay et al. Optics Express paper “Four-directional stereo-microscopy for 3D particle tracking with real-time error evaluation” [49]. I discuss the advantages of using stereo-microscopy for 3D particle tracking, as well as describing the extension of the stereo-microscopy to Quad stereo-microscopy, providing a more robust method of tracking microparticles in 3D and with additional information on the tracking errors.

The work is concluded in Chapter six, where all the work will be summarised, and quantitative results will be restated. I discuss the prospect of future research on each chapter, and mention the idea of combining work from each chapter, to produce a new stereoscopic Holographic Optical Tweezer setup.

Chapter 2

The Redesign of the Meadowlark Cube

This chapter presents work on redesigning and building a commercial Holographic Optical Tweezer (HOT), making the system easier to align and improving the reliability of the particle tracking data. The option of fluorescence microscopy was added using a simple low cost LED as the excitation source. Like the original design, the new design remains relatively compact and has the potential to be easily transported between research facilities in initiate collaborative projects. There are many potential applications of HOTs with fluorescence imaging, especially within biology. It is soon realised that there are potential applications in microrheology of biological systems, which requires a means of detecting the fluorescence at high frame rates. The work of this chapter has led on to a project where state of the art scientific cameras are evaluated for the tracking of fluorescent particles, at high frame rates and for low photon flux. More details of this can be found later in chapter 3.

2.1 Background

‘The Meadowlark Cube’ is a commercial holographic optical tweezer product that was developed at Glasgow University and Meadowlark Industries in Boulder, Colorado [8]. Its main selling point is that it is only one cubic foot in size, thus making it compact, stand-alone and portable. However, because the setup contains an SLM, it still allows multiple HOT traps simultaneously (up to 100’s of traps), which allows the 3D manipulation of objects with a variety of material characteristics, ranging in size from 10’s of nanometers to 10’s of microns. It works across a field of view of 200x200 microns.

In order to achieve the compact optical layout, a unique design was used where the same lens forms part of the laser beam expander and also the Fourier lens for the traps. A consequence of this is the aberrations of the laser light or trapping beams passing through this lens off axis. The aberrations arising from this make it harder to determine the position of a trapped object, and can lead to the calibration of the whole system being degraded, and trap-stiffness results possibly being skewed.

The developers take advantage of the SLM in the setup, as the SLM hologram can be used to correct such aberrations. This software works by dividing the SLM into ‘sub-apertures’. Each sub-aperture projects a spot onto the sample at different positions, producing a distortion of an array of spots, which is then tracked. From this, the phase pattern can be found for the corresponding aberration by recovering the tilt of the aberration phase surface of each of the sub-apertures. This phase pattern is subtracted from the SLM hologram to cancel out the aberration.

Now not only is the SLM used to split the laser beam into it’s separate traps and position the traps within the sample, it also corrects for aberrations, so that the quality of the trap is improved. However, many problems can occur by combining

the two roles onto one SLM. Firstly, combining tasks for the SLM leads to a decrease in trap power and stiffness, as more laser power is being lost at the SLM, and less is reaching the sample. This has been overcome previously by increasing the laser power.

Combining SLM roles also increases the chance of issues involving cross-talk, which came apparent in Dienerowitz et al. research involving biofilms [1]. Cross-talk is when there is unwanted transfer of signals between multiple optical traps. In the case of HOT, this is usually caused by the hologram design on the SLM. In this work, they wanted to measure force interactions between two holographic optically trapped *Bacillus subtilis* during approach. Because of the cross-talk between traps due to the hologram design combining the trap production and aberration correction, the accuracy of the tracking data is limited. This may be especially true when measuring the forces between a pair of optically trapped particles or bacteria in close proximity.

Another issue that stems from adding the aberration correction software to the SLM is that the SLM becomes a compulsory part of the system. As mentioned in the theory section, an SLM is not required to optically trap an object, and a mirror can be used in its place. This is useful to remember in situations such as diagnostic checks. When diagnosing issues with a typical HOT system, one of the best ways to check is to switch off the SLM or to replace the SLM with a mirror, and to check if it is possible to produce a single trap. If it is not possible, the cause of the problem may be an alignment or component issue. If it is possible to trap using a mirror, it is clear to see that the problem is with the SLM or the hologram design. However, this diagnostic test cannot take place with the current design of the Meadowlark Cube due to the SLM being required for the aberration correction.

For this reason, we decided to redesign the Meadowlark Cube. We want to keep its selling qualities. We still want it to be compact, stand-alone and portable. We also

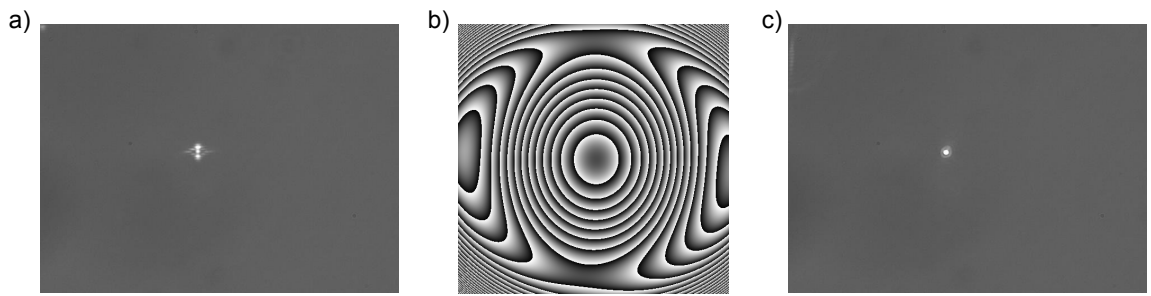


FIGURE 2.1: (a) is an image taken from the Cube of a focussed spot without any aberration correction. (b) is the hologram placed on the SLM to correct for the aberration. (c) is an image taken with the Cube with the aberration hologram on the SLM [8]. This aberration correction hologram is no longer required with the new Cuboid design, reducing cross talk and ghost traps.

want to keep its specifications involving trap number and the sizes of objects that can be trapped. However, we would also like to be able to remove the need and dependency of the aberration correction software, resulting in a system where it is easier to perform diagnostic tests. Crosstalk between traps is also reduced.

Another aspect we want to add to the Meadowlark Cube system is the opportunity to use Fluorescence microscopy. Fluorescence can be a useful tool when using the Meadowlark Cube for biological experiments such as Dienerowitz et al. [1], when the sample is not spherical nor symmetrical [50, 51]. When trapped objects experience Brownian kicks in the axial direction within the trap, the sample can experience a torque, causing the sample to roll and rotate. If the object is non-spherical, such as a cell, it can be difficult to distinguish between the orientation of the cell and its lateral displacement. This makes the trap more difficult to calibrate, and gives less accurate results for trap stiffness [52].

It was shown in McAlinden's 2014 paper that using fluorescence when tracking a cell's position can significantly improve the tracking data. Under a normal visible brightfield microscope, some organelles within the cell are visible, and are still mobile when cells are optically trapped. This will cause problems when using centre of mass and centre of symmetry tracking algorithms, as the centre of mass and centre

of symmetry of the cell will change position significantly over time. If the cell is fluorescently dyed, and viewed under a fluorescent system, the cell's organelles are no longer visible, and the cell appears more uniform and opaque, making the chance of a change in the centre of mass or symmetry significantly smaller. This helps in making cell positioning more definite. Also, by using fluorescent stains and applying a smoothing algorithm, large features associated with cell roll can be reduced without losing the cell's main shape, due to the cell roll being slower than the Brownian motion. This allows more accurate thresholding of the image and can improve tracking results.

A common downside to fluorescence microscopy is that the camera must acquire images over relatively long exposure times, and hence must run at a low frame rate. This is not ideal for high speed video tracking in optical tweezers when information of the trap dynamics is required. When using a generic CMOS camera, we are able to track our fluorescent samples at around 20-30 frames/second. This frame rate could be considerably increased by using a scientific camera such as a Scientific CMOS or EMCCD (as mentioned in Chapter 3) and a reduced region of interest, allowing us to decrease the amount of data acquired and track particles in real time.

We added a compact, low-cost, fluorescence illumination based on a high-power blue LED. We investigated two different methods of coupling the excitation light into the setup. One way was to add the illumination in the imaging arm of the system to back illuminate the sample. The other was to add the illumination to the original red LED illumination microscope source. In both instances, the samples were silica beads stained with a fluorophore called green fluorescent protein (GFP). This has an excitation centre wavelength of 469nm. The emission wavelength of the protein is 525nm, allowing the stained part of the sample to fluoresce green, and to be imaged by the camera. We found that the images produced were better (having higher

contrast) when the sample was back illuminated, with the illumination travelling to the sample via the objective lens. This is because, when the bead is being excited by the light in the original brightfield illumination position, the side of the bead being excited is not facing the camera, hence dimmer images are viewed, making the bead more difficult to track at higher frame rates. Also, the dichroic filter used to couple in the back illuminated (blue) light also helps to filter out the backscattered light, allowing the camera to only image the emission (green) light.

For the fluorescence mode to work, the set up also required an excitation and emission filter, as well as the dichroic filter, used to reflect the blue 469nm excitation light towards the sample. The 469nm light travels to the sample via the objective lens, and exciting the fluorophore, which in turn emits the 525nm emission light. The emission light is collected by the same objective and tube lens and eventually reaches the camera where the fluorescence image is formed.

2.2 Optical Configurations of the two HOT Designs

In the original Meadowlark setup, the Fourier lens is shared with the beam expander, hence producing the undesired aberrations, which need to be corrected using the SLM. This was originally done to save space, and to fit the whole system in a one cubed foot space. The design of this setup is shown in figure 2.3. In our setup, we decided to separate this lens into two individual lenses; the beam expander lens and the Fourier lens, containing a beam expander that can be removed without affecting the other parts of the set up. This was not the case before, as by removing the beam expander, the Fourier lens would have also been removed. This setup is shown in

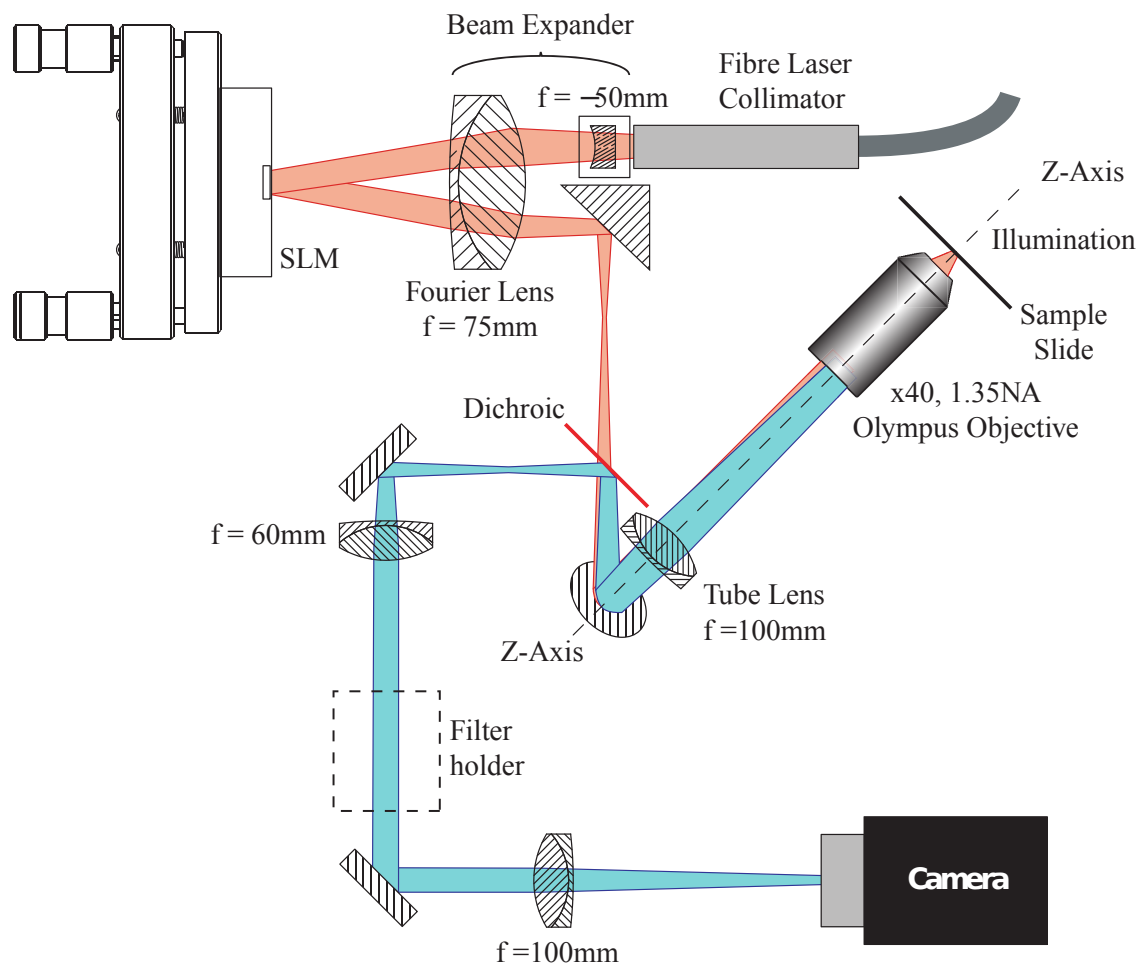


FIGURE 2.2: Schematic of the original Meadowlark Cube. The laser is expanded to fill the SLM. One of the beam expander lenses is then reused as the Fourier lens, leading to aberrations, causing the degrading of the traps before aberration corrections are added to the SLM. After the Fourier lens the laser light is coupled into the microscope with a dichotic filter. A high speed camera allows accurate position tracking of trapped objects.

figure 2.4, and now has the laser beams passing through the centre of the lenses, reducing aberrations.

Unfortunately, by adding the extra lens, the system was unable to keep its precise cube shape. Therefore, to keep it compact, stand-alone and portable we had to redesign the setup and reposition certain components within the system. Separating the laser beam expander and the Fourier lens added $\sim 50\%$ to one dimension of the system. This allowed some extra space in which we could replace the fibre coupled

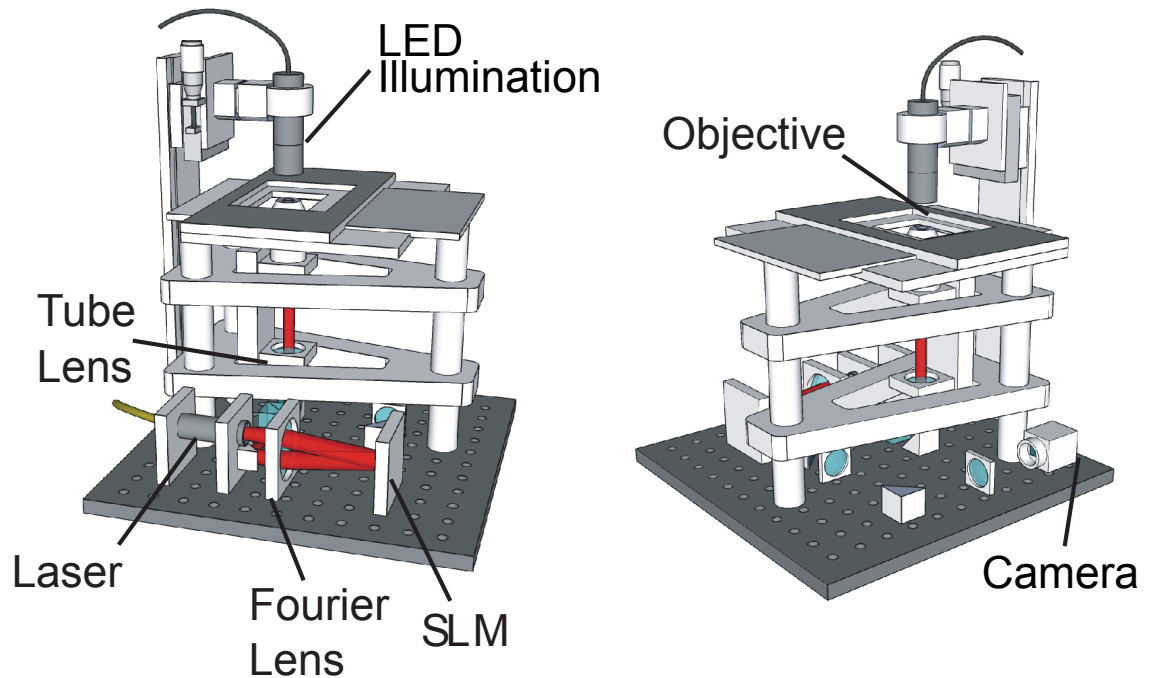


FIGURE 2.3: 3D models of the original Meadowlark Cube tweezer system. With it being only one cubic foot in size, yet still allowing multiple HOT trapping, it's main selling point is that it is compact, stand-alone and portable. However, there are aberration issues due to using the same lens as both a beam expander and a Fourier lens, so that the product can stay portable. Figure from Reference [8]. A space for a filter holder is left to allow filters to be added to epi-fluorescence illumination.

laser in the original setup with a fixed solid state laser. Despite the solid state laser head being larger than the output end of a fiber laser, the system benefited from the overall reduction in size and complexity of the laser source as a whole, including the power supply and control electronics. Having a compact optical tweezers system in which all optics components are mounted on a single unit is an advantage when transporting the system, avoiding the need to maintain an optical fibre link between two separate units. The laser used for trapping was moved to behind the main microscope, and two mirrors were used on either side of the beam expander to steer and position the laser beam onto the SLM. The new shape of the system is now cuboid (24x18x12in), and so it is still fairly compact.

We also had to move the camera in the set up. We found that when the camera was

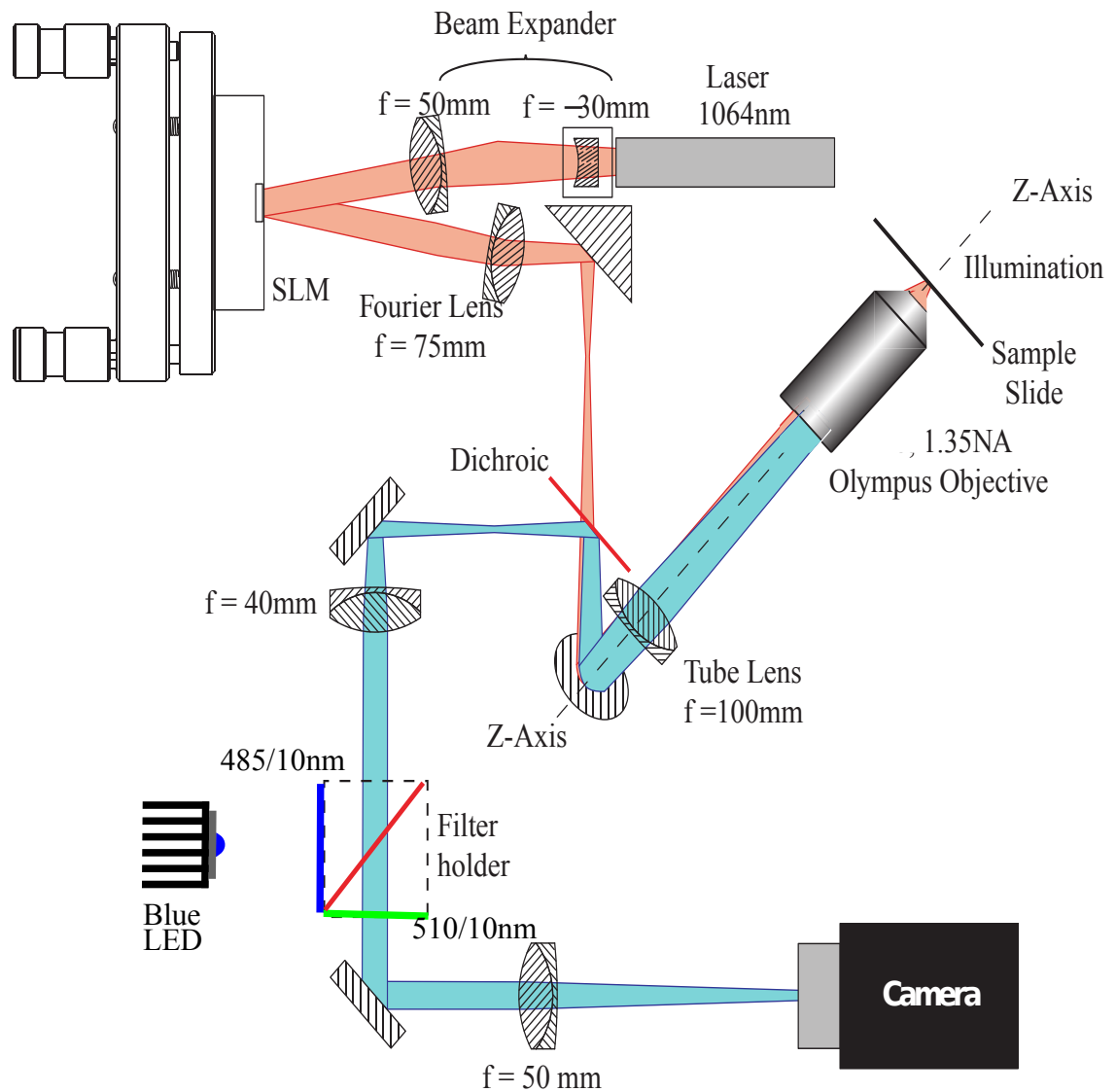


FIGURE 2.4: Schematic of the new Cuboid. The laser is expanded to fill the SLM. There are two distinct lenses in place of one for the beam expansion and the Fourier lens. After the Fourier lens the laser light is coupled into the microscope with a dichroic filter. A reconfigurable filter holder is found in the camera arm, allowing the use of epi-illumination for Fluorescence microscopy and imaging.

in its previous position, the image of the sample was out of focus with respect to the laser trap. This was previously overcome by, yet again, designing an appropriate hologram on the SLM, to move the trap into focus. Ideally, the camera had to be closer to the tube lens in the system. Unfortunately this was not possible, as the dichroic beam splitter was required to be in that preferred position. For this reason, we re-imaged onto the camera using a 4f imaging setup, a setup made up of two lenses separated by the sum of their focal lengths. This set up allowed the camera to access the image plane that was previously blocked by the dichroic beam splitter and its associated mountings. To save space, we turned the imaging arm by 90 degrees, so that the 4f imaging was in parallel to the main microscope frame.

Between the two lenses in the 4f re-imaging system in the camera arm, is where the fluorescence filter holder is located, required for the epi-illumination for the fluorescence microscopy. This holds the excitation filter, which is placed just after the blue fluorescence illumination source, the dichroic beam splitter, and the emission filter, which is placed in front of the camera. The excitation filter allows only a narrow spectral band of light centred on the excitation wavelength to travel through to the microscope sample.

The resulting fluorescence emission from the sample is filtered by both the dichroic beam splitter and the emission filter, resulting in only emission wavelengths reaching the camera. The blue epi-illumination is provided by a blue LED source, which is perpendicular to the CMOS camera, facing the main microscope body and SLM. The new HOT system is now able to produce fluorescence video images of stained microbeads in real time, of suitably high contrast for particle tracking (see figure [2.5](#)).

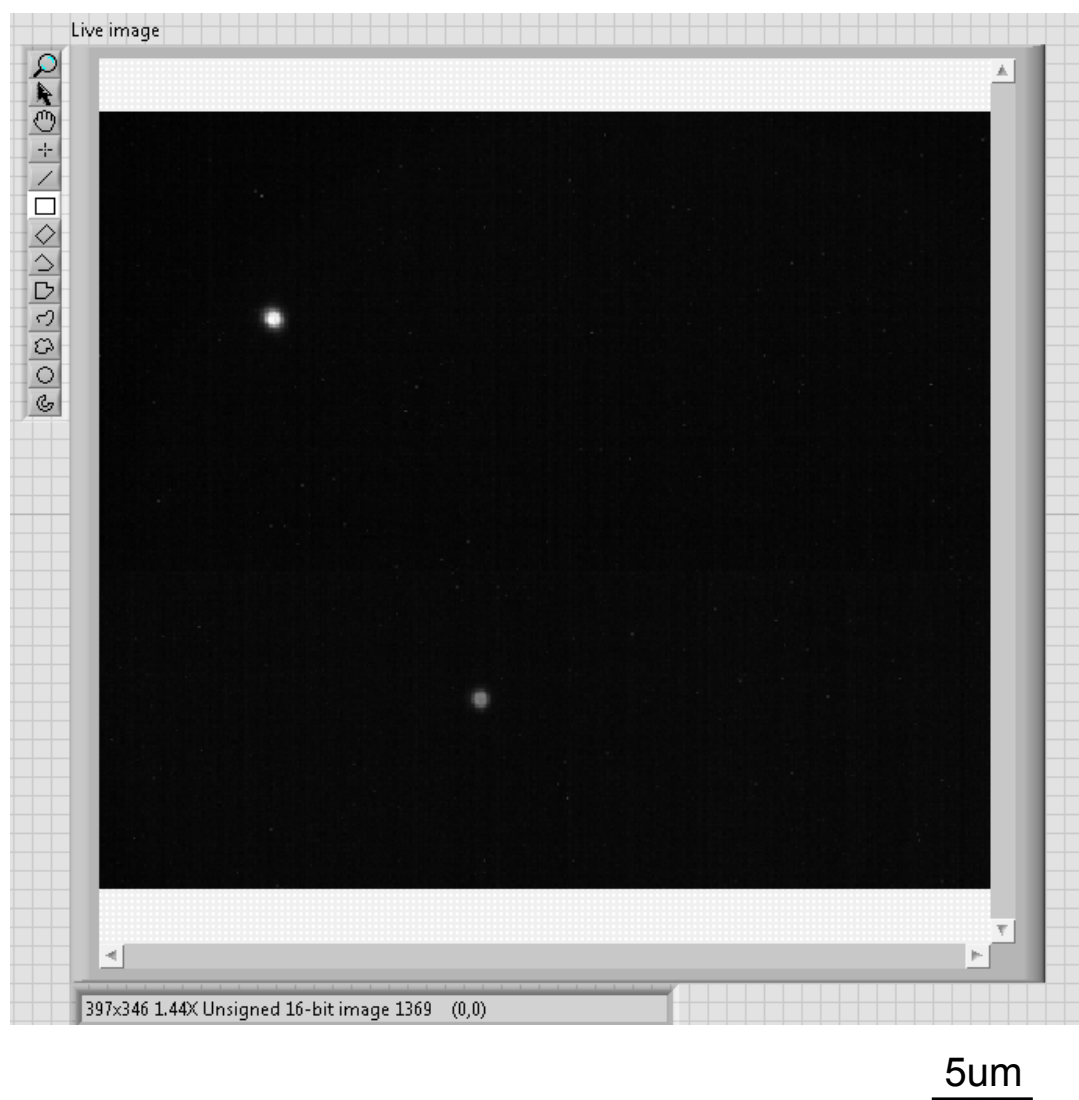


FIGURE 2.5: Live image of two optically trapped fluorescing $1.5\mu\text{m}$ silica beads taken from the imaging and data tracking Labview program. See that the beads are circularly symmetrical in shape. Here we see a highly fluorescing bead and a dimmer fluorescing bead. This is due to the dimmer bead performing less excitation, either due to a lack of fluorescence coating or less blue excitation light reaching the dimmer bead. This image was taken using the Dalsa Genie camera running at a frame rate of 18 frames per second.

2.3 Conclusion

We redesigned the commercial product ‘the Cube’ and built the new ‘Cuboid’. The new design, was still relatively small and compact, but some of the original design ‘flaws’, such as transporting the system with a fibre coupled laser, were removed. The main example of a removal of a flaw was removing the need and dependency of any aberration correction software which the Cube previously required. This was done by replacing the shared beam expander and Fourier lens with two individual lenses, one for each task. This led to laser light not being off axis while travelling through lenses, and hence a reduction in cross-talk of the tracking data of two or more optically trapped particles. We also incorporated fluorescence imaging using a compact, low cost, LED illumination source.

The Cuboid setup would be a desired choice of tweezers to use in future HOT collaborative work with other research groups, as it has a small, compact and standalone design, making it easily transportable. For this reason, the Cuboid will be used for future collaborations with David Phillips at Exeter University, as well as internal collaborations with the Microbiology and Chemistry Departments at the University of Glasgow.

While investigating potential applications of the new HOT with fluorescence imaging, it was clear that there are applications where additional information is required over standard particle position measurements. Such examples could include microrheology studies using tracking data of fluorescent stained cells. In such cases particle tracking at high frames rates are required in order to recover information on the trap dynamics. Chapter 3 covers details of evaluating current state of the art scientific cameras for high speed particle tracking in very low light conditions.

Chapter 3

Comparing EMCCD and sCMOS cameras for low-light high-speed position tracking of optically trapped fluorescing particles

We learnt from the last chapter that fluorescence microscopy can be a useful tool when combined with HOT, especially when tracking non-spherical particles, or non-uniform samples such as cells. However, when video tracking particles (for experiments such as for micro-rheology research), a fast frame rate may be required to obtain as much information as possible about the particle's position. For this reason, it is best to use a higher speed scientific camera, that allows quicker frame rates at lower intensities. In this chapter, we compare 2 different types of scientific cameras to see if they can improve our particle tracking results. The two cameras being compared are fairly large, and therefore this experiment was not done on the small Cuboid, but on a larger fixed system, where there was space to fit both cameras to the set up. This

fixed system still allowed the use of the LED based fluorescence system developed for the Cuboid in Chapter 2. We use spherical beads rather than a non-spherical sample or cells as spherical beads have known specifications including excitation and emission wavelengths, size, and fluorophore stain amount. This information helps to make a fair comparison, and thus evaluate their suitability for fluorescence position tracking experiments.

Here is an abstract for the following work:

We compare the performance of an Electron Multiplying CCD (EMCCD) camera and a scientific CMOS (sCMOS) camera for the high-speed tracking of fluorescent particles trapped within an optical tweezer. We characterise the motion of the particle using the autocorrelation function of its image centroid and examine how the performance of the two cameras depends upon the fluorescence intensity. We show that for fluorescence intensities in excess of a few thousand photons per frame both camera types yield position tracking data that allows the recovery of both the trap stiffness and the motion dynamics. For fluorescent intensities on the limit of detection there is evidence to suggest that an EMCCD camera provides marginally improved tracking data compared to the sCMOS but that noise inherent in the photon statistics, combined with the size of the fluorescent particle, dominates over the camera noise itself.

3.1 Introduction

As covered in section 1.3, Optical tweezers are often used as pico-Newton force transducers, and are an effective tool for measuring forces acting upon optically trapped particles within a fluid [3-7]. An external force acting on a particle (cell or bead)

causes its displacement from the trap centre, the extent of the displacement being dependent upon the trap stiffness (κ) and the applied force.

As the position of the trapped particle is constantly moving due to the thermal motion, to measure κ we need to know the trapped particles's position over time. If the tweezers are using the experiment as a force transducer, with this information, we can either calculate the variance and use the Equipartition theorem to find κ . For this process, no time information is required. If the tweezers are being used for a microrheology experiment, the MSD must be found, and either the autocorrelation of power spectrum method is used to find κ . To use the MSD, we require high-speed particle tracking, which can be performed using high-speed video.

The vast majority of this previous work utilising video tracking in optical tweezers was performed using brightfield microscopy. Video particle tracking is easy to implement in brightfield, as long as the trapped objects are both uniform and spherical (such as a bead), and there is a clear centre of mass or symmetry. However, when the object is non-spherical (such as a cell) problems can occur, for example a rotation of the object can be mistaken for a lateral shift, due to a change in its 2D image shape. The consequence of this is skewed and misleading data being calculated from the centroid measurement algorithm.

There are alternatives to brightfield microscopy that can be used to overcome such problems that occur by using a brightfield mode. One example is fluorescence microscopy: a useful tool in many aspects of microbiology, particularly for particle tracking, where McAlinden et al. noted that using fluorescence can significantly improve the tracking data for an optically trapped cell [52]. Under a regular brightfield microscope some organelles within the cell are visible and mobile even when the cell is optically trapped. This movement will cause problems when using an image-centroid tracking algorithm, because as stated before, the 2D image shape will change and

thus the centre of the cell will appear to move more over time, leading to skewed tracking data. If the cell is marked with a fluorescent dye and viewed under a microscope, the cell's organelles are then no longer visible and the cell appears more uniform and opaque [53, 54]. This means the cell's shape does not appear to change as significantly as under brightfield. This leads to data not being so skewed and a reduction in errors, hence an increase in tracking data quality.

There are setbacks when using fluorescence microscopy, especially when considering video tracking due to the typically reduced light levels in the image. Using a regular CMOS camera to video track fluorescent particles requires long exposures, due to the reduction of light intensity. Although, high frame rates are not required to measure the variance and therefore κ , we would be unable to measure the MSD of the particle as the frame rates that are acquired are typically too slow to track its Brownian motion, for micro-rheological experiments [48]. Information would be lost between frames at low frame rates due to the particle drift being missed, affecting the MSD measurement, and thus skewing the κ result.

In recent years, advances in camera technology such as Electron Multiplying CCD (EMCCD) and scientific CMOS (sCMOS) cameras have allowed images to be acquired at kHz frame rates even at very low photon fluxes (~ 1000 s photons/frame), with a reduced region of interest [55].

EMCCD cameras are single photon sensitive, allowing shorter exposure times, and faster frame rates. EMCCD cameras differ from conventional CCD cameras as they have a dedicated gain register before the readout register. In the detection process of the EMCCD, photons with a high enough energy generate photoelectrons that are stored within the pixel element. These charges are then shifted, making their way to the readout register. The EMCCD's dedicated gain register amplifies the signal by accelerating the photoelectron across a potential difference of several tens

of volts. This process generates secondary photoelectrons that are subsequently read out. This ‘avalanche’ process therefore can multiply even the smallest of signals, which unfortunately also includes the noise within the read out circuitry [56, 57]. This amplification process give EMCCD’s a typical quantum efficiency of up to 90 percent, and has a large dynamic range.

sCMOS cameras are based on scientifically graded CMOS image sensors, and are capable of simultaneously delivering extremely low noise, high frame rates, large dynamic range, high quantum efficiency (around 80%), high resolution and a large field of view [58]. Despite not being able to detect single photons, these properties make it possible to acquire high fidelity images with a high frame rate, even in the absence of avalanche gain. Therefore, in fluorescence optical trapping, either an EMCCD or sCMOS can be used to track particles at higher frame rates compared to standard CMOS and traditional CCD cameras.

sCMOS cameras are also significantly cheaper than EMCCD cameras. We therefore determine what the minimum fluorescence light levels are for reliable tracking, allowing the user to make the optimum choice for a particle experiment. It is also worth noting that sCMOS cameras are often standard equipment in a biology research laboratory.

The Andor iXon3 897 EMCCD camera used can be liquid cooled to temperatures as low as -85°C . It has a 512×512 full-frame resolution with a pixel size of $16\mu\text{m} \times 16\mu\text{m}$, with a 4×4 hardware binning. sCMOS cameras are usually made to be un-intensified, and can be liquid-cooled to a temperature of -30°C . The Hamamatsu ORCA-Flash4.0 V2+ sCMOS used in the experiment has a 2048×2048 full-frame resolution, with a pixel size of $6.5\mu\text{m} \times 6.5\mu\text{m}$, and allowed 2×2 hardware binning. Care was taken in the choice of imaging lenses after the camera box, to make sure spatial sampling in terms

of pixels per bead per frame was the same for both cameras. This is important to ensure a fair comparison of the tracking performance of the two cameras.

In this work we compare the two camera types to determine their suitability for tracking fluorescent beads at high frame rates using images with a low photon flux. We compare the accuracy of position and trap stiffness measurements of a trapped fluorescing silica bead of diameter $1.5\mu\text{m}$. These spherical beads have known specifications including excitation and emission wavelengths, size, and fluorophore stain amount. This allows us to make a fair comparison between the cameras, and to evaluate their suitability for fluorescence position tracking experiments.

We investigate how much fluorescence intensity is required by each camera to track the bead at an image rate of 250 frames per second (fps).

3.2 Method

3.2.1 Experimental setup

Figure 3.1 shows a schematic of the tweezers system used in this work. The system is based around an inverted optical microscope similar to that reported in [22]. A 1064nm wavelength, 3W laser (Laser Quantum, Ventus IR) is used to produce the trap. The laser output beam is expanded, slightly overfilling the aperture of a spatial light modulator (SLM) (Boulder nonlinear optics). Using an SLM and appropriate software enables us to dynamically change the trap position by using the gratings and lenses algorithm [43]. The light diffracted by the SLM is re-imaged onto the back focal plane of the objective lens, 100x 1.3NA (Nikon, Plan-Fluor). This focuses the trapping laser beam in the sample cell.

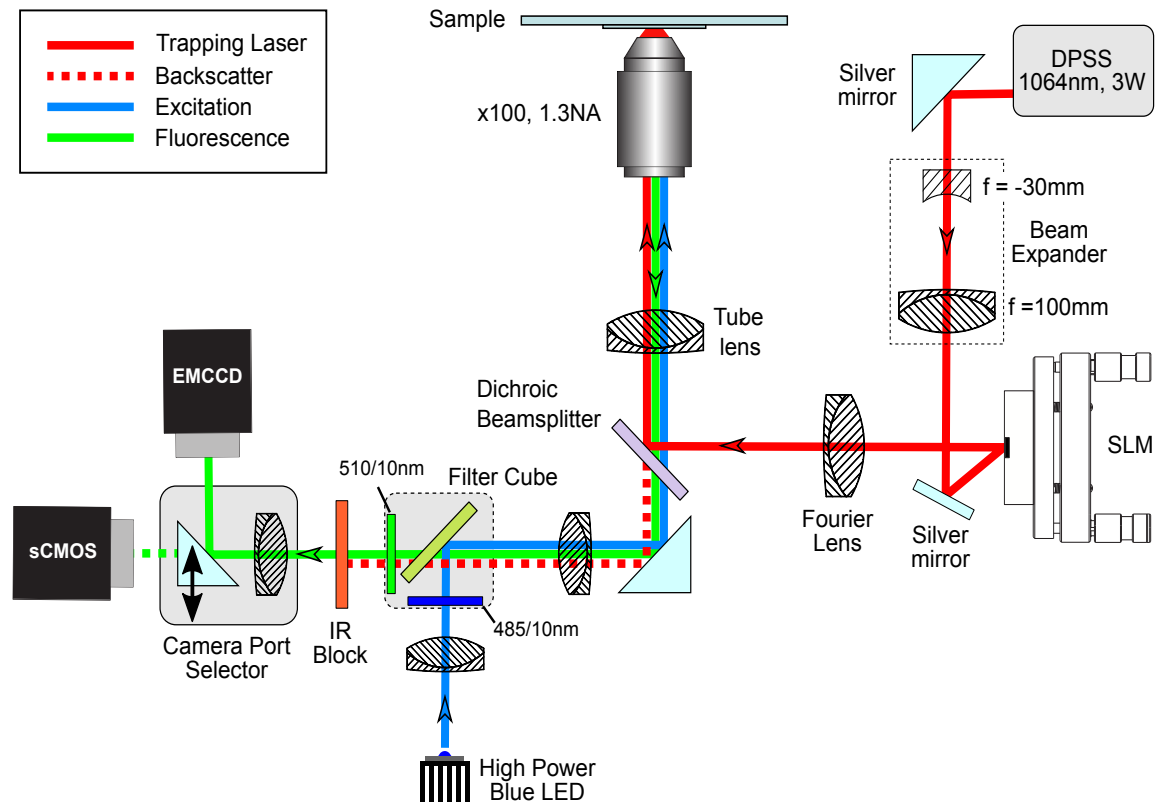


FIGURE 3.1: Schematic of the setup used. The laser output beam is expanded, slightly overfilling the aperture of the Spatial Light Modulator (SLM) (Boulder non-linear optics, XY series 512x512 pixels). After the Fourier lens, the light diffracted by the SLM is re-imaged onto the back focal plane of the objective lens, 100x 1.3NA, (Nikon, Plan-Fluor), which focuses the trapping laser beam in the sample cell. The fluorescence excitation source is a blue LED (Luxeon Rebel) filtered with a 485/10 nm filter and is coupled through the objective using a dichroic beam splitter. Within the same filter cube a 510/10nm filter ensures that only the fluorescence is detected. We used both sCMOS (Hamamatsu ORCA-Flash4.0 V2+) and EMCCD (Andor iXon3 897) cameras to image the fluorescence. A camera port selector determines which camera is used.

The trapped fluorescence-green silica beads (Kisker Biotech GmbH) are $1.5\mu\text{m}$ in diameter. The fluorescence excitation source is a blue LED (Luxeon Rebel), which intensity is varied throughout, and is filtered at 485/10nm and coupled using a dichroic filter through the high NA objective. The trapped bead's fluorescent peak is at 515nm and the camera (either EMCCD or sCMOS) image is filtered at 510/10nm so that only the fluorescence is detected. To enable an easy comparison between our results, we measured the fluorescence intensities using the EMCCD in the photon counting

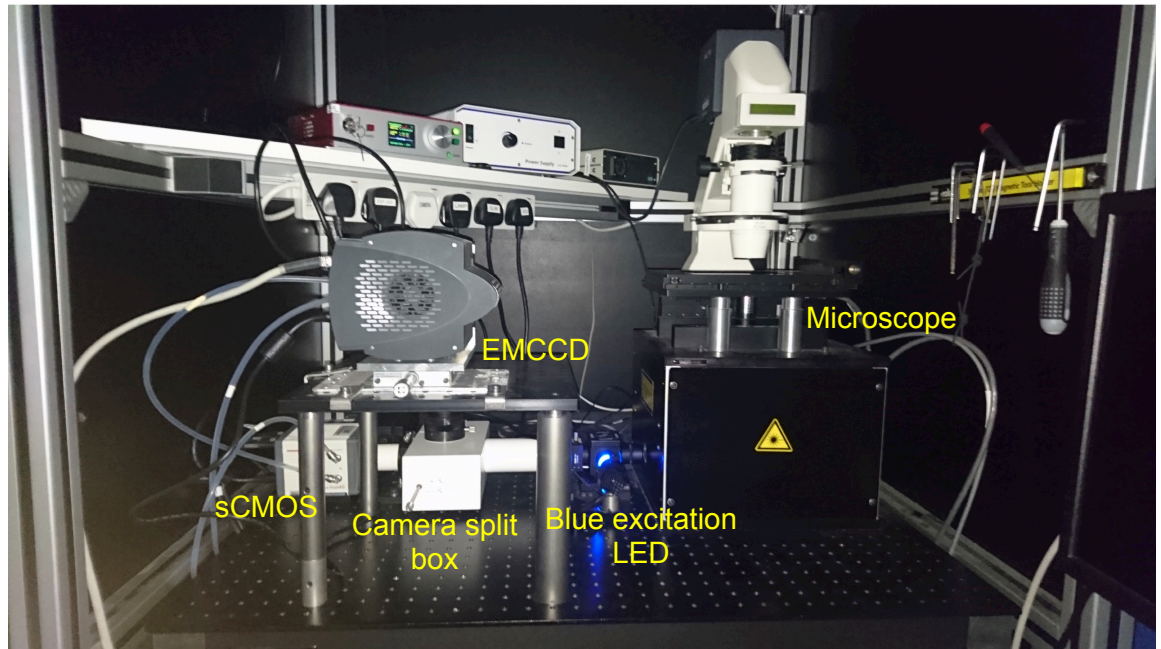


FIGURE 3.2: Photo of experimental setup.

mode, which reads out results in photons/frame. Alternatively, we could have calculated the power input of the excitation source, but we believe that photons/frame at the end of the process would be a more reliable result, as we would not have to consider loss of power within the system. As the bead in our video crosses a circumference of 10 pixels, we could state the bead covers the pixels the area of the bead image covers (approximately 75 pixels. We could then approximately calculate photons per pixel.

3.2.2 Data Acquisition and Analysis

To allow our two scientific cameras to run as quickly as possible, we pre-recorded videos of the trapped bead using both cameras, and post analysed to acquire the data we required. This is unlike more generic brightfield tracking, that allows the user to track a trapped particle live. The choice to pre-record the data was made, so that we could run both cameras at faster frame rates, which is desired for particle

tracking. We also changed the region of interest (ROI) and binning on each camera, so that only the trapped bead was visible and that the camera ran at its optimum speed. We found that the quickest camera speeds that both cameras would work at, due to light level restrictions producing lower quality images that cannot be thresholded, was around 250fps. This was at a reduced ROI of 32x32 pixels and a binning of 2x2 for the sCMOS and 64x64 pixels and a binning of 4x4 for EMCCD. Therefore, for the case of both sets of camera videos, the bead's circumference covered approximately 10 pixels.

Once our videos (10000 frames long) were recorded at 250fps, each video was analysed in a Labview program, that applied a threshold to each ROI to reject background noise without any bias. This allowed only the bead to be viewed. A centroid tracking algorithm was then used on the video to follow the centre of the bead throughout the 10000 frames. This program calculates the bead's x, y position, and hence MSD data, as well as the corresponding time data. An example of the displacement data is seen in Figure 3.3.

At this point, a Labview program was also used for the EMCCD photon count videos. This calculated the total number of pixels from all the frames, and then divided this total by the total number of frames, to calculate an average number of frames per second. We checked for any significant decrease in photons per frame throughout each video in case of photobleaching, however this did not seem apparent. The average photons/frame used in the experiment were therefore: 5650, 4690, 3215, 2870 and 2080 photons/frame. These numbers were chosen by changing the voltage input of the blue excitation LED.

The MSD data was then split into smaller 4 second intervals of data (1000 data points), to limit the effect of any possible longterm drift due to thermal expansion of the laser and microscope. It was then fed into another Labview program that

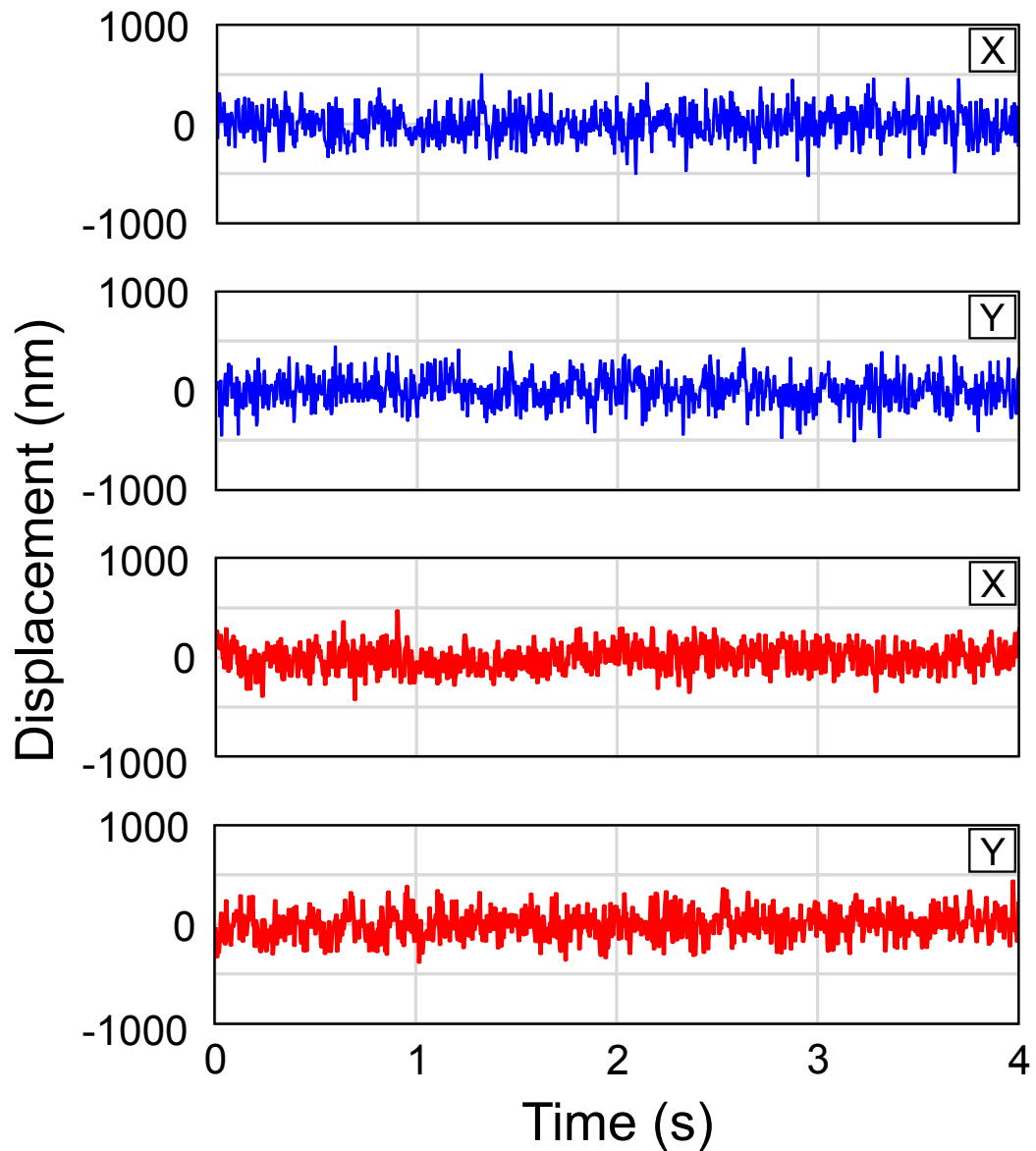


FIGURE 3.3: An example of the x and y displacement data for a 4s interval of data at the highest fluorescence intensity (5650 photons/frame) for the EMCCD camera (blue) and the sCMOS camera (red). The approximation of noise, and hence the error on each x, y position measurement is 10.5nm. This is approximately a factor of 10 larger than the error of from the more general brightfield tracking, which usually has errors of around 1nm. This is due to the limited number of photons in each image.

calculates the autocorrelation of the particle position for each interval. The 4 second interval autocorrelations are then averaged over each dataset.

3.3 Results

We examine the auto-correlations of the particle position to quantitatively compare the performance of the two camera types. We know that the important parts of the autocorrelation that we are interested in are the y-axis intercept, that provides the standard deviation of the bead motion, and the gradient, that provides information about γ and κ . Given that the trap strength, the bead diameter and the viscosity are the same in all our datasets, we would anticipate that the trap dynamics should also be the same, irrespective of the fluorescence intensity to record the data. Therefore the autocorrelations, and thus the y-intercepts and gradients, at all fluorescence intensities should be identical. If any change in the autocorrelation therefore came about, it would be due to the choice of camera.

Figure 3.4 has only four data points on each autocorrelation graph. The slope of the autocorrelation is set by the time constant of the trap and the number of data points depends on the time taken between frames. Therefore, higher frame rates would give more data points on our autocorrelation, and would thus result in a more reliable fit. In our case, we have a considerably lower tracking frame rate of 250fps, 8 times less than the more general brightfield tracking frame rates of around 2000 fps, and therefore we have only an eighth of the data points we would usually have. Any data points added at later times would have the issue of noise to consider. The noise would cause a skew in the gradient in the autocorrelation, which would be detrimental when calculating the trap stiffness. An example of the noise from an autocorrelation

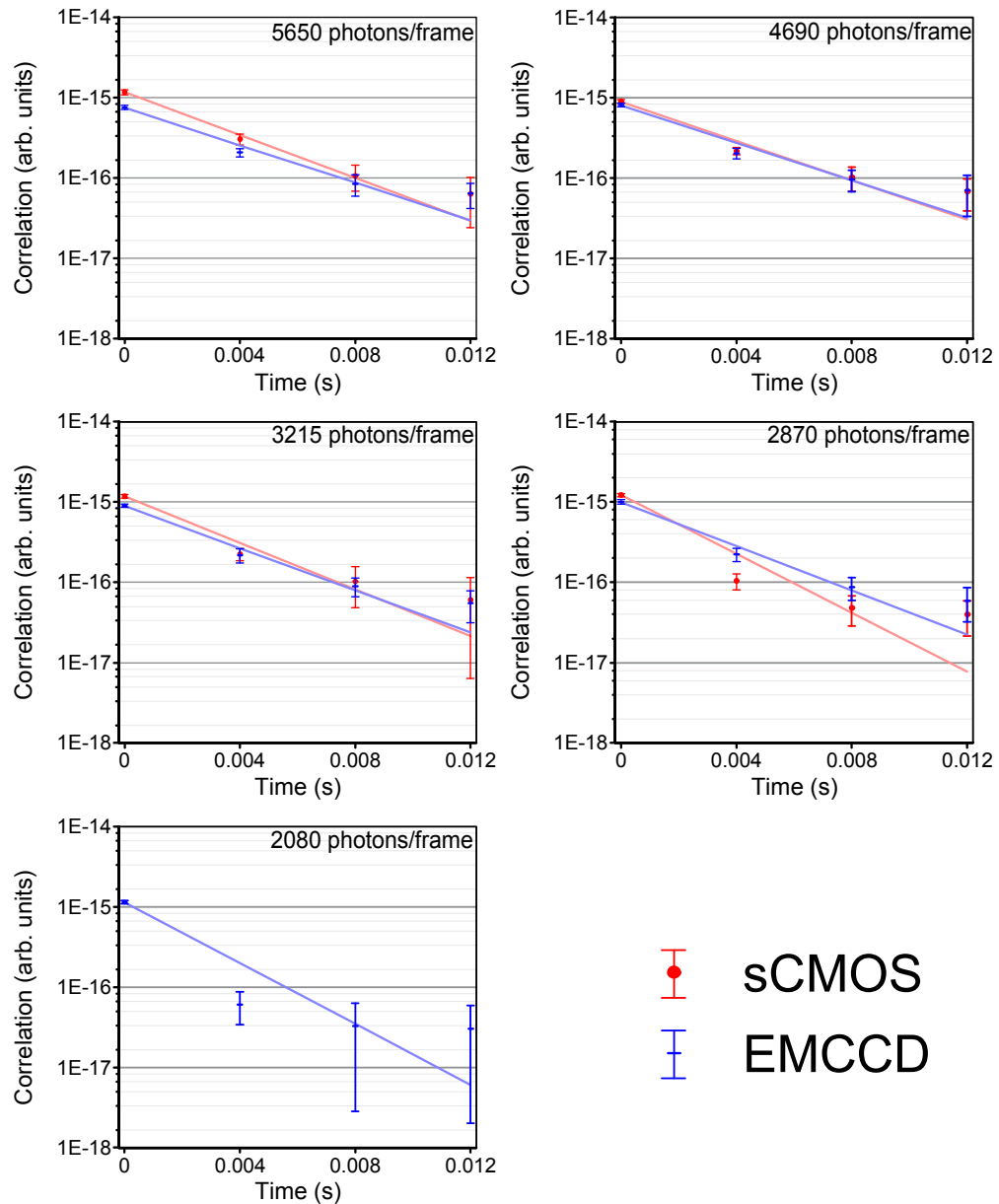


FIGURE 3.4: Autocorrelation against time graphs for the sCMOS and the EMCCD camera for different fluorescent levels. The x-axis is time (measured in seconds). At higher fluorescent levels, the cameras give similar results for the autocorrelation gradients and y-intercepts. At lower fluorescent levels the cameras are in overall agreement for what concerns the y-intercepts but not for the gradients. The error bars are one standard deviation over 10 samples of 4 second durations (equating to 1000 frames)

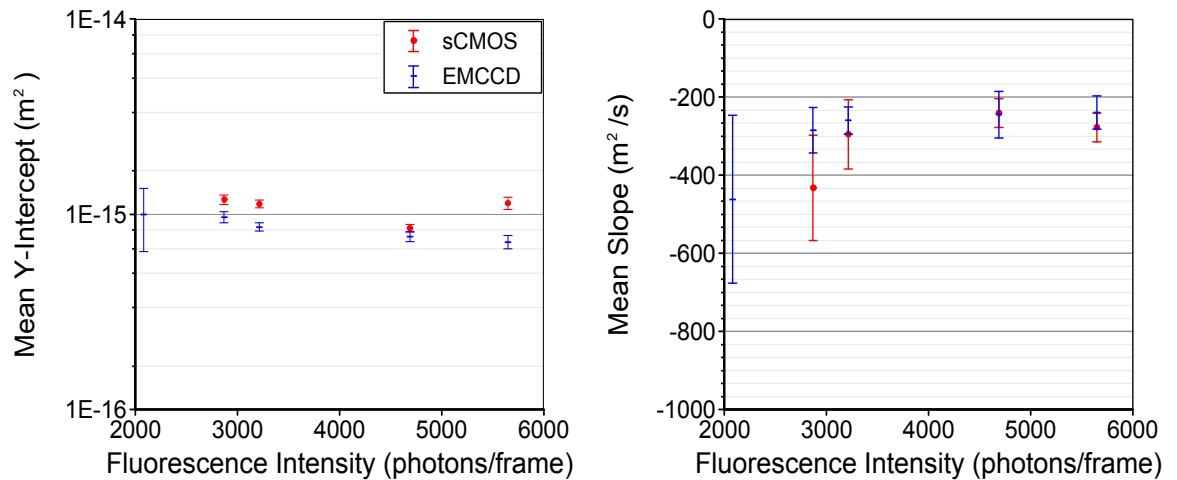


FIGURE 3.5: Graphs to show how the average autocorrelation gradients (left) and y-intercepts (right) change with respects to different fluorescent intensities, as well as their standard deviations. What we would hope to see is both a constant y-intercept and gradient, as the trap power and stiffness is constant throughout the experiment. What we find is that at higher fluorescence intensities (more than 3000 photons/frame), the two cameras yield autocorrelations that are in close agreement with each other, both in terms of their y-axis intercepts and gradients. This changes at lower intensities where it is evidence to suggest that the sCMOS camera slightly underperforms the EMCCD especially in terms of the gradient of the autocorrelation, until at the lowest intensity it proved impossible using the sCMOS camera to record images of sufficient quality in which to run standard centroid tracking algorithms, therefore no autocorrelation could be calculated. At low intensities the EMCCD camera images were of a sufficient quality to measure the standard deviation of the bead motion, but the gradient of the autocorrelation was subject to significant uncertainty.

function can be seen in figure 3.8. Therefore, we had to carefully consider how many data points to include in the fit.

The averaged autocorrelations from the two cameras are compared in Figs. 3.4, for five different fluorescence intensities ranging from approximately 2000-6000 detected photons/frame. In figure 3.5, we chart the change in the gradient and y-intercept with respects to the fluorescence intensity. We find that at higher fluorescence intensities (>3000 photons/frame) the two cameras are in close agreement autocorrelation wise, both in terms of their y-axis intercepts and gradients. At the very lowest fluorescence intensity (~2000 photons/frame) there is so little fluorescence that the sCMOS camera was unable to produce images of sufficient quality for standard centroid tracking

algorithms to work properly, and therefore no autocorrelation could be calculated. Factors affecting the quality of the images include the low amount of fluorophore coating on the silica beads and the camera shot noise.

When using the EMCCD camera at lower fluorescence intensities (just over that 2000photons/frame), the images were of a sufficient quality to detect the bead and measure a standard deviation of the bead motion (as seen in figure 3.4). One could therefore conclude that the EMCCD slightly outperforms the sCMOS. However, at the lower fluorescence intensities, there was a significant uncertainty to the autocorrelation gradient, which therefore would give skewed results for trap stiffness. If we are to take that in mind, both cameras perform the role of tracking a fluorescence bead equally.

We should also consider the cost of the cameras. The EMCCD camera can be up to 4 times more expensive than the sCMOS, and so not all research facilities can afford one. Also, most fluorescence experiments already use sCMOS cameras. Therefore, it would be fair to conclude that for future fluorescence tracking experiments, where we need to measure the MSD, there would be no need to spend extra money on a new EMCCD camera, as it would not offer any new or extra information about the experiment.

As an example we plotted the power spectra data for both cameras with the same particle tracking data as used to plot the autocorrelation with a fluorescence level of approximately 4690 photons/frame, as seen in figure 3.7. Here we can see that, due to noise, the corner frequency can not be easily determined. In this case the resulting measurement of the optical trap stiffness is less reliable than that determined from the autocorrelation data.

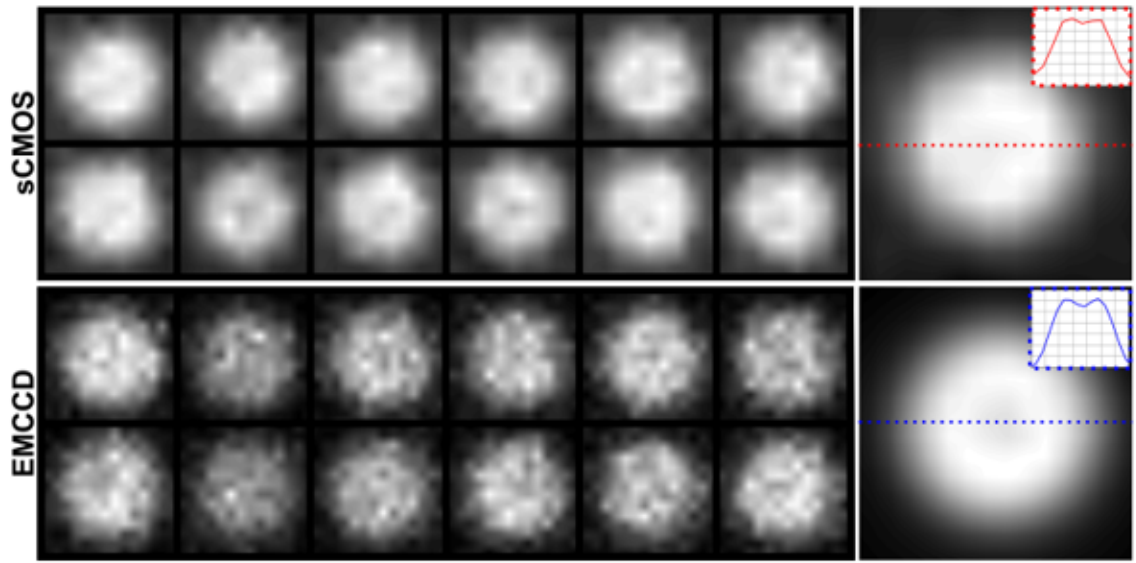


FIGURE 3.6: Single frames and summed successive co-registered frames images (left and right respectively) at a fluorescence level of ~ 5650 photons/frame. Images at the corner of the summed image represent the intensity at the cross-section of the summed image (the dotted line). The summed images appear circularly symmetric, with a slight reduction in intensity at the centre (as seen in the intensity cross-sections) due to the bead being surface labelled. The central reduction in intensity should therefore not affect the numerical calculation of the centroid position.

3.4 Discussion

In this work we have compared the performance of EMCCD and sCMOS cameras for tracking fluorescent beads within an optical tweezer. We found that our sCMOS camera has a comparable performance to our EMCCD camera at light levels more than 3000 photons/frame. At these light levels both camera types give images of sufficient quality from which the autocorrelation of the position of the trapped bead can be calculated. However, at extremely low fluorescent intensities both camera types have limitations. These limits are close to those expected in the nature of the noise arising from the finite number of photons. The detection of individual photons would be expected to be distributed over the diameter of the bead ($2r$) hence the accuracy to which the bead centroid can be measured is given by approximately r/\sqrt{N} , where N is the number of detected photons in the frame. In the case of

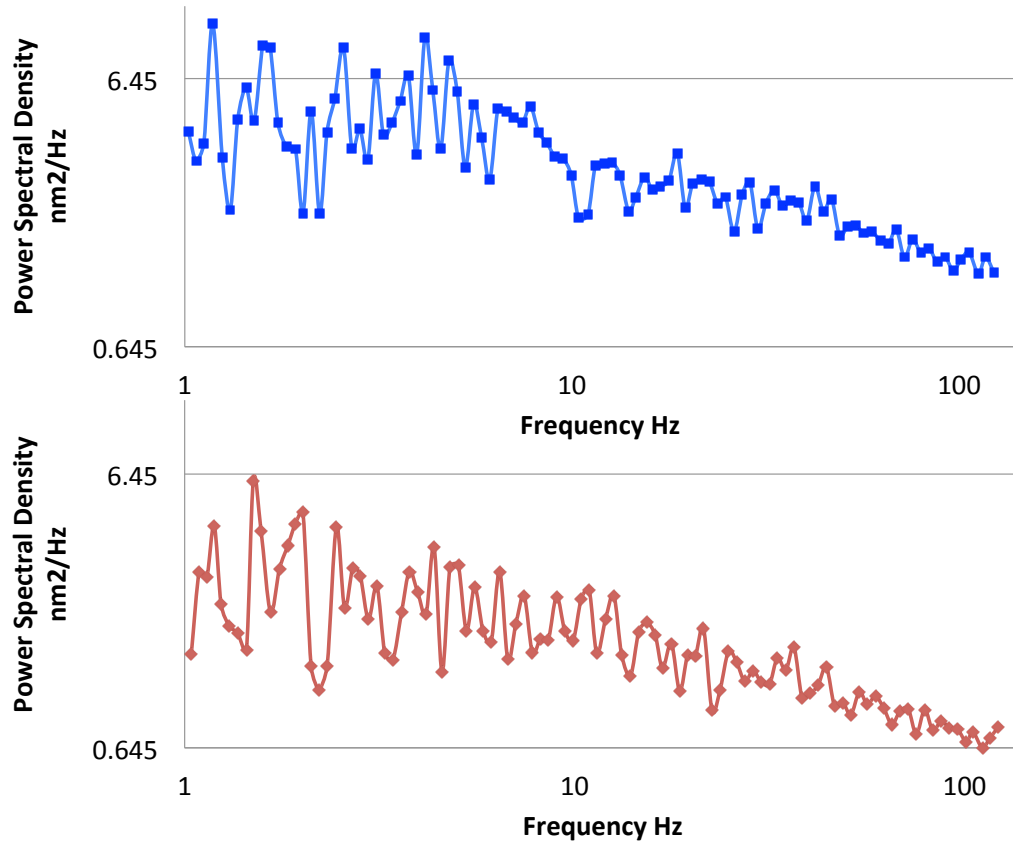


FIGURE 3.7: The power spectra produced by the tracking data for the EMCCD camera (above) and the sCMOS camera (below) at a fluorescence level of approximately 4690 photons/frame. Note that the spectra are very noisy, and although not impossible, much more difficult to read a corner frequency than a gradient on an autocorrelation.

Figure 3.8, where r is equal to $0.75\mu\text{m}$, and (if we assume all photons come from the bead itself) N is equal to 4690 photons, the approximation of noise is 10.5nm . This is in agreement with the noise level in said figure, Figure 3.8, as the noise is averaged around a correlation level of $1.1 \cdot 10^{-16}\text{m}$, which is approximately the square of 11nm .

It is not necessarily true or fair to state that the distribution of the detected photons is unbiased due to bead location and orientation, just by looking at the bead image itself. For example there could be a non uniform fluorescence caused by a non uniform fluorophore coating. Such biases in our detection could in principle lead to a systematic error in centroid estimation. To rule out this possibility we summed successive single frame images of the trapped bead, and examined the fully summed

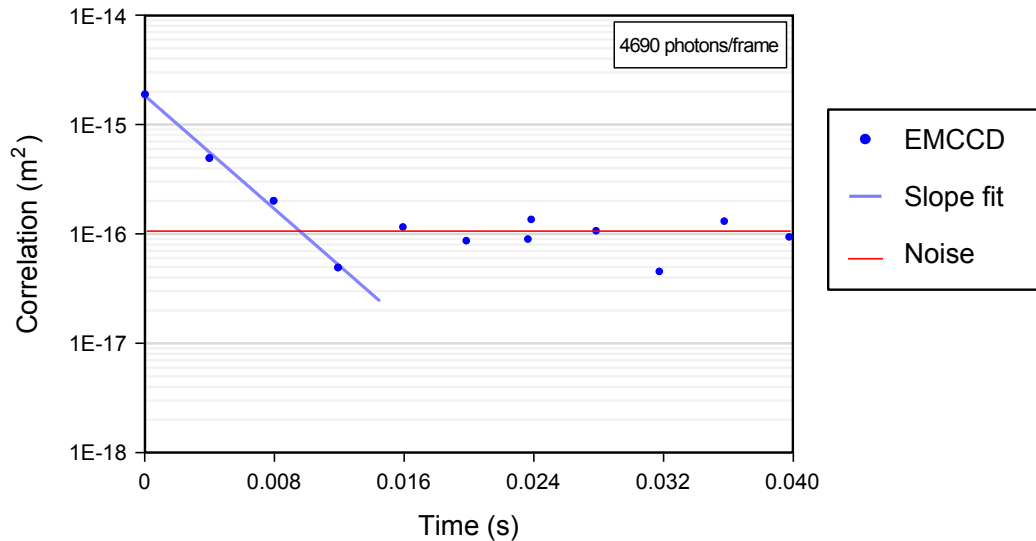


FIGURE 3.8: Autocorrelation function obtained from 4s interval of data (1000 frames) using the EMCCD camera at an intensity of 4690 photons/frame. The number of data points depends on the time taken between camera frames. The gradient of the autocorrelation is determined by fitting to the first 4 data points. If more (noise) data points were used for the fit, the gradient would be skewed.

image to see if we could detect spatial structure (as seen in Figure 3.6). We found the summed image smooth with no internal structure and to be circularly symmetric, albeit with a slight reduction in intensity at the centre. However, this central reduction in intensity does not affect the numerical calculation of the centroid position.

This central reduction in intensity could be due to the centre of the bead being the closest part of the bead to the camera and therefore being slightly out of focus. When we use centroid tracking, we desire a sharp clear symmetrical image to track, hence the image desires a sharp circumference. When looking at the 2D image of the bead, the centre of the bead would have been closer to the camera, so that the middle of the bead would be in focus, giving a sharp symmetrical image to track. This would mean that the centre of the bead was closer to the camera than the bead image circumference was (that distance being the radius of the bead), hence making the bead centre slightly out of focus, and the camera unable to detect all the fluorescence.

We have also showed that the best way to measure trap stiffness in this process is

to use the autocorrelation. In figure 3.7, we can see just how much the noise of the system can effect the results, as well as longer frame rates. There is a great deal of noise in fluorescence systems, due to the limited number of photons, which affects our results when using the power spectrum technique to find the optical trap stiffness κ . As mentioned in section 3.1, it is the corner frequency of the spectrum that provides optical trap stiffness information. If we are not able to reliably fit the Lorentzian, and the corner frequency of the spectrum is difficult to determine, it is more difficult to calculate κ , and the result is more likely to be skewed. Our autocorrelation results are less affected by this noise, and thus for future reference, autocorrelation can be a viable method to use when position tracking particles in low light applications such as fluorescence.

3.4.1 Validation by comparing fluorescence tracking to bright-field

Finally, we wanted to see if tracking in fluorescence gave a fair comparison to tracking in the more generic brightfield mode, and see whether the two modes would give similar results and answers when using the same bead sample specifications. To do this we directly compared the autocorrelation measure from centroid tracking data from the fluorescence sCMOS image at a high photon level(>5000 photons/frame) to bright field CMOS camera (Dalsa Genie gigabit ethernet) images. This is the camera setup we usually use on our Optical Tweezer brightfield experiment. As before with the scientific camera comparison, both measurements were taken with data with the cameras running at 250 frames per second, but at a slightly higher trap power (causing a shift in the y-intercept of the autocorrelation as seen in figure 3.9) due to the experimental conditions being slightly altered.

We were able to confirm that the fluorescence mode gives similar results to the more general brightfield mode approach (again, as seen in Figure 3.9). This therefore shows that the centroid tracking procedure of our bead's fluorescence, rather than the bead itself, is a valid approach for monitoring the motion dynamics of optically trapped beads. As there is no difference in the results between brightfield and fluorescence for symmetrical objects and there appears to be no restrictions to a fluorescence mode other than frame rate (that is considerably improved using scientific cameras), it is a simple assumption to make that for non-symmetrical objects, such as cells and bacteria, a fluorescence mode using a scientific camera would be more desirable than using the more general approach of a CMOS camera in brightfield.

3.5 Conclusion

We conclude not only that centroid tracking of our bead's fluorescence is a valid approach to monitoring the motion dynamics of optically trapped beads, but that in imaging with limiting light levels, the latest scientific cameras can be used to increase the frame rate of the tracking data, and therefore increase the quality of results in trapping experiments and research. We found that our sCMOS camera has a comparable performance to our EMCCD camera at light levels less than 3000 photons/frame. If the circumference of the bead is 10 pixels, we can calculate that this light level corresponds to approximately 40 photons/pixel.

However there are limits under this level for both cameras. Scientific cameras are able to work at a frame rate approximately 10 times greater than that of a traditional CMOS or CCD at lower light levels, when the camera's field of view is decreased. Therefore at lower light levels, it would be better to use a scientific camera rather than a generic CMOS or CCD, and at extremely low light levels (between 2000 and 3000

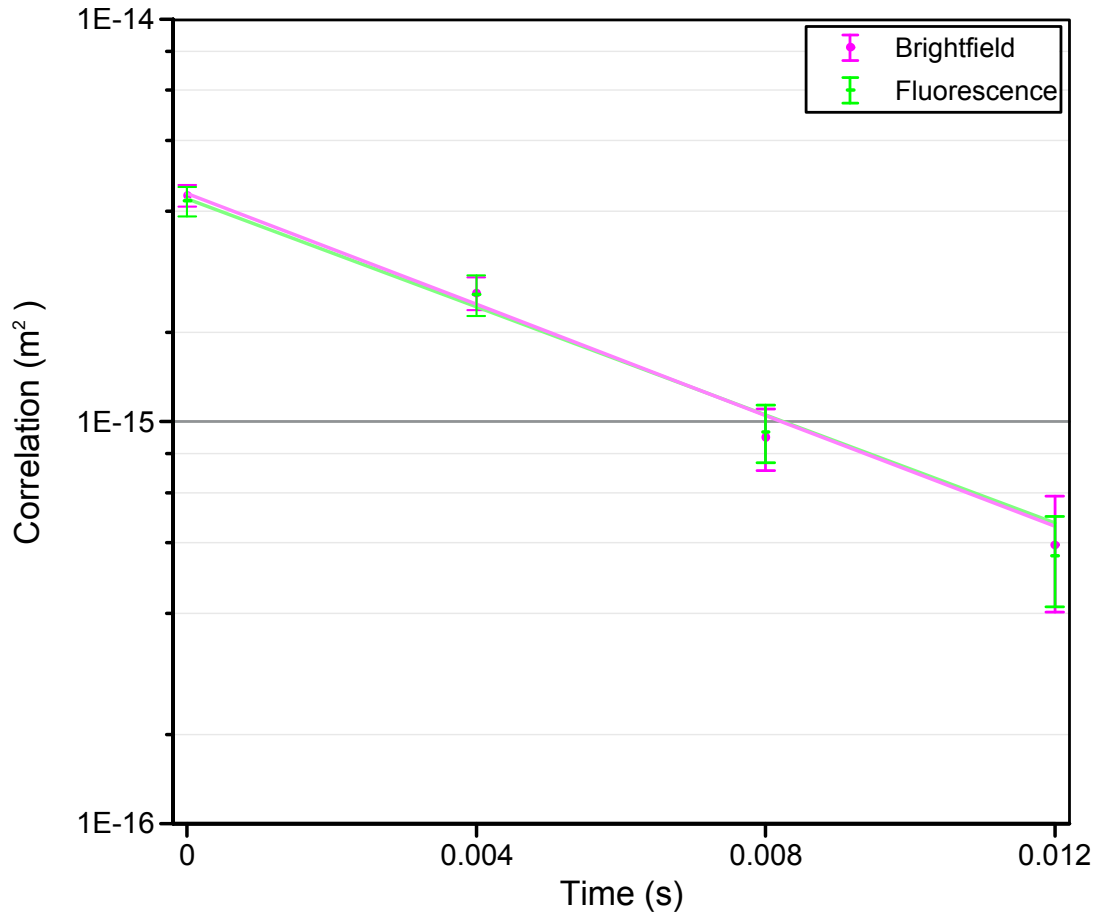


FIGURE 3.9: Autocorrelation against time graphs for the sCMOS with fluorescence (at a photon level of >5000 photons/frame) and brightfield centroid tracking data. Again, a 40s dataset was divided into 4s intervals, the autocorrelations being calculated for each interval and then averaged over each dataset. The camera gave similar results for the fluorescence and brightfield tracking.

photons/frame corresponding to approximately between 27 and 40 photons/pixel) it is better to use an EMCCD. At light levels lower than this, neither camera is detecting enough photons to produce images of the bead that allows reliable centroid tracking to occur. This level appears to agree with the Signal to Noise Ratio (SNR) for EMCCD and sCMOS comparison graphs that Andor provide, where they believe the performance of the EMCCD and sCMOS crossover at 55 photons/ pixel, with 2x2 binning [59].

One negative to using fluorescence tracking is the problem of photobleaching the

sample during the measurement, where the fluorescence dye on the sample is permanently unable to fluoresce. This is due to a photochemical change in the structure of the fluorophore which depends on the quantity of light hitting it. The process is irreversible. The lifetime for the Green Fluorescent Protein used in the experiment can be up to 10^5 photons, which meant we had limited time to use each sample, especially at higher fluorescence intensities.

We noticed that our samples only allowed us to trap 1 bead, and take a full set of measurements (such as in fig. 3.4), before photobleaching became a problem and the beads became noticeably dimmer. It was therefore decided that each time we performed the experiment with a new sample each time. To future account for photobleaching in the example, it would be best to use a fluorescence intensity ~ 3500 photons/frame, a lower intensity where both cameras agree. This is ~ 45 photons/pixel.

We also conclude that in low light applications, or those involving biological or non-Newtonian fluids, the optimum way to measure the optical trap stiffness is to use the autocorrelation function rather than finding the power spectrum.

Chapter 4

‘Lissajous-like’ trajectories in optical tweezers due to the competition between optical elastic forces and hydrodynamic interactions

This chapter is based on the work discussed in the Hay et al. Optics Express paper “‘Lissajous-like’ trajectories in optical tweezers” [5]. This was a collaboration with David Phillips, where I was in charge of the experimental part of the work. This included setting up a new static optical trap on an already established Holographic Optical Tweezer system, writing new SLM code to sinusoidally move the holographic optical trap, running the experiments, collecting data and analysing it using Labview and Matlab. David Phillips went on to simulate the conditions to see if it was in agreement with the experimental results.

The experiments described in the previous two chapters did not necessarily require a Holographic Optical Tweezer (HOT) setup to gain the results we got. However it was desirable, as HOT brings ease of use and more accurate control of the position of the optical trap (if needed) using computer control. However, in this chapter, HOT was essential for the experiment to work. Not only does SLM hologram allow multiple traps and ease to change the trap position [60], it also allows the user to program the SLM so that it can move a microscopic bead can be moved smoothly along a predefined trajectory.

There is much interest in producing less invasive trapping, especially within biological experiments. One area researchers are looking into is how some water-living microorganisms living in low Reynolds number environments, move in water. What they find is that they are able to break time-reversal symmetry of a hydrodynamic flow path. With this knowledge, it may be possible to mimic some of these processes so that we can produce some sort of ‘hydrodynamic’ trapping. This would mean producing time-varying hydrodynamic flows in close proximity to the particle being trapped.

In this chapter, we design a simple set-up to demonstrate how some of the time-reversal and non-time-reversal time varying hydrodynamic flows would affect a ‘probe’ bead in close proximity to the flow. We question whether hydrodynamic trapping could be a viable option when it comes to future biological trapping experiments. We used an SLM to move a bead sinusoidally along different trajectories, which would produce a hydrodynamic flow, whilst tracking and measuring the position of another trapped bead in close proximity which this flow would be acting on. This chapter uses a bead as a model system, that allows us to learn useful knowledge which has useful applications in Micro-biology . The chapter has applications in flow sensing [61–63], and is also related to the techniques of active micro-rheology [64–66], highlighting a mechanism by which stationary ‘passive’ optical traps can perturb the environment

that they are in place to measure, where future work could be done in.

Here we reference the abstract of Hay et al. paper:

When a microscopic particle moves through a low Reynolds number fluid, it creates a flow-field which exerts hydrodynamic forces on surrounding particles. In this work we study the ‘Lissajous-like’ trajectories of an optically trapped ‘probe’ microsphere as it is subjected to time varying oscillatory hydrodynamic flow-fields created by a nearby moving particle (the ‘actuator’).

We show a breaking of time-reversal symmetry in the motion of the probe when the driving motion of the actuator is itself time-reversal symmetric. This symmetry breaking results in a fluid pumping effect, which arises due to the action of both a time-dependent hydrodynamic flow and a position-dependent optical restoring force, which together determine the trajectory of the probe particle. We study this situation experimentally, and show that the form of the trajectories observed is in good agreement with Stokesian dynamics simulations. The simulation method we chose has been used in previous work, and has correctly accounted for hydrodynamic interactions in a variety of many particle systems, and is widely used in the literature. Our results are related to the techniques of active micro-rheology and flow measurement, and also highlight how the mere presence of an optical trap can perturb the environment it is in place to measure.

4.1 Introduction

In this chapter we initially wanted to see how very simple hydrodynamic interactions can affect optically trapped beads in a low Reynolds number environment. We wanted to see if a force produced by the hydrodynamic interaction would be strong enough to ‘trap’ another bead in close proximity. The research resulted in us looking to see how

the competition between the Hookean elastic optical force produced by an optical trap and the time-varying hydrodynamic interactions around it can affect a trapped bead’s position with respects to the trap centre over time, in a Low-Reynold’s number environment, such as those in our samples.

Reynolds number is dimensionless quantity, as defined as the ratio between the inertial forces and viscous forces acting on an object:

$$Re = \frac{\rho\nu L}{\mu} \quad (4.1)$$

where Re is Reynolds number, ρ is fluid density, ν is velocity of the fluid with respect to the object, L is linear size of the object, and μ is the dynamic viscosity of the fluid. We as humans live in a high Reynolds number environment, as the inertial forces dominate over viscous drag forces. However, not every living organism lives under high Reynolds number conditions. Most bacteria living in water live in low Reynolds number environments, as water is very viscous to microscopic objects and the viscous forces dominate over the bacterium’s inertial forces [67]. For humans, living in an environment like this would be similar to our atmosphere being of the consistency of maple syrup, making movement slow and causing objects to come to rest almost instantaneously after a force is applied. Low Reynolds number environments would normally cause counter-intuitive effects for them [68].

Some water living bacteria have evolved so that they do not need to rely on inertial forces to be able to move (unlike movement on the macroscopic scale). They use swimming techniques such as corkscrewing motions or the beating of cilia [69, 70]. However, these techniques are not fully understood physically, as some must involve

periodic deformations that break time-reversal symmetry, to which to say the hydrodynamic flow produced by the deformation would not be identical to the flow if time was reversed.

This chapter shows the time varying trajectories of a constrained trapped microsphere that is hydrodynamically interacting with another. This is a very simple model of how some micro-swimmers may act under time-varying viscous hydrodynamic forces. We exert a time-varying hydrodynamic force on a static optically trapped ‘probe’ bead by driving a Holographic Optically Trapped (HOT) ‘actuator’ bead in a sinusoidal fashion in close proximity, thus producing a fluid flow. We assume that the trap stiffness is constant and equal in x and y throughout trajectory. For the static trap, κ in x is equal to κ in y . We explore the resulting trajectories that are executed by the probe under a range of time varying configurations of the actuator path. Even in this fairly simplistic system we produce unexpectedly rich and potentially counter-intuitive behaviour, like bacteria living in low Reynolds number environments in the real world, which can help facilitate the development of artificial micro-swimmers and fluid pumps, and inform the growing field of microrobotics [71–74].

In particular we contrast two different experimental configurations, as seen in figure 4.1: firstly when the actuator is driven around a non time-reversal symmetric trajectory (circular motion), and secondly, when the actuator’s trajectory is time-reversal symmetric (periodic horizontal motion). We show that when the probe is trapped by the stationary optical trap, the probe travels along a closed loop ‘Lissajous’ like trajectory. Lissajous curves are a family of curves that are described using parametric equations. They are always closed paths (as our trajectories are).

We also show that certain actuator trajectories could cause the breaking of time reversal symmetry of the probe’s trajectory. Our work has applications to flow sensing, such as optical velocimetry in microfluidic systems and direct optical monitoring

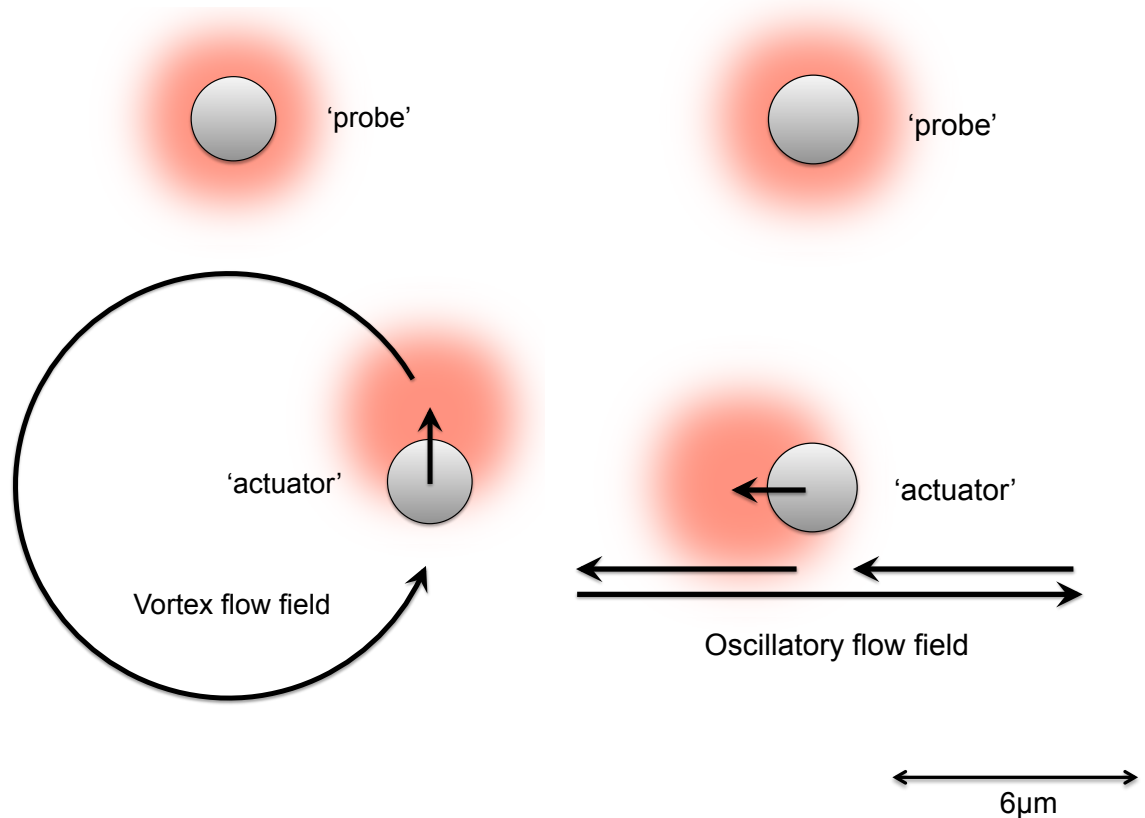


FIGURE 4.1: Examples of the two main ‘actuator’ bead paths with respect to their corresponding ‘probes’. The left shows the circular non time-reversal (the path going forward in time is not identical to the path that would go back in time) symmetric actuator path. The right shows the horizontal time-reversal (the paths going forward in time and backwards in time are identical) symmetric actuator path.

of flow generated by flagellar [61–63]. It is also related to the techniques of active micro-rheology[64–66], and highlights a mechanism by which stationary ‘passive’ optical traps can perturb the environment that they are in place to measure.

4.1.1 The Langevin Equation

For sample particles suspended in Newtonian fluids, assuming particles are spherical and ignoring the rotation of particles about their own axis (which can occur in an optical trap), the evolution of each degree of freedom of each particle in the system is governed by equation 4.2, also known as the Langevin equation [68, 75].

$$m_i \frac{d^2 x_i}{dt^2} = - \sum_{j=1}^{3N} (\xi_{ij} \frac{dx_j}{dt}) + \kappa_j (\delta x_j) + \sum_{j=1}^{3N} \alpha_{ij} f_j \quad (4.2)$$

where i and j index the degrees of freedom of all particles (i.e. three translational degrees of freedom for each of N particles), m is the particle mass, x denotes the coordinate of a particular degree of freedom, and t is time. ξ is the friction tensor used to describe the friction of the whole system of particles, κ is the stiffness of each optical trap, δx is the displacement of the particle from the centre of its associated optical trap, f is a stochastic force due to Brownian motion, and α is a tensor describing the coupling of Brownian fluctuations on nearby particles (which can be calculated from ξ). The left hand side corresponds to the inertial forces, and the right hand side corresponds to the viscous forces.

The left hand side (LHS) Equation 4.2 is equal to the mass of the particle multiplied by its acceleration, which describes the resultant force on the particle. At low Reynolds number limit, this inertia is negligible compared to viscous forces (Equation 4.1). As the LHS corresponds to the inertial forces, it can be set to zero. The first term on the right hand side (RHS) describes external forces, such as hydrodynamic drag forces, on each particle, encapsulating both the damping of a particle’s motion due to the surrounding fluid and the interactions with neighbouring particles through disturbances in the fluid. In the case of our system, this is the external time-varying hydrodynamic force produced by the water flow. The second term describes the optical restoring forces of the trap on each particle (assuming displacements are small so that optical force is linear with displacement and each particle only feels the effect of the nearest optical trap). In our case this is a static trap’s optical Hookean restoring force. The third term describes the Brownian motion of each particle, i.e. the stochastic Brownian kicks acting on the probe. As the LHS is always approximately zero, the resultant force on the RHS must also be zero.

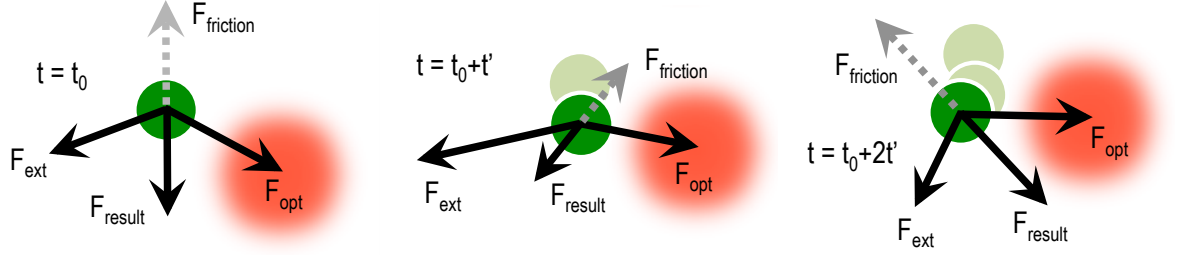


FIGURE 4.2: Schematic showing how a trajectory of a microsphere is calculated at each simulation time-step from the balance of external forces, F_{ext} (such as hydrodynamic and stochastic thermal forces), optical forces, F_{opt} , and frictional forces, $F_{friction}$.

This equation will be used later to numerically simulate our experiment. This can be done by using the Rotne-Prager tensor to calculate the friction tensor ξ [76]. We can use the Rotne-Prager tensor due to two main conditions in our experimental set up; a) our beads are spherical, b) the distance between two beads is much larger than the diameter of the bead itself. Another advantage to using the Rotne-Prager is that the tensor allows the first term to be expressed as functions of just the bead positions and velocities, and does not have to explicitly deal with fluid motion, making our simulation simpler to compute [77].

As the actuator is constantly moving, the evolution of the actuator path (and hence fluid flow) is broken into discrete steps. The steps are separated by a time that is much shorter than the relaxation time of the traps in the system (the time it takes for the trapped beads to relax back to the trap centre), but much longer than the relaxation time of the Brownian motion (the duration of the movement of the bead due to a Brownian kick), as we assume uncorrelated Brownian motion. With each iteration of the simulation, the forces on each particle are calculated, and therefore new positions of the particles a short time later are determined. As the

friction tensor ξ depends on the configuration of the particles, this is recalculated at each step for every new configuration. This is illustrated in figure 4.2.

This equation is very important as we are now able to simulate the system that will capture the hydrodynamic interactions of our micro-beads in water, along with the prescribed optical forces and Brownian motion. The simulation method used has been widely used in the literature, and has correctly accounted for hydrodynamic interactions in a variety of many particle systems [78–80]. It will also help us to understand the competition between the optical Hookean restoring forces and the time-varying hydrodynamic interactions. This will help to validate our experimental results.

4.2 Experimental Method

We trap two $5\mu\text{m}$ silica beads using the experimental setup shown in figure 4.3. Each trapped bead has a Hookean restoring force acting on it, equal to $-\kappa x$, where κ is the trap’s stiffness and x is the displacement of the bead away from the trap’s equilibrium position. We trap one of the beads (the ‘probe’) in a static trap, where κ_x is equal to κ_y , and trap a second bead (the ‘actuator’) in a holographic trap [81]. The stiffness of the actuator trap was approximately one order of magnitude larger than that of the probe trap. This is allowed for our setup as the stiffness of the actuator trap is not an important parameter in determining the behaviour of the system, as it was only the probe’s motion we were monitoring closely. As long as the actuator bead is trapped stiffly enough, the actuator will not escape the trap, and its motion will produce the time varying hydrodynamic force we desire. We assume that κ_x and κ_y do not vary during the actuator trajectory, as the single holographic trap is not near

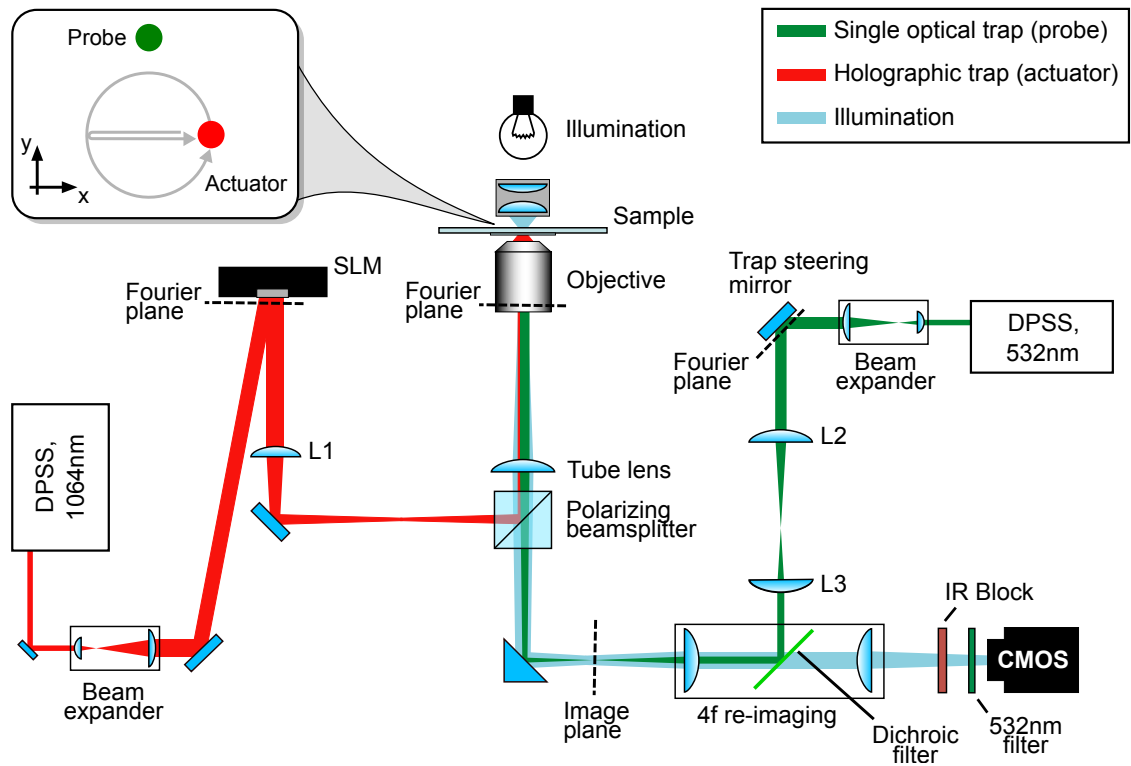


FIGURE 4.3: Schematic of the dual beam holographic optical tweezers system. Our optical tweezers system is built around a custom-made inverted microscope with a Zeiss halogen illumination module (100 Watt). The holographic actuator trap is created by expanding a diode pumped solid state (DPSS) infra-red 1064 nm wavelength laser beam to overfill a nematic liquid crystal spatial light modulator (SLM) (BNS XY series, 512x512 pixels, 200Hz frame-rate). The SLM is placed in the Fourier plane of the sample and telescopically re-imaged onto and overfilling the back aperture of the objective lens (Nikon 100 x oil immersion, 1.3 NA) using a Fourier lens (L1) of 250 mm focal length and a tube lens of focal length 100 mm. The single beam trap is provided by a green DPSS 532 nm wavelength laser. Its position can be manually controlled using a kinematic mirror mount, and the beam also overfills the back aperture of the objective lens. The sample is viewed using a high-speed CMOS camera (Dalsa Genie gigabit ethernet), and any reflected infra-red and green laser light is filtered out. The top left inset shows a schematic of the relative optical trap positions and trajectories within the sample.

the zero order, and limited light is reaching all other orders to reduce the risk of the actuator feeling any other optical forces.

We program the Spatial Light Modulator (SLM), controlling our HOT, to change the position of the trap using the ‘gratings and lenses’ algorithm [29] so that the trap is moving periodically at 2 cycles per second and with an amplitude of $6\mu\text{m}$. At one point we used a piezo mirror, and also considered using an Acousto-Optic Deflector (AOD) instead of an SLM, both of which we could vary the amplitude and frequency of [6, 23]. The piezo mirror only provided a limited range of actuator movement and two orthogonal AODs are required for control in x and y. The SLM provided the easiest method of smoothly controlling the bead over a path that was repeatable each time.

The periodic movement of the holographic trap moves the actuator approximately sinusoidally, causing the surrounding water to move, thus generating an external time-varying hydrodynamic force. This force is exerted on the probe. A hydrodynamic friction force is also produced during this procedure, which acts in the opposite direction to the external time-varying hydrodynamic force. Due to the constant changing balance between the external hydrodynamic, friction and trap’s optical restoring force, the probe is constantly being displaced by different force vectors. When the probe is constantly being displaced, the probe trap’s relaxation time (τ) is large compared to the time the particle experiences the force. The probe does not have enough time to relax back to the trap centre before being displaced again by a different force vector. This leads to the probe constantly moving in a closed trajectory with a varying velocity.

We track the position of the centre of the probe bead over a period of time using high-speed video tracking with a centre of symmetry tracking algorithm, thus allowing us to plot this probe trajectory [46]. During the tracking time, the probe travels the same

closed loop trajectory multiple times (>200). We average over all the trajectories the probe travels (as to average away the Brownian motion) using data processing, which results in an averaged, smooth experimental probe trajectory. The data processing included adding all of the trajectories together, and viewing all the positions the probe had been during the multiple trajectories. At this point we were able to calculate an average path. These average paths, with an example single path, are shown in figures 4.7 and 4.8.

Using a Matlab program with this probe position data, we are able to calculate the probe's changing magnitude and direction of the drift velocity and speed throughout its movement, and also calculate the occupancy of where the probe has been within the closed loop trajectory.

We start with periodic horizontal movement (a time-reversibly symmetric path) of the actuator with respects to the probe. The path then increases in the y direction until the actuator is moving with circular motion counterclockwise (a non time-reversibly symmetric path). Each actuator path has an amplitude of $7.5\mu\text{m}$ in x, and an amplitude in y ranging from 0 to $7.5\mu\text{m}$. The smallest distance between the actuator bead and probe bead within this set up is $\sim 7\mu\text{m}$ apart. We concentrate on the probe paths that correspond to the horizontal the circular actuator paths.

4.3 Results

4.3.1 Experimental

Figures 4.4 and 4.5 show the experimentally measured response of the optically trapped probe microsphere as it is subjected to the two types of time-varying external hydrodynamic forces produced by the actuator (along with the stochastic forces

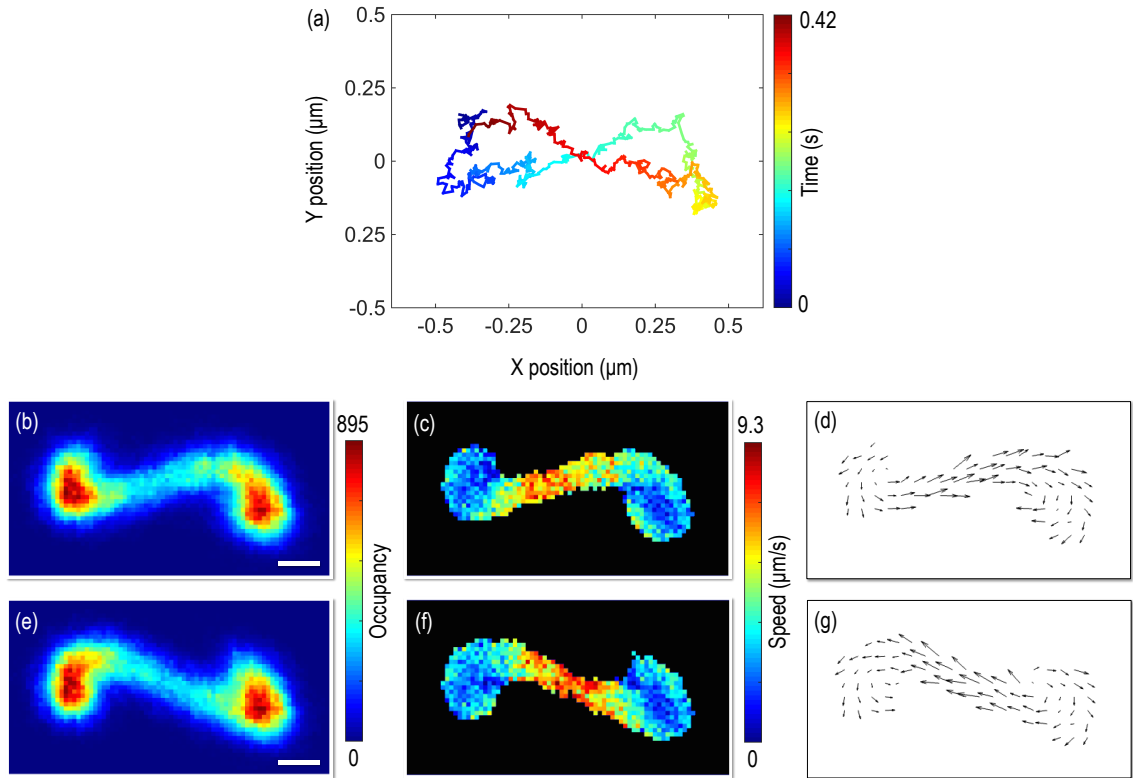


FIGURE 4.4: Experimentally measured probe microsphere trajectories when subjected to a time-reversible flow-field. (a) The trajectory of the probe over a single time-reversal symmetric actuator cycle. (b) and (e) 2D occupancy histograms showing the number of visits the probe made to each 10 nm wide bin over the course of 100 actuator cycles. The white scale bars represent 100 nm. (b) is the first half of the cycle, (e) is the second half of the cycle. (c) and (f) The average drift velocity of the probe as it passes through each 10 nm x 10 nm histogram bin. (d) and (g) The magnitude and direction of the drift velocity of the probe bead.

of Brownian motion). Figures 4.4(b) and 4.4(c) and figure 4.5(b) are occupancy histograms displaying the number of times the probe appeared in each bin of a 2D grid of 10 nm x 10 nm bins over 100 actuator cycles. For the horizontal actuator motion, the data is displayed in two plots to separate the probe's motion in the first and second half of each cycle, as it revisits the central region twice per cycle. The histogram occupancy maps are approximately inversely proportional to the probe's speed. We also calculate the average drift velocity of the probe as it passes through each histogram bin, which is shown in Figs. 4.5(c) and 4.5(d) and Figs. 4.4(c), 4.4(d), 4.4(f) and 4.4(g). We find the position of the bead at each time point. From here, we are

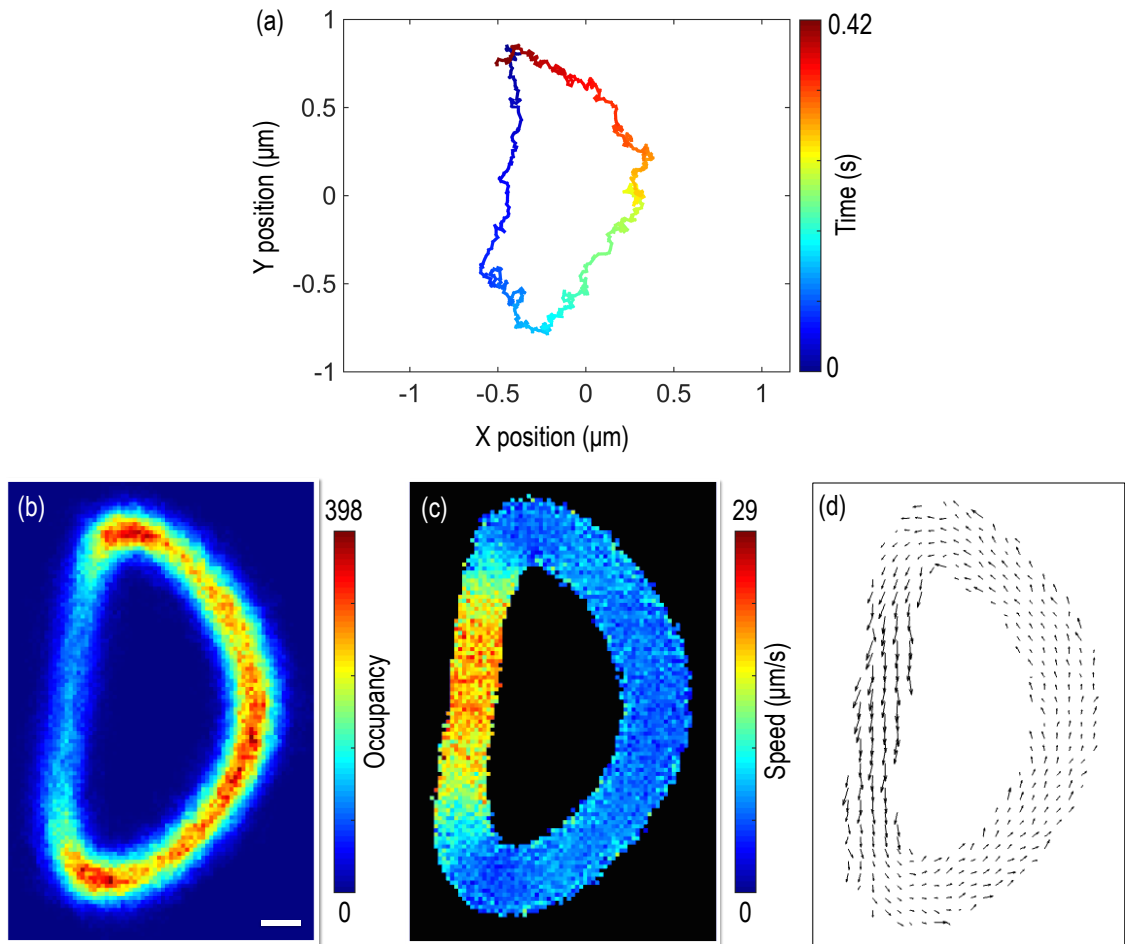


FIGURE 4.5: Experimentally measured probe microsphere trajectories when subjected to a non-time-reversible flow-field. (a) The trajectory of the probe over a single non time-reversal symmetric actuator cycle. (b) A 2D occupancy histogram showing the number of visits the probe made to each 10 nm wide bin over the course of 100 actuator cycles. The white scale bar represents 100 nm. (c) The average drift velocity of the probe as it passes through each 10 nm x 10 nm histogram bin. (d) The magnitude and direction of the drift velocity of the probe bead.

able to calculate an average velocity.

When the actuator bead is moving horizontally with approximate sinusoidal motion, the trapped probe bead appears to move sinusoidally in a figure of eight, with equal sized lobes. This is shown in figure 4.7, when the actuator is moving in the x direction at different z depths. At a height of $25\mu\text{m}$ above the surface of the sample, the trapped probe bead moves sinusoidally with amplitude of $\sim 0.8\mu\text{m}$ in the x axis, and in y moves with an amplitude of $\sim 0.2\mu\text{m}$.

When the actuator bead is moving away from a peak towards the centre of the sinusoidal movement, the hydrodynamic force acting on the probe is at its peak as the actuator is travelling at its fastest velocity in the cycle, and the distance between the actuator and probe is at its smallest, meaning the hydrodynamic force produced by the moving actuator will affect the probe more. This moves the probe bead in the x direction, and also a little in the y direction. As the actuator bead starts to travel away from the trap centre towards an end of the trajectory path again, its velocity decreases, leading to the hydrodynamic external force to also decrease. This balances with the optical Hookean restoring force. At this point, the probe moves in y, but has little movement the x direction. As the actuator then reaches the peak of its cycle, the restoring force of the trap is much larger than the hydrodynamic external force, and the probe bead moves back towards the centre of the trap. This is explained in figure 4.11.f

As the actuator bead moves towards circular motion, one of the lobes of the probe's path becomes larger and dominates over the other, until the smaller disappears. The path then becomes pear shape when the ratio of vertical to horizontal amplitude is around 0.3. This pear shape then becomes 'D' shaped at a vertical to horizontal amplitude ratio between 0.5 and 0.6. This is shown in figure 4.6b.

When the actuator bead is under circular motion, the trapped probe bead appears to have a trajectory that looks 'D' shaped, as experimentally shown in figure 4.8, again when the actuator is moving in x and y at different z depths. At $25\mu\text{m}$ above the surface of the sample, the probe moves a distance $\sim 0.4\mu\text{m}$ in the x axis, and $\sim 0.9\mu\text{m}$ in the y axis. This is due to the time varying hydrodynamic force produced by the moving actuator bead balancing with the time varying restoring force of the probe beads optical trap. The resultant force is therefore also time varying. We map out the forces and trajectories in figure 4.11.

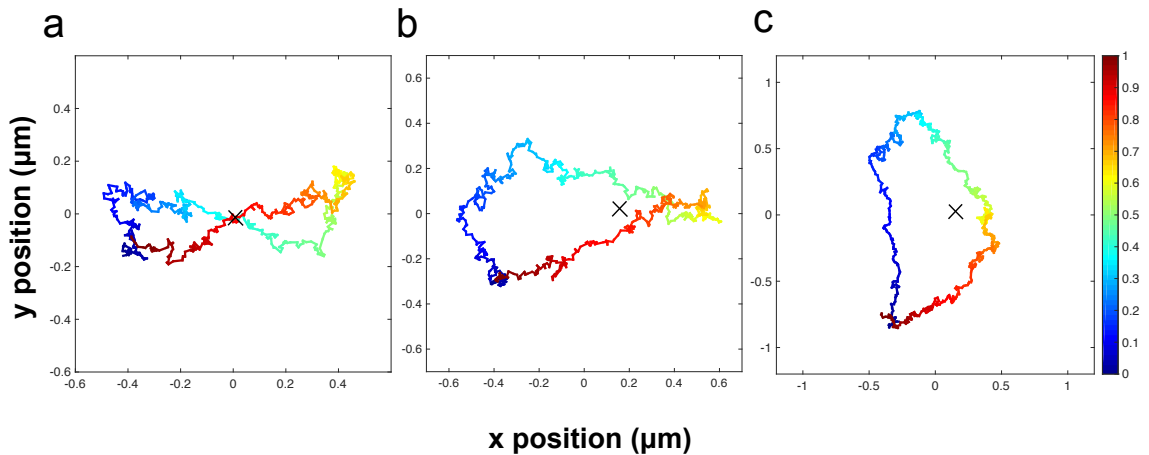


FIGURE 4.6: Experimental trajectories for (a) horizontal oscillatory actuator motion, (b) oscillatory actuator motion with x y displacement ratio equal to 5, and (c) circular motion respectively. 'x' on the experimental trajectory graphs represents the probe trap position. When looking at (a) we see a 'figure of eight' probe trajectory, where the probe moves in both x and y, even though, the actuator only moves in x. It moves a distance in x of around $1\mu\text{m}$, and in y of around $0.3\mu\text{m}$. When looking at (b), we see one of the lobes produced in (a) reduced in size. This happens until the lobe disappears entirely, to form the 'D' shape, as seen in (c). Again the horizontal distance of around $1\mu\text{m}$ in x, but now a $2\mu\text{m}$ in y.

The distance from the bottom of the sample can affect the size of the trajectory in figures 4.7 and 4.8. The further away the trapped beads are from the surface of the sample, the bigger the hydrodynamic force produced by the actuator is. The wall of the sample is unable to dampen the force. We also show in figure 4.9 that for the circular path, even if the angle between the actuator and the probe is changed, the probe path still gives the same trajectory.

If we were to reverse the circular actuator trajectory corresponding to going backwards in time, hence go clockwise, there would be a break in time-reversal symmetry. This breaking of symmetry would also be the case for the corresponding probe path, where the 'D' shape would be flipped around, and so the two trajectory paths are not the same forwards and backwards.

When looking at the horizontal motion, the actuator trajectory is the same both forwards and backwards in time. However, this is not the case for the corresponding

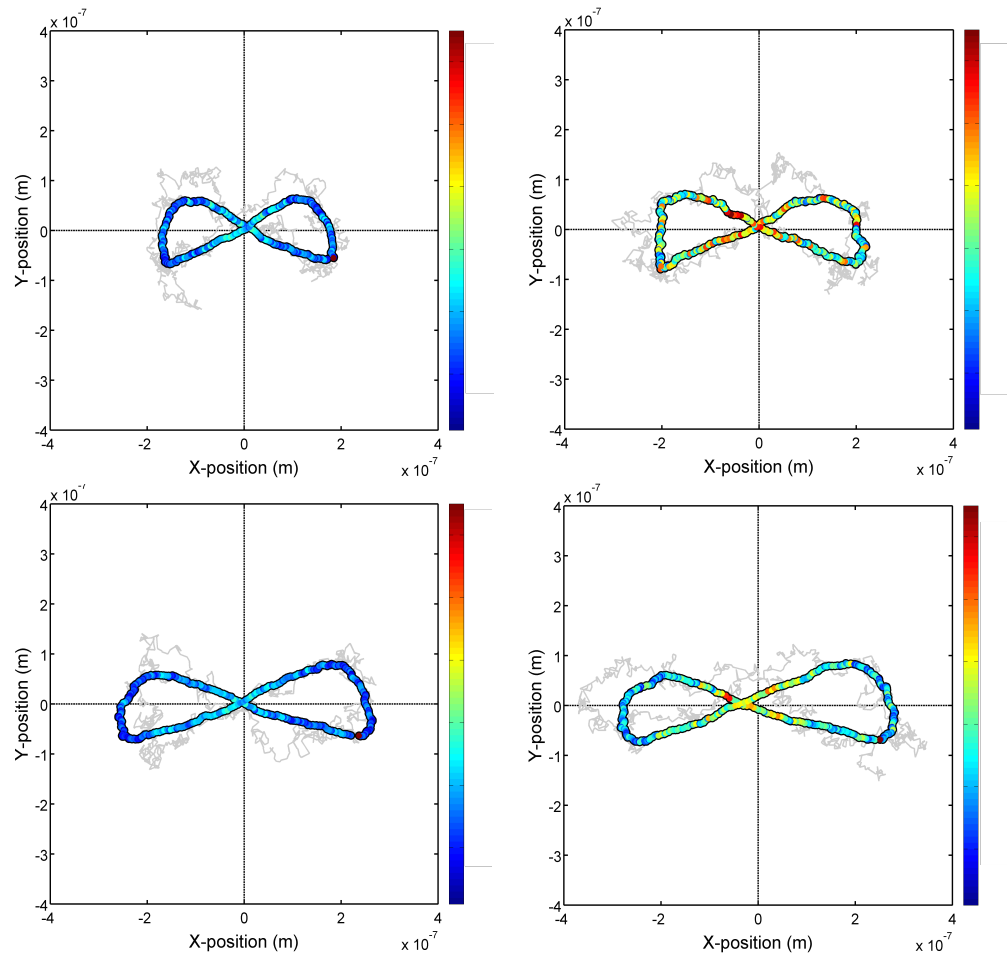


FIGURE 4.7: Averaged experimental trajectory of a trapped probe being driven by an actuator travelling with circular motion are at the same height of 10 (top left), 15 (top right), 20 (bottom left) and $25\mu\text{m}$ (bottom right) from the surface. Colour scale represents the velocity. Grey line represents a single trajectory before averaging. The average was taken over 200 trajectories. It appears that the trajectory get larger when it is moved away from the surface. This is due to less surface friction acting upon the bead.

probe trajectory, where the probe trajectories again would be a mirror image of each other. Thus, time-reversal symmetry is broken.

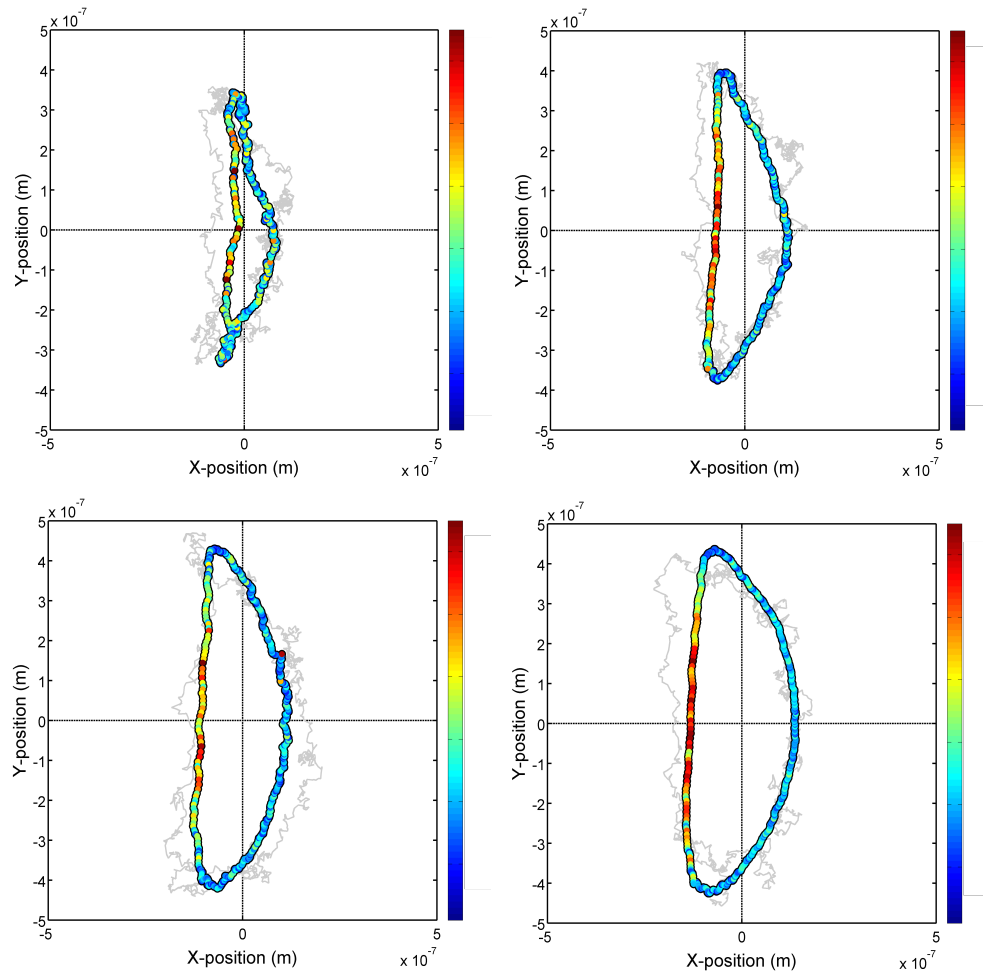


FIGURE 4.8: Averaged experimental trajectory of a trapped probe being driven by an actuator travelling with circular motion are at the same height of 10 (top left), 15 (top right), 20 (bottom left) and $25\mu\text{m}$ (bottom right) from the surface. Colour scale represents the velocity. Grey line represents a single trajectory before averaging. The average was taken over 200 trajectories. Again, it appears that when the probe moves away from the sample cell’s surface, the trajectory get larger. Again, this is due to less surface friction acting upon the bead.

4.3.2 Simulated

Assuming that the probe trap was conservative [82], we were able to simulate (using Equation 4.2) the two extremes of the system: static trapped probe path when the actuator was moving in the periodic horizontal path and the static trapped probe path when the actuator was moving with circular motion. We also simulated the movement of the probe when there was no trap present. We used the same size beads

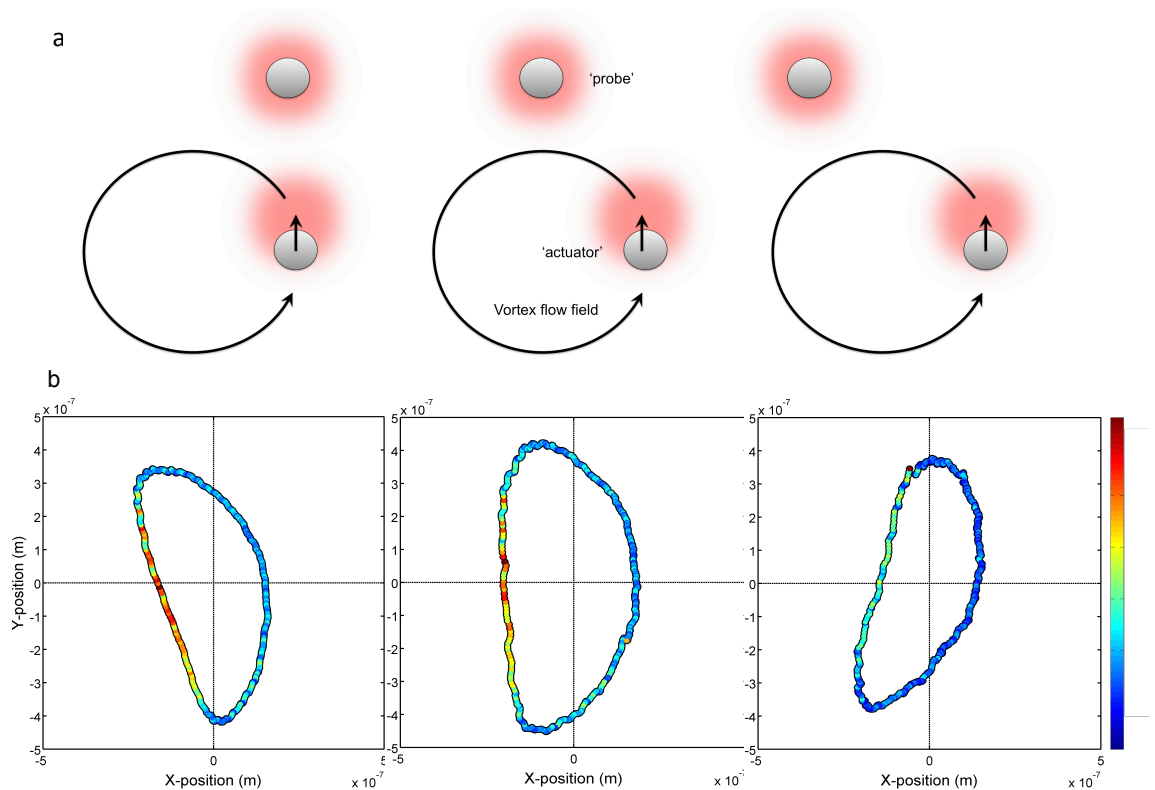


FIGURE 4.9: Averaged probe trajectories where the actuator paths are at different locations with respect to the probe. (a) Illustration of the actuator position and path with a circular system configuration with respects to the probe bead and trap (b) the corresponding experimental probe trajectories, with information about the speed the probe is travelling, using the colour velocity scale to the right of the charts. Note that all probe trajectories are ‘D’ in shape, only with some tilting occurring when the actuator trajectory is placed either to the left or the right of the probe. We find that the bead travels quickest when travelling in the y-direction and no movement in the x-direction.

and the same distances between traps as in the experiment. These results are shown in figure 4.10, and show a similar ‘D’ shaped probe trajectory for a circular actuator path and a similar ‘figure of eight’ probe trajectory for the horizontal actuator path.

From that, we have mapped out the relative positions of the actuator and probe microspheres through one actuator cycle for (a) the horizontal actuator trajectory and (b) the circular actuator trajectory. This is seen in figure 4.11. This shows the relationship between the two beads’ movements, and helps us to understand why the probe travels the way it does with respect to the actuators position and speed.

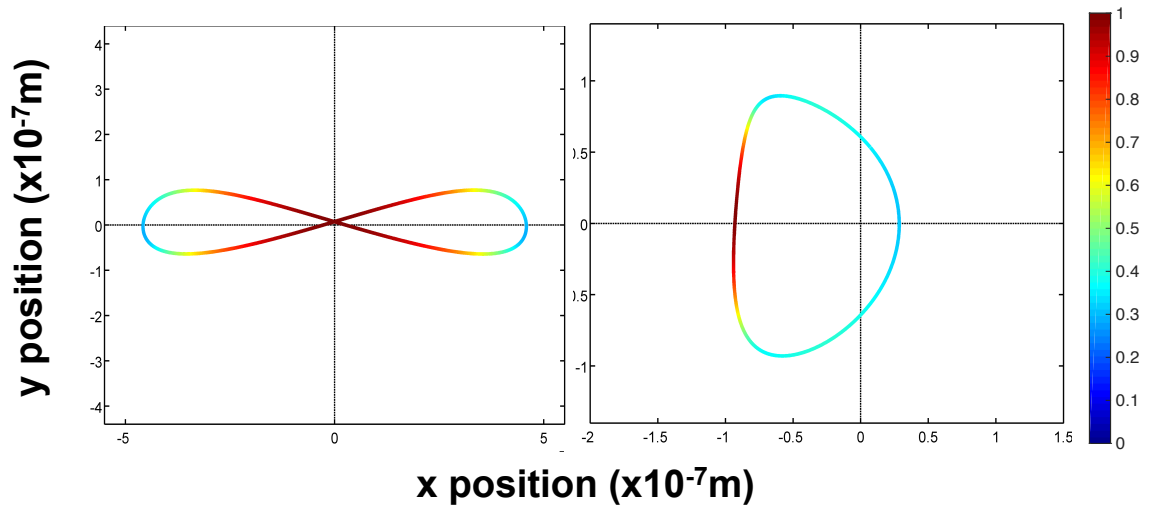


FIGURE 4.10: Simulated trajectories of the probe with respects to actuator paths. The left probe path corresponds to the time-reversal symmetric actuator trajectory (horizontal sinusoidal motion) and the right probe path corresponds to the non time-reversal actuator trajectory (circular motion). The zero point on the graphs corresponds to the trap centre. Colour chart corresponds to the beads speed during the trajectory, here the bead is travelling at its slowest when the path is blue, and quickest when its path is red.

4.4 Discussion

Let’s first look at the circular actuator path that already breaks time reversal symmetry. The actuator is driven in two dimensions (x and y) at a rate of 2 rotations per second and a horizontal and vertical amplitude of $6 \mu\text{m}$, causing a maximum speed during it’s trajectory of $75.4 \mu\text{m/s}$. Our actuator path is not time-reversible (it is not the same in both directions). The stationary optical trap constrains the motion of the probe causing the probe’s trajectory to transform into a closed asymmetric orbit around the position of the optical trap. The trajectory is defined by the changing balance between hydrodynamic, optical, and frictional forces, as shown in equation 5.11

Now let us look at the horizontal periodic actuator path and it’s corresponding hydrodynamic force. The actuator is driven in only one dimension, sinusoidally running in the x-axis at a rate of 2 rotations per second and a horizontal amplitude of $6 \mu\text{m}$.

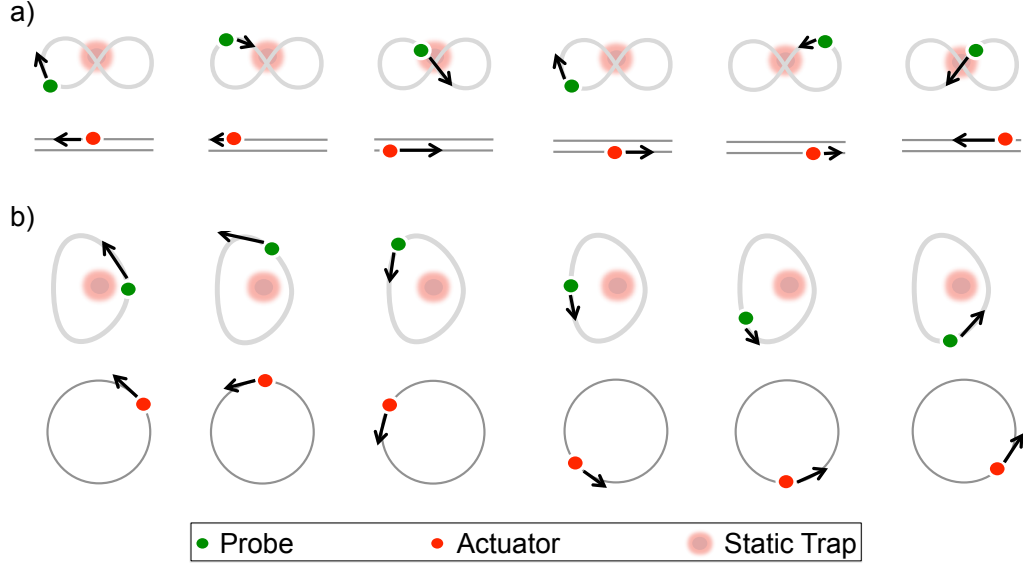


FIGURE 4.11: Illustrations showing the relative positions of the probe microspheres with respects to the position and movement of the actuator in its path for (a) the time-reversal symmetric actuator trajectory (horizontal sinusoidal motion) and (b) non time-reversal symmetric actuator trajectory (circular sinusoidal motion). Once again, for clarity, the relative size of the probe trajectory has been exaggerated compared to both the probe size, and the actuator trajectory.

Again, this causes a maximum speed of $75.4 \mu\text{m/s}$ in the x direction. This motion is symmetrically time-reversible (the same path would be followed if the direction were to be reversed), and if Brownian motion is ignored, the cycle-averaged hydrodynamic force would be approximately zero. When the probe is constrained by a static trap, we observe a ‘figure of 8’ trajectory as in the experimental results. We stress that the measured ‘figure of 8’ trajectory followed by the probe particle in this experiment is a *signature* of the breaking of time-reversal symmetry in the system. This trajectory can *only* occur if a small non time-reversible symmetric hydrodynamic flow is *also* generated. Here the symmetry is broken due to some small perturbation caused by the changing balance of the time varying hydrodynamic flow, the optical trap restoring force and the fictional forces, hence the time varying resultant force, as shown in Equation 4.2.

This would result in a weak pumping action of the system. As with the previous

trajectory, this trajectory is also defined by the changing balance between hydrodynamic, optical, and frictional forces, as shown in equation 5.11.

All of the probe trajectories from the corresponding actuator flows, differ from each other due to the difference in the time varying hydrodynamic force produced by the changing actuator bead path. Due to the changing balance between the external, friction and trap's optical restoring force, the probe is constantly being displaced by different force vectors. Because the relaxation time (τ) of the static trap is large compared to the time the particle experiences the force, the particle does not have enough time to relax back to the trap centre before being displaced again by a different force vector, causing the probe to constantly move. As the actuator movement is sinusoidal, the time varying hydrodynamic force will be repetitive, thus the resultant force exerted on the bead is also repetitive, causing the probe to travel along closed loop 'Lissajous' like trajectories.

The time varying resultant force exerted on the probe is visco-elastic, by which the resultant force is a combination of viscous forces from the hydrodynamic flow and optical elastic forces, from the optical trap restoring force.

Figures 4.7 and 4.8 show that when the probe and actuator move away from the sample cell's surface, the trajectory get larger. This is due to a decrease in the surface friction acting on the bead. These figures were taken from 50μ deep samples.

However, we should remember that at higher distances above the surface, we are creating a more complex hologram for our trap. Moving the trap deeper into the sample would create spherical aberrations, which could significantly decrease the trap strength, as not all the trapping power is being focussed to the same spot. One should also remember to take Faxen's law into account. Faxen's law relates the bead's velocity to the flow it experiences at low Reynolds number environments, and can predict roughly how close to the surface the particle needs to be to feel the boundary

impact on the hydrodynamic forces it is experiencing. These two problems would only come into account if the sample was deeper and the beads were further away from the surface.

4.4.1 Energy Transfer between the Probe and Actuator

One should also consider the importance of energy transfer within a symmetrically broken time-reversible system, and whether we would be able to measure the transfer of energy between the actuator and probe.

The flow-field created by the breaking of time-reversal symmetry is due to the storage of energy in the probe bead (by pulling it away from its equilibrium position) which is then dissipated into the surrounding fluid later in the cycle. As work done is equal to the force multiplied by the distance travelled, but the force is time-varying, we can measure this energy transfer by calculating the line integral of the hydrodynamic vector field. This is calculated using Equation 4.3, and can then be simulated. The simulated results are shown in figure 4.12.

$$W = \oint_C \mathbf{F}_{hydro}(\mathbf{r}) \cdot d\mathbf{r} = \oint_C \mathbf{F}_{hydro}(\mathbf{r}(t)) \cdot \frac{d\mathbf{r}}{dt} dt, \quad (4.3)$$

where $\mathbf{F}_{hydro}(\mathbf{r}(t))$ is the time-dependent hydrodynamic vector flow-field (which varies throughout the cycle), $d\mathbf{r}(t)/dt$ describes the velocity of the probe when at position $\mathbf{r}(t)$ along its closed loop trajectory, and t is time.

Equation 4.3 can be integrated numerically in our simulation, and the work done on the optically trapped probe microsphere under non time-reversal symmetric, and time-reversal symmetric driving configurations are shown in figure 4.12. The blue

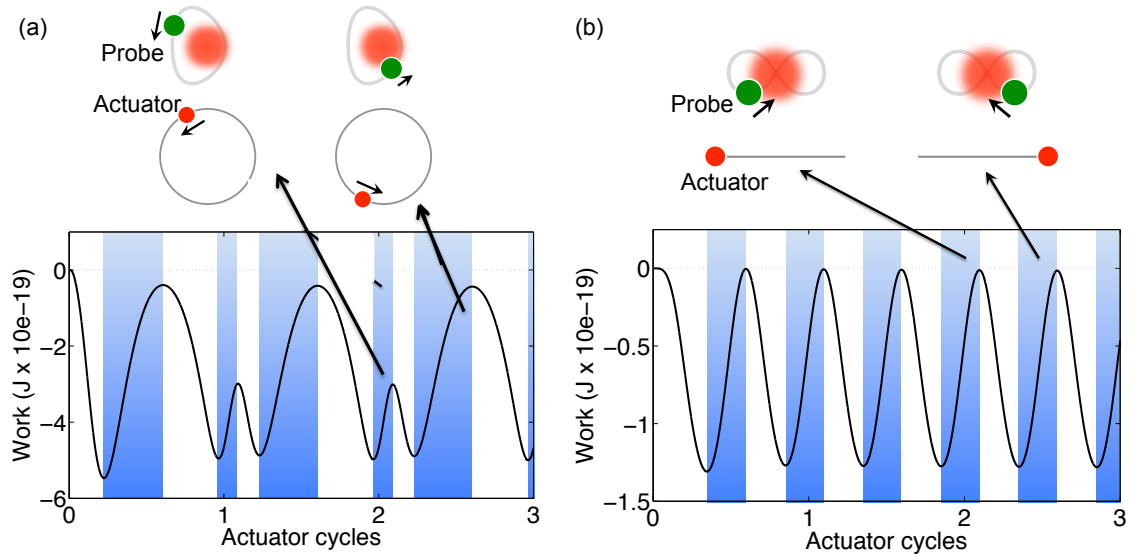


FIGURE 4.12: Simulation of the accumulated potential energy of the probe trap in the absence of Brownian motion for the (a) actuator in circular motion (non time-reversible symmetric) case and (b) actuator in periodic horizontal motion (time-reversible symmetric) case. Each case shows the evolution of the energy stored in the system when the probe is initially positioned at rest at the centre of the trap. Work is done on the bead in the white stripes, and energy is released by the bead in the blue stripes.

stripes show the points in the trajectory where energy is released, and the white stripes show the points in the trajectory where work is done on the bead.

In figure 4.12(a), the circular actuator trajectory, when the probe orbits the centre of the trap, at no point in its cycle does it revisit the trap centre. Consequently, the work done on the bead is never equal to zero, as the bead’s stored energy is never fully released. This is different to the horizontal actuator trajectory, where the probe travels through the centre of the trap, and revisits the trap centre twice during one cycle. At the moment this occurs, the work done on the probe bead equals zero.

It would be interesting to see if this was indeed the case experimentally, as more research on this energy transfer could lead to a better understanding of micro-swimmers and water living micro-organisms. It could also aid the growing field of micro-robotics.

4.5 Conclusions

We have investigated ‘Lissajous-like’ trajectories of optically trapped particles as they experience time-varying oscillating hydrodynamic forces. In particular, we have demonstrated the breaking of time-reversal symmetry in the motion of an optically trapped particle when it is subjected to a time-reversible symmetric external force-field. This has produced visco-elastic competition, where viscous forces (hydrodynamic flow) competes with elastic forces (optical restoring force).

We have shown how even a very simple system of two microspheres, driven without feedback, can display a wealth of complex behaviour, and have shown that the simple addition of a static trap within HOT can produce visco-elastic forces. These forces are able to break time-reversal symmetry, even when the driving force is not time-reversal symmetric. This time-reversal symmetry breaking is a consequence of the action of both a time-dependent hydrodynamic flow and a position-dependent optical restoring force from the probe trap as the probe moves. Throughout this probe motion, the trapped probe never reaches a static equilibrium position.

Future work could also involve tracking microorganisms in this visco-elastic force using a similar setup to that in the research chapter but also using the knowledge gained from chapters 2 and 3. We see that time-varying hydrodynamic forces, like those produced in the experiment, are fairly weak, and possibly too weak to ‘trap’ a particle, although it would be useful to investigate further to see if there was an appropriate configuration of actuator beads to hydrodynamically trap a particle, which could significantly aid rotating micro-tool research [83, 84]. This could be useful for biological experiments, as hydrodynamic forces are unaggressive and less harmful than optical forces (produced by lasers) on biological and living samples such as cells or bacteria.

It would also be interesting to repeat the experiment especially to attempt to measure the energy transfer between the the probe and actuator beads. The simulation was mentioned previously in the chapter. By finding out whether this is in agreement with experimental data, we have more evidence and thus a deeper understanding of micro-swimmers and water living micro-organisms. This information could also further aid the growing field of micro-robotics.

Chapter 5

Four directional stereo-microscopy for 3D particle tracking with real-time error evaluation

This chapter is based on the work discussed in the Hay et al. Optics Express paper "Four-directional stereo-microscopy for 3D particle tracking with real-time error evaluation" [49].

There are many advantages to putting an SLM in the trapping arm of an Optical Tweezer setup (making the setup a HOT system). The SLM can be used to produce multiple traps, as well as providing interactive control of the trap positions in x, y and z directions.

There are also advantages to putting an SLM in a camera arm of the microscope, allowing complex imaging modes to be used with only minimal additional hardware [85, 86]. In this chapter we look at the advantages of using an SLM in this way for stereo-microscopy, a type of microscopy that allows the user to gain three dimensional information about a sample. The SLM from the trapping arm of our optical tweezer

setup was replaced with a mirror, and the SLM was moved to the imaging arm, similar to that in Lee et al. 2014 Optics Express paper [87].

Using multiple illuminations (in this case four) of the sample, and with the help of parallax calculations, we were not only able to position track an optically trapped bead in the x, y and z directions, but were also able to measure the accuracy of the tracking with real-time data. The ability to track in real-time is very important for many types of experiments, and has been done laterally in areas such as microreology and microbiology [51, 52, 88–91], including Dienerowitz et al. biofilms research, which I was involved in [1]. This is a process, that we have called ‘Quad-Stereo-microscopy’, allowing one not only to track laterally and axially, but to measure the accuracy of the tracking data, all in real-time.

5.1 Introduction

Previously, 3D tracking was done using Quadrant Photo-Diodes (QPDs), which were positioned on the back focal plane of the microscope’s condenser to detect the photons that were reflected off the sample [39, 92]. By finding the intensity difference between quadrants to find lateral position information and summing the intensities reaching each quadrant to yield axial position information, it is possible to gain 3D position data.

There were also interferometric techniques used to produce 3D data, which again uses QPD technology to detect the position of the sample particle [93, 94]. In this process, two light beams are used to create an interference pattern. Here, the phase difference, and hence interference pattern produced by the interferometer setup when a particle is tracked, yields both lateral and axial position information about the tracked particle, so thus 3D data can be produced.

One alternative to this QPD method is using digital holography for holographic 3D particle tracking. Here, a hologram (an interference pattern) is produced at the image plane as the object beam and the reference beam interfere. From this interference pattern, which can be viewed using a camera, one is able to retrieve position information, as there is both amplitude and phase information that can be deduced from the recorded wavefront [95, 96]. Digital holography can be combined with the interferometric technique discussed previously, by placing the hologram in the sample plane [97, 98].

Unfortunately, when using QPDs, one is unable to view the sample live, and therefore it is much harder to detect and stop issues happening within the sample, such as excess beads falling into tracked traps. QPDs are also not trivial to calibrate, nor are they trivial to extend to track multiple particles, compared to video tracking.

Other 3D tracking methods not involving QPDs can include contrast inversion [99] and finding the point spread function of the tracked particle [46, 100].

More recent methods have included combining holograms with microscopy to gain 3D particle tracking is the work of Saglimbeni et al. [101]. In this work, it is shown that with 3 tilted colour illumination channels, one is able to gain lateral and axial tracking data, due to the overlap of the three numerical reconstructions obtained by the tilted light channels. This stereo-scopic technique demonstrates an improvement in the axial resolution of holographic images.

Much research has gone into the technique of stereo-microscopy. A stereo-microscope enables three dimensional visualisation of a sample by providing two views of it from different directions [102, 103]. If an object moves axially in a sample which is viewed at an angle, there is an observed lateral movement in the corresponding image. This is by an amount and direction that is dependent upon the viewing angle. The 3D axial

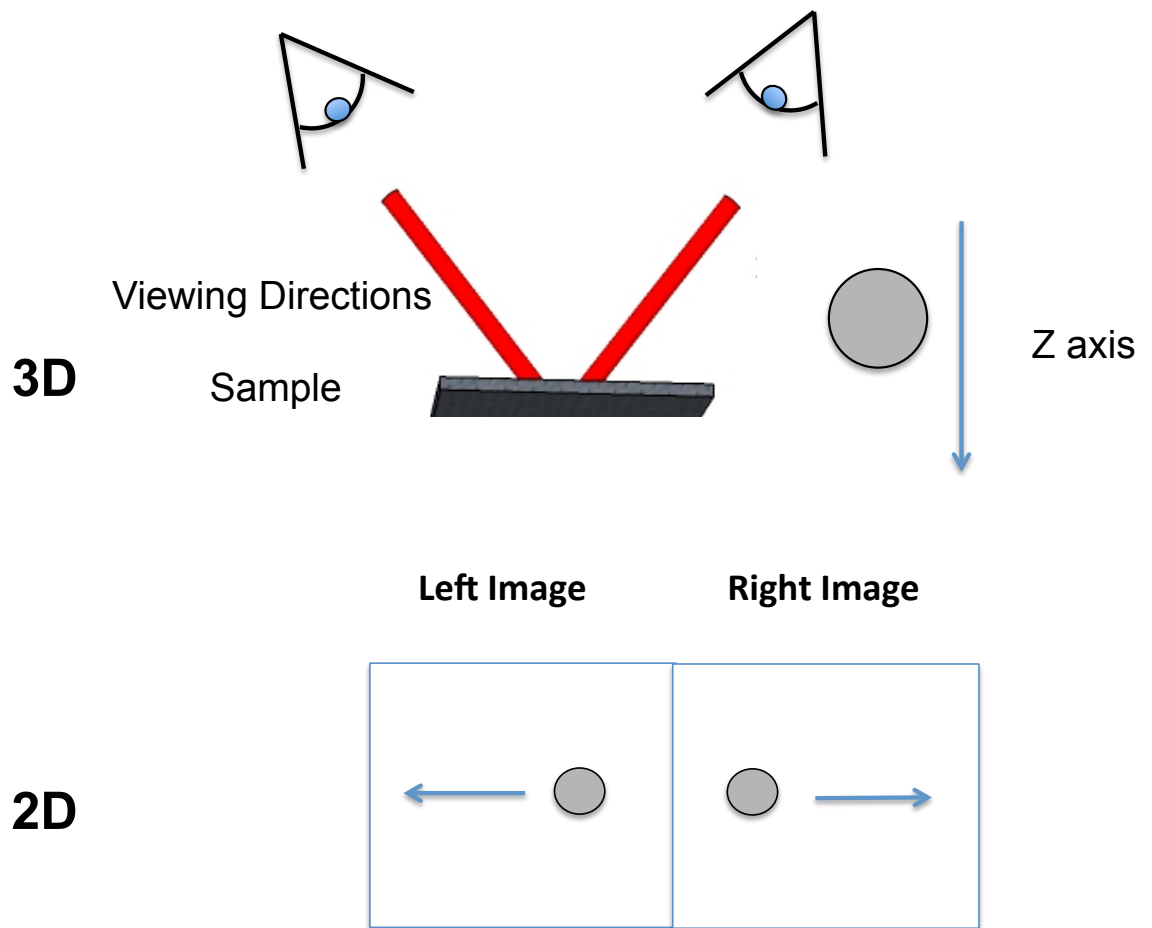


FIGURE 5.1: By illuminating the sample from different directions, multiple images are produced, each individual image corresponding to one illumination direction. When an object moves up and down in the z direction of the sample, the sample appears to move in the x and y direction in the corresponding 2D images.

(z) movement of a bead and its corresponding lateral (x, y) movement is illustrated in figure 5.1.

Stereo-microscopy is different to these other methods, as it does not require a hologram in its simplest form, and can be combined with high-speed video tracking [103, 104]. Simple, computationally efficient centroid tracking can be used on 2D images in order to obtain 3D position information.

Stereo-microscopy can be done in one of two ways (as seen in figure 5.2). One is to carefully align two objective lenses at angles with respect to the sample, and have

a single light source illuminating the sample [102, 105, 106]. This process can be expensive due to having to use two objective lenses and requires two cameras to view the separate images. In addition, this method limits the choice of objective lens that can be used, both in terms of magnification and Numerical Aperture (NA).

The cheaper and more simpler setup would be to have two light sources, illuminating the sample at different angles, followed by one objective lens, located in the conventional position, perpendicular to the sample. By illuminating from two distinct directions simultaneously, two simultaneous views of the sample from different angles can be imaged using a single objective lens [107]. This requires just one camera, making the setup more cost effective, and simpler to calibrate and align.

Not only does this approach have parallels with human vision, where each eye has its own lens, but it is related to research I was involved in which is discussed in the Zhang et al. publication, ‘A fast 3D reconstruction system with a low-cost camera accessory’ [108]. Here, multiple illumination sources are used to produce 3D information from a commercially available digital SLR camera. In this example, macroscopic objects are used rather than microscopic. To gain the 3D information a process called photometric-stereo is used, where the amount of change of illumination (and thus shadow) between the different illumination images in each corresponding pixel is used to produce a 3D map of the object.

One drawback to using this method is the superposition of the images produced from each illumination angle. Previous ways of tackling this include separation by channel colour [109], and redirection of the different images by placing bi-prisms in the Fourier plane of the imaging arm of the system [103]. This method can be tricky to align, which leads to it commonly being used with only two illumination angles.

Another way to separate superimposed images is to place an SLM in the Fourier plane rather than bi-prisms [85, 110]. The SLM separates the images by diffracting

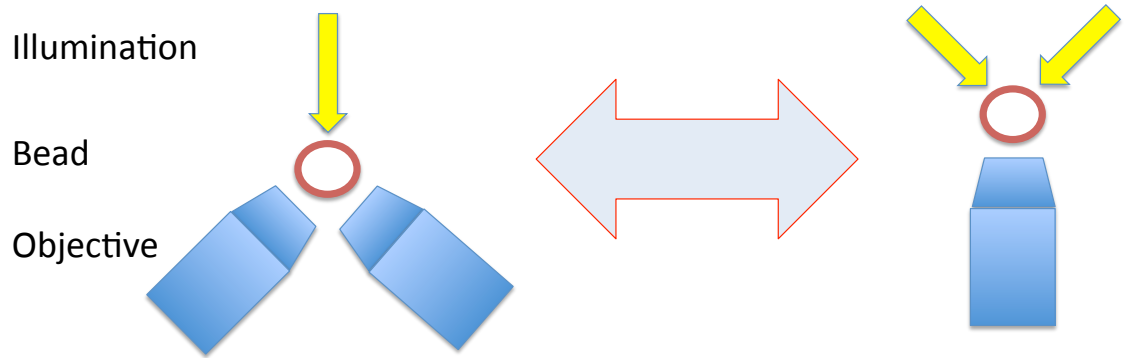


FIGURE 5.2: Stereo-microscopy is a technique that enables a sample to be imaged from two directions simultaneously, allowing the tracking of microscopic objects in three dimensions. This can be done by either one illumination and two objective lenses or two illuminations and one objective lens. By illuminating the sample from different directions, multiple images are produced, each individual image corresponding to one illumination direction.

the light from each illumination direction to a different position on the camera, as the bi-prisms do. Placing and aligning an SLM in the system is much easier than aligning bi-prisms, and thus saves time when setting up. It also allows one to incorporate the technique with other imaging techniques such as dark-field imaging [86], and allows dynamic refocussing so that particles can be tracked over an increased depth of field [87]. The flexibility of an SLM also enables multiple illuminations to be viewed simultaneously (rather than just two), provided the images can be viewed by the camera. This allows us to measure the accuracy of the tracking system, by comparing independent measurements, each using a different pair of illumination angles. It is also an advantage to have more than two illumination angles in case there is an obstruction in the way of one of the illumination sources. If that does occur, it is simple enough to swap to another illumination source that is not obstructed, thus allowing axial measurements to be calculated.

This process can be a useful tool when combined with high-speed video tracking, a

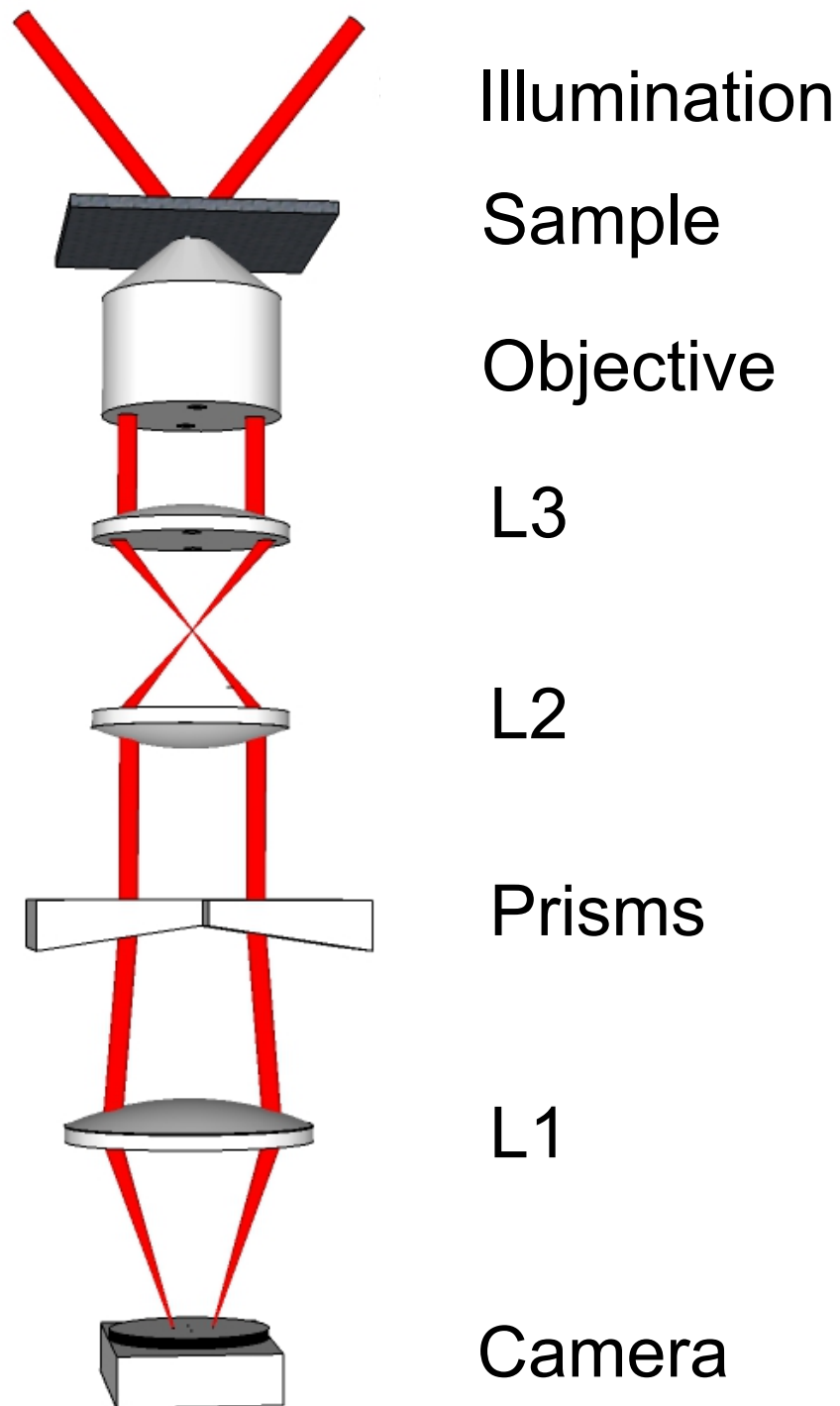


FIGURE 5.3: Layout of previous Stereomicroscopy system including wedge prisms to separate the superimposed images and to send them in different directions. This works best for two illumination directions, so is convenient to use an SLM so that we can use more illuminators.

process that we call high-speed video stereo-microscopy. High-speed video stereo-microscopy has been used in a variety of situations thus far, including the axial position clamping of optically trapped objects [104, 111], the observation of optically stacked particles [112], tracking of live algae and artificial non-spherical structures [111, 113], and in an optically controlled scanning probe microscope [74].

In this chapter we demonstrate a stereo-microscope with four illumination directions rather than the usual two. We therefore provide two independent measurements of the 3D position of an optically trapped micro-bead and find the Root Mean Square (RMS) of the difference to measure the accuracy of the tracking data. The comparison of these measurements yield our estimate of the accuracy of both lateral and axial tracking of the microbead in real-time while undergoing Brownian motion, rather than a single lateral accuracy [104]. This is different to finding the precision or repeatability of the technique (such as looking at the noise on a static object) [86]. This method of measuring the accuracy of the system is representative of the situation in which the technique is most often used. We investigate how tracking errors depend on the exposure time and the degree of spatial filtering of each image. From examining these two conditions, we are able to optimise the system.

5.2 Methods

5.2.1 Experimental set-up

Figure 5.5 shows a schematic of the experimental set-up. It is based on a transmission light microscope with an SLM placed in the Fourier plane in the image arm of the set-up. The sample is illuminated from four directions with red LEDs (Luxeon Rebel, peak emission at 636 nm). The LEDs are coupled into light guides to transmit the

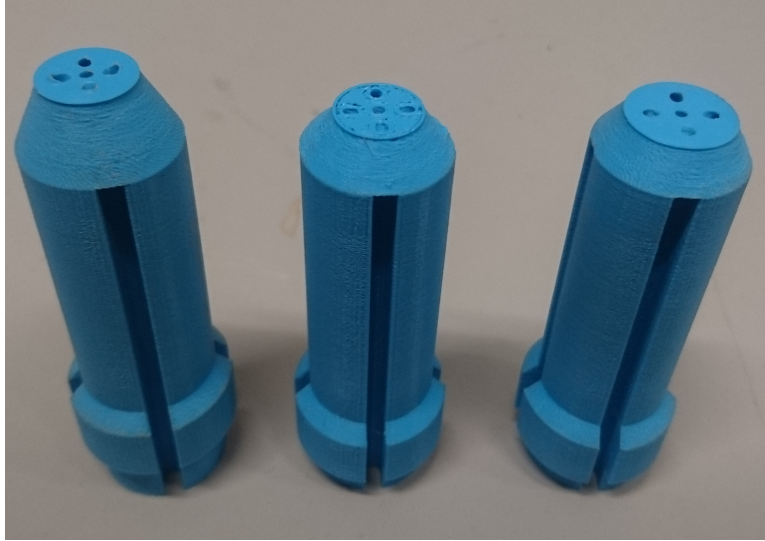
illumination. Light transmitted through the sample is collected by the objective lens (Zeiss Plan-Neofluar, $100\times, 1.3\text{ NA}$). The polarising beamsplitter selects light of the correct polarisation for the SLM. An iris in a conjugate image plane controls the field-of-view to ensure all images fit adjacently onto the camera. A narrowband filter ($635\text{ nm} / 10\text{ nm}$) minimises dispersion of the images when diffracted from the SLM. The polarising beamsplitter is also used to couple in a single beam optical tweezer ($\lambda = 635\text{ nm}$). The focal lengths of the lenses are: $L1 = 120\text{ mm}$, $L2 = 150\text{ mm}$ and $L3 = 200\text{ mm}$.

We use a compact design for stability, based on the microscope described by Lee et al. [87], with a modified illuminator head which holds four optical fibre light guides each illuminating the sample from a different direction.

The compact illuminator head we required was not commercially available, having four light guides where the illumination angle could be controlled. It was decided that the illuminator head would be designed using a Computer Aided Design (CAD) program called Sketchup, and printed using a 3D printer (Ultimaker 2.0). The plastic material used to make one illuminator head cost about 20p, hence this option ended up being very cost effective, especially as a set of these were printed covering a range of illumination angles. As the main design did not change significantly between illuminator heads, and each only taking approximately three hours to print, it was also quick, as we did not have to rely on outsourcing the manufacturing to contractors.

We use an SLM to diffract each of the four views of the sample to a different location on the camera. The optical layout is shown in Fig. 5.5, and the four illumination paths through the system are shown in Fig. 5.6(a). Each illumination direction corresponds to a unique position in the Fourier plane of the sample where the SLM is positioned. The pattern displayed on the SLM is shown in Fig. 5.6(b), it consists of four apertures, each centred on a position corresponding to one of the illumination

(a)



(b)



FIGURE 5.4: (a) Examples of the illuminator heads designed with Sketchup and 3D printed using the Ultimaker 2.0 3D printer. Note that the three heads cover a range of angles. (b) Example of one illuminator head holding the four optical fibres used as light guides.

directions. Within each aperture, a phase grating diffracts the light to a separate region on the camera chip, resulting in an image such as that shown in Fig. 5.6(c).

5.2.2 Using parallax calculations to find 3D position coordinates

The position of a bead in each image is tracked in two dimensions using a centre of symmetry algorithm [103]. The apparent position in 2D is a projection of its 3D position onto the focal plane from the direction defined by the illumination angle. Each illumination is at a direction defined by azimuthal and polar angles (ϕ and θ respectively). If we were to look at figure 5.7, a bead at position a will result in

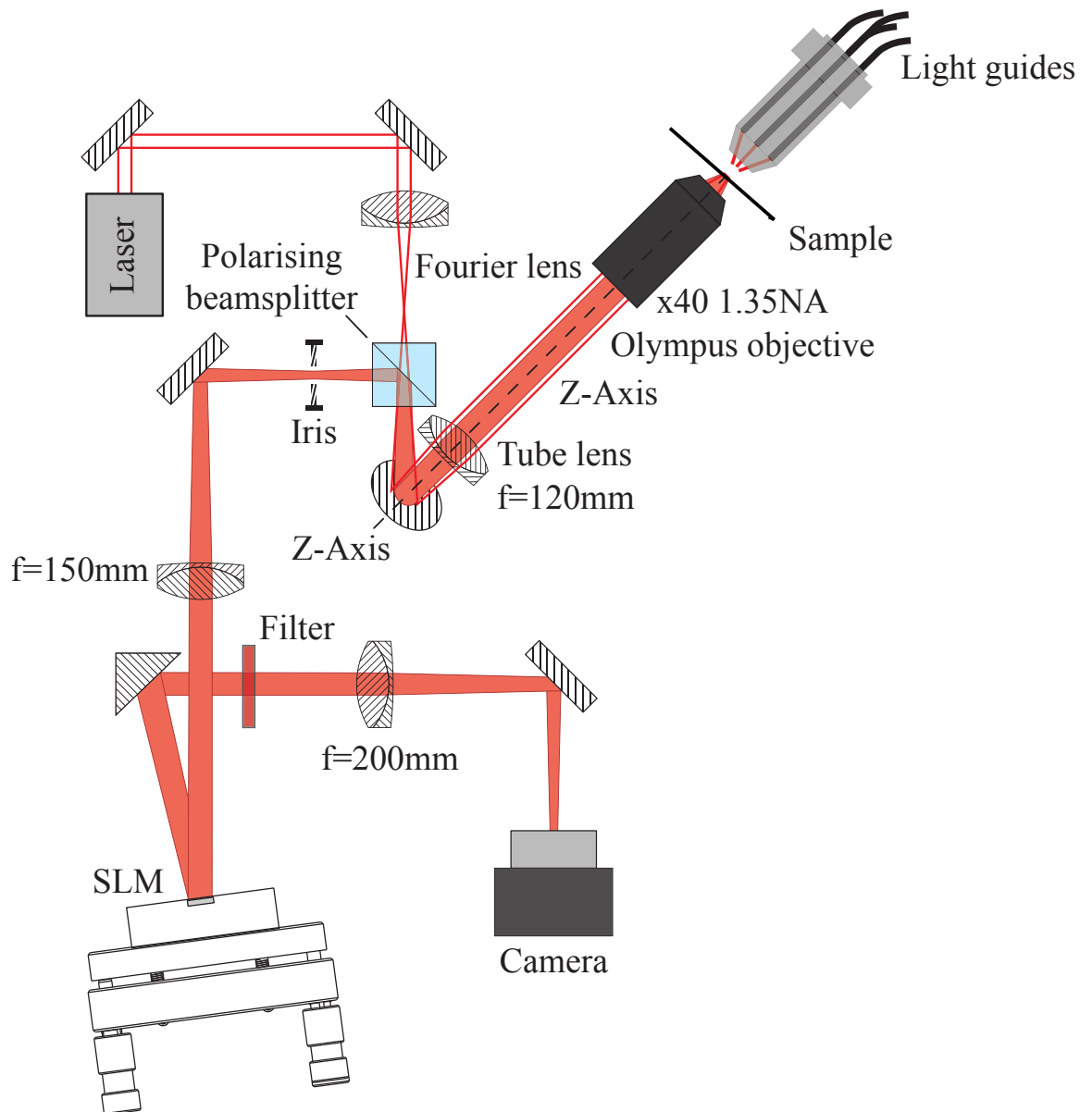


FIGURE 5.5: Schematic of the optical layout. It is based on a transmission light microscope with an SLM placed in the Fourier plane of the image. The sample is illuminated from four directions with red LEDs (Luxeon Rebel, peak emission at 636 nm) coupled into light guides. Light transmitted through the sample is collected by the objective lens (Zeiss Plan-Neofluar, 100 \times , 1.3 NA). The polarising beamsplitter selects light of the correct polarisation for the SLM. An iris in a conjugate image plane controls the field-of-view to ensure all images fit adjacently onto the camera. A narrowband filter (635 nm / 10 nm) minimises dispersion of the images when diffracted from the SLM. The polarising beamsplitter is also used to couple in a single beam optical tweezer ($\lambda = 635$ nm). The focal lengths of the lenses are: L1 = 120 mm, L2 = 150 mm and L3 = 200 mm.

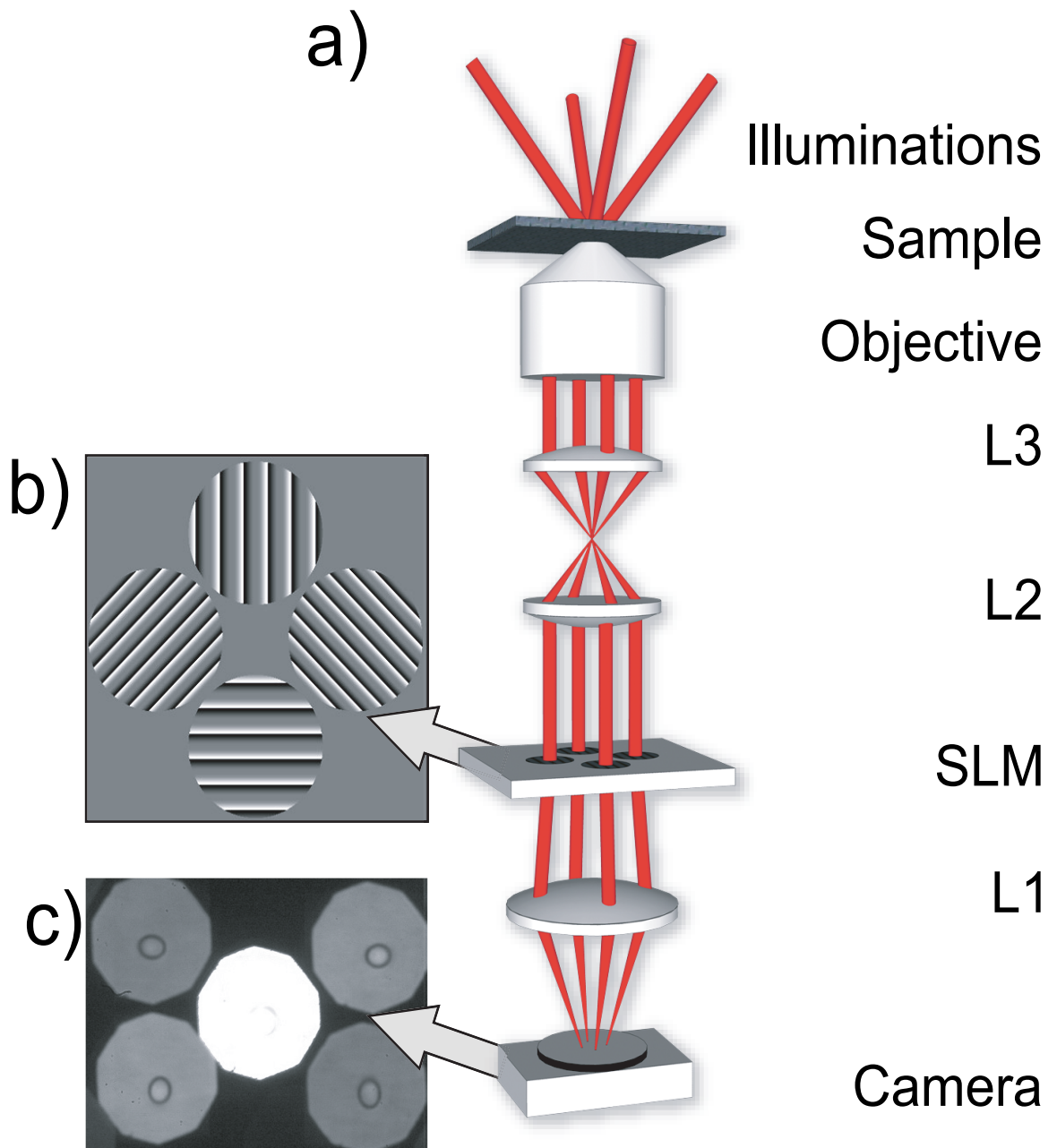


FIGURE 5.6: a) Illustration of the four illumination paths through the system. Here the SLM is shown as a transmissive element rather than reflective, for clarity. The SLM diffracts light corresponding to each illumination direction to a separate region of the camera sensor. (b) A representative phase pattern on the SLM. (c) The resulting image on the camera. Undiffracted zero-order light is sent to the central region. The scaling is 73.5 nm per pixel.

a projected image at a_i in the focal plane. If the bead moves vertically to b , the projected image moves to b_i in the focal plane. The direction of the translation of the projected image is defined by θ , and the magnitude is a function of δz and ϕ . For an arbitrary 3D translation of the bead, the vector to describe it is $v = [\delta x, \delta y, \delta z]$.

Looking at figure 5.7, it is clear to see that if the bead moves in the z direction in 3D, there will always be some movement in x and y in the 2D projection. This overall move in 2D is:

$$x_m = x_x + x_z \quad (5.1)$$

$$y_m = y_y + y_z \quad (5.2)$$

This corresponds to the movement in the x or y direction itself plus the apparent x or y component in 2D from the bead's 3D movement in z . The apparent x and y movement in 2D due to 3D z movement is equal to $\delta z \tan \phi \cos \theta$ and $\delta z \tan \phi \sin \theta$ respectively. Therefore, equation 5.1 is equal to

$$x_m = \delta x + \delta z \tan \phi \cos \theta \quad (5.3)$$

Equation 5.2 is equal to

$$y_m = \delta y + \delta z \tan \phi \sin \theta \quad (5.4)$$

The distances moved in each direction cannot be calculated by one illuminator, as there are more unknowns than equations. Therefore, we must use pairs of illuminators (i and j), and use either the x or y data. If a bead moves x or y in 3D, in the 2D projection the bead will move x_{m_i} and y_{m_i} if viewing with illuminator i, and x_{m_j} in x and y_{m_j} if viewing with illuminator j. These values are equal to:

$$x_{m_i} = \delta x + \delta z \tan \phi_i \cos \theta_i \quad (5.5)$$

$$x_{m_j} = \delta x + \delta z \tan \phi_j \cos \theta_j \quad (5.6)$$

$$y_{m_i} = \delta y + \delta z \tan \phi_i \sin \theta_i \quad (5.7)$$

$$y_{m_j} = \delta y + \delta z \tan \phi_j \sin \theta_j \quad (5.8)$$

By either setting equations 5.5 and 5.6 or equations 5.7 and 5.8 as a set of simultaneous equations, we can rearrange and solve for δz , with equations 5.9 and 5.10 for x and y data respectively. δz will be the same value for both equations 5.9 and 5.10.

$$\delta z_x = \frac{x_{m_j} - x_{m_i}}{\tan \phi_j \cos \theta_j - \tan \phi_i \cos \theta_i} \quad (5.9)$$

$$\delta z_y = \frac{y_{m_j} - y_{m_i}}{\tan \phi_j \sin \theta_j - \tan \phi_i \sin \theta_i} \quad (5.10)$$

The value of δz can then be substituted back into equations 5.5, 5.6, 5.7 and 5.8 to find δx and δy , using equations 5.11 and 5.12.

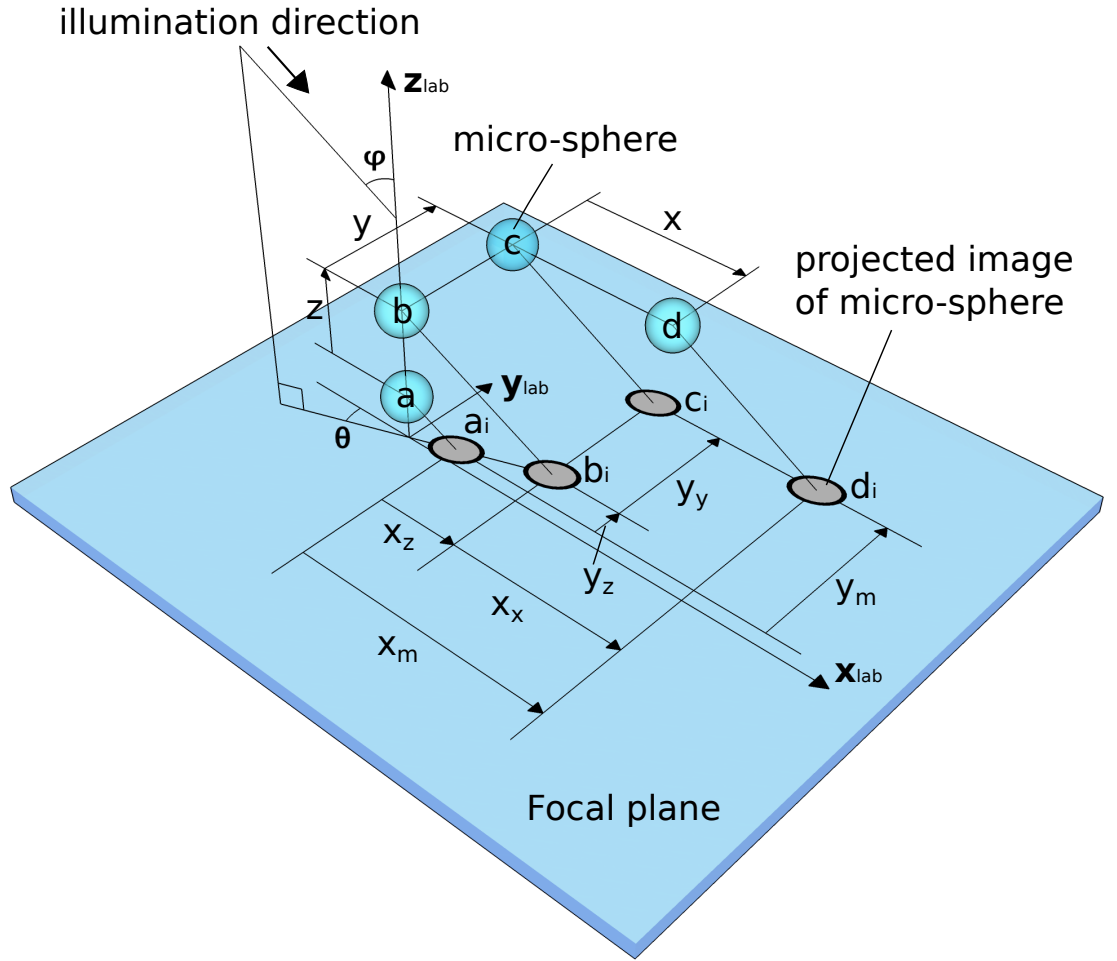


FIGURE 5.7: The relationship between micro-bead's 3D position to its projected image on the focal plane. The measured motion of the image parallel to x in the focal plane is given by $x_m = A + \delta x$, where $A = \delta z \tan \phi \cos \theta$. Likewise the measured motion of the image parallel to y is given by $y_m = B + \delta y$, where $B = \delta z \tan \phi \sin \theta$.

$$\delta x = \frac{x_{m_j} \tan \phi_i \cos \theta_i - x_{m_i} \tan \phi_j \cos \theta_j}{\tan \phi_i \cos \theta_i - \tan \phi_j \cos \theta_j} \quad (5.11)$$

$$\delta y = \frac{y_{m_j} \tan \phi_i \sin \theta_i - y_{m_i} \tan \phi_j \sin \theta_j}{\tan \phi_i \sin \theta_i - \tan \phi_j \sin \theta_j} \quad (5.12)$$

To track accurately using parallax, the angles of the illumination of each channel must be known. This can be achieved by aligning each channel to the aperture at a preset

position in the SLM at the focal plane. The light is centred on the aperture when the image of a microsphere appears at its most symmetrical. When the apertures are lined up to the illumination, the system is aligned. From there, the azimuthal and polar angles of each illumination channel can be calculated from the location of the centre of each aperture on the SLM, without the need for calibration using a Labview program, by monitoring the translation of a micro-sphere fixed to the substrate as it is stepped axially by a known distance.

5.2.3 Data Acquisition

A program was created on Labview to control the SLM. This SLM program switches on the SLM and produces apertures that can be displayed on the SLM monitor, using the ‘Gratings and Lenses’ algorithm to design the apertures [29]. The program allows multiple apertures to be displayed on the SLM at once. In the case of the experiment, four separate apertures are created. Within each aperture, a phase grating diffracts the light to a separate region on the camera chip. Figure 5.6(b) is a figure of the grating displayed on the SLM. We find the four separate illumination first order images from the superimposed zero order image, and align each of them to a separate aperture.

The program also included an override mode, which was originally used in Lee et al. paper ‘Dynamic stereo microscopy for studying particle sedimentation’ [87]. This allows the SLM to continually update the gratings, depending on the position of the bead. This was achieved by using the calculated z position to design the Fresnel lens. This allowed the bead to always stay in focus, and thus easier to track over a longer range. This included adding a lens hologram to each grating on the SLM, to refocus the bead. We investigate whether keeping the bead in focus is a help or a hindrance when 3D tracking a bead.

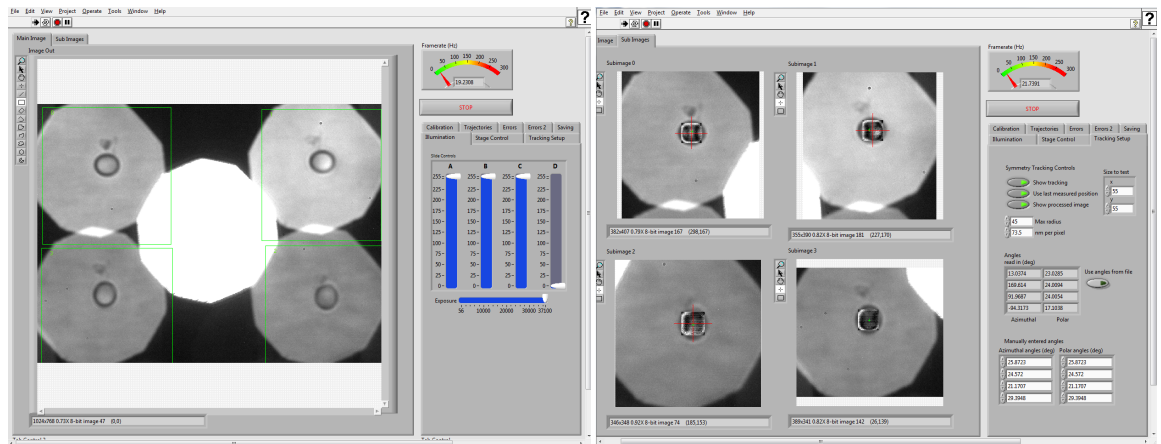


FIGURE 5.8: Images of the front panel of the Labview program. The left shows the illumination intensity control and the full image viewed by the CMOS camera. The right shows the four separated first order images (indicated by the green square in the left image) and the tracking setup controls. These controls include the illuminators' azimuthal and polar angles, tracking area test size, and a tracking off and on switch.

When the SLM display or the setup is changed and the image is ready for data taking, a calibration must be performed on a stuck bead in the sample, to calculate the polar and azimuthal angles of the illuminators. The calibration performed is fairly simple compared to other 3D tracking calibration procedures (such as QPD calibration), as the stuck bead is moved electronically through z , with an image taken from each stage. We calculate the change in x and y displacement in each image, and because the position in z is already known for each image, we are able to rearrange parallax equations, to calculate the polar and azimuthal angles required.

These angles are then fed into the camera acquisition program. At this point, tracking of a bead is performed using a radial symmetry tracking method [103]. In the program, the four first order images are separated, and the tracking positions of the bead in x , y and z are measured, as well as their standard errors, corresponding to four pairs of illuminations, (two sets of opposite pairs, and two sets of adjacent pairs). This was done over a set time, where around 500 images are recorded.

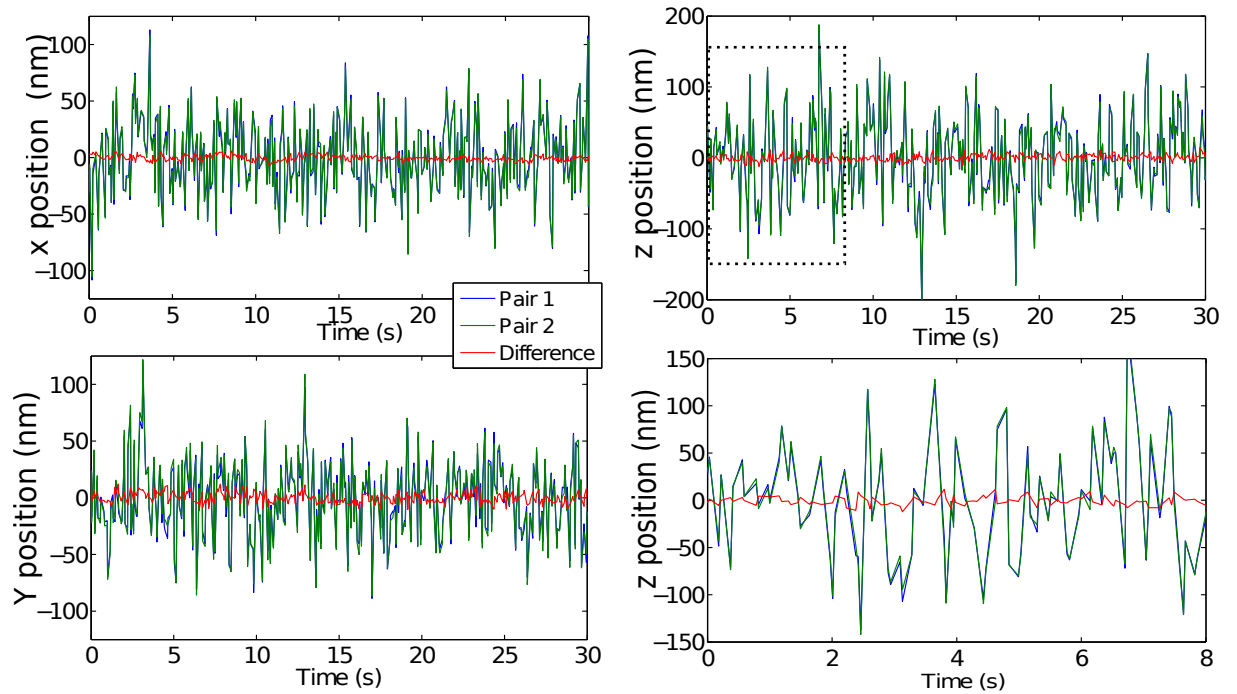


FIGURE 5.9: Accuracy of 3D particle tracking using stereo-microscopy. Top left, top right and bottom left show traces of the measured x , y and z positions respectively. In each case the two independent measurements (green and blue lines) are overlaid by subtracting their mean positions. The red trace indicates the difference between the measurements. Bottom right shows a zoom in on the highlighted region of the bottom left to more clearly observe the similarity of the measurements.

5.3 Results

Figure 5.9 shows a comparison of the two independent measurements of the trajectory of an optically trapped micro-bead recorded using our four directional stereo-microscope. The difference between each measurement is shown by the red trace. In this case the azimuthal illumination angles were separated by $\sim 90^\circ$, and the polar angles were all $\sim 25^\circ$.

We have demonstrated an accuracy of better than 7% of the range of motion of a $2\ \mu\text{m}$ diameter optically trapped micro-bead (as seen in figure 5.9).

The RMS of the differences between each measurement in the case of figure 5.9 are 2.6 nm in x , 4.5 nm in y and 5.1 nm in z , using data recorded over a 30 s period with

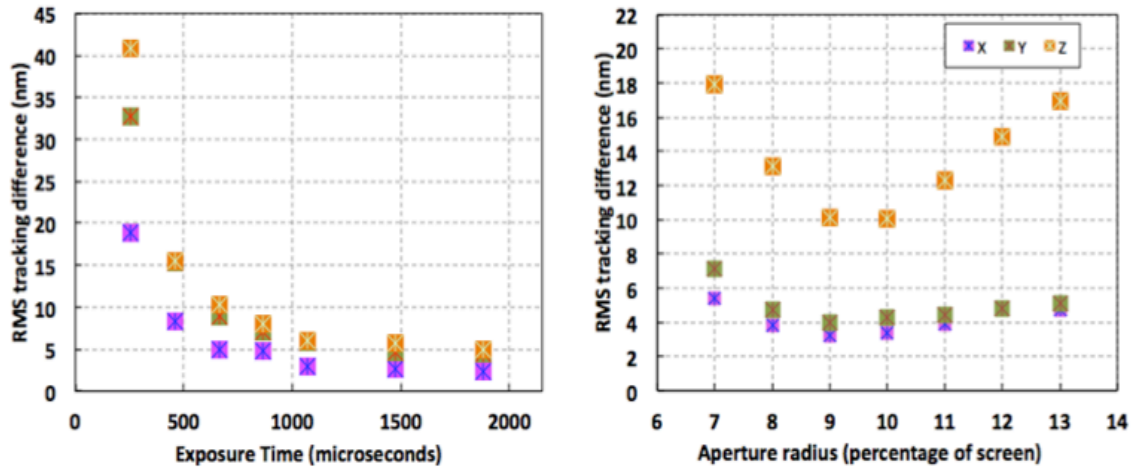


FIGURE 5.10: Accuracy of 3D particle tracking using stereo-microscopy in each dimension with respects to (a) the level of spatial filtering (aperture size in terms of a percentage of the SLM screen space) and (b) the exposure time of the camera (measured in microseconds).

an exposure time of $1877 \mu\text{s}$ (corresponding to a frame rate of 532 Hz if not limited by other factors). Figure 5.9(d) shows a zoom in on part of the axial position trace to more clearly reveal the similarity of the measurements.

5.4 Discussion

In figures 5.12 we can see that the off-axis illumination introduces distortions in the images of a micro-bead. due to the image and the illuminating light not being perpendicular to each other. Some of the high spatial frequency distortion caused by this can be removed by changing the aperture size on the SLM (hence add some low-pass spatial filtering to the image).

If the apertures are too large, then the spatial filtering is set too high. Not only would the amount of light reaching the image plane saturate the camera chip, but the distortions due to off axis illumination would cause the bead to appear more asymmetric as it moves axially, making it more difficult to track, and increasing the tracking difference. This is shown in figure 5.13.

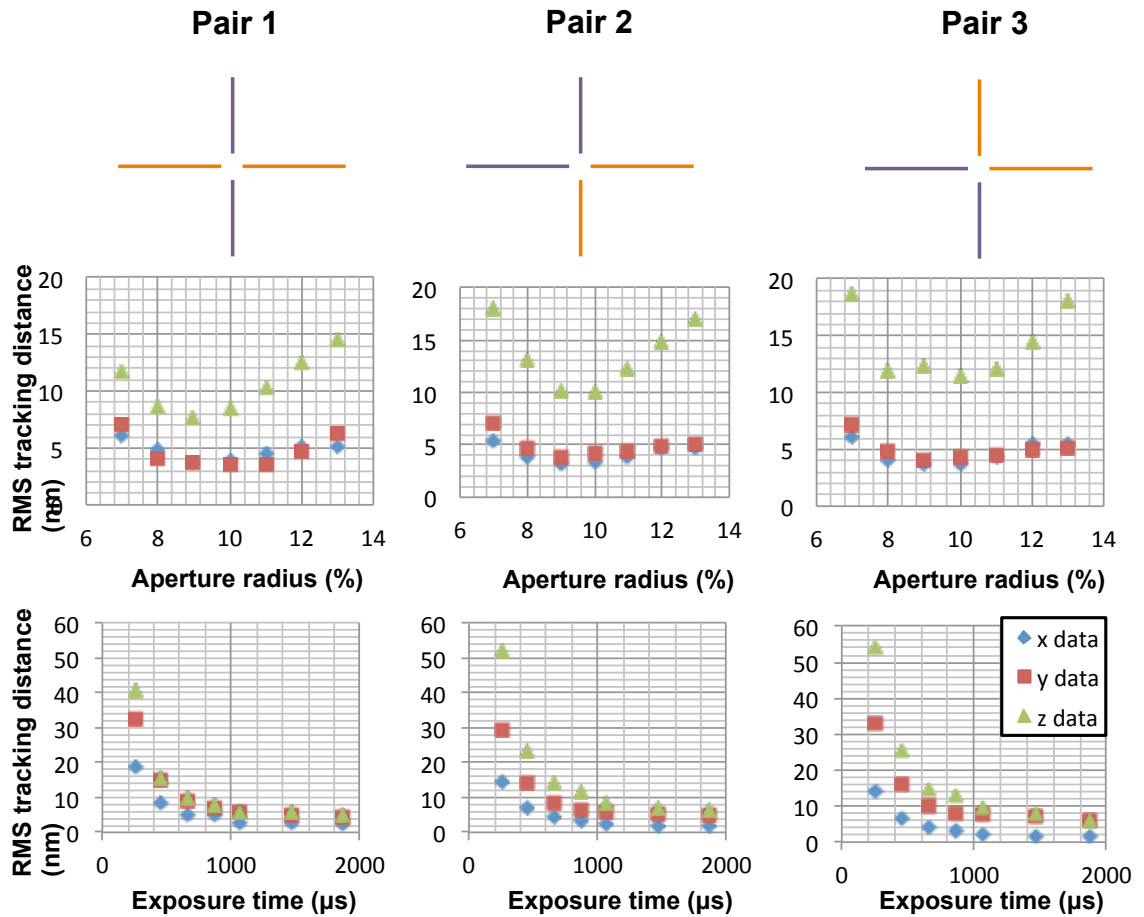


FIGURE 5.11: Accuracy of 3D particle tracking using stereo-microscopy in each dimension depending on each pair of illuminators with respects to the level of spatial filtering (aperture size in terms of a percentage of the SLM screen space) and the exposure time of the camera (measured in microseconds). The top illustration describes each set of illuminator pairs. The pair of opposite illuminators appear to give the more accurate results than each set of orthogonal pairs.

Conversely, when the apertures are too small and the spatial filtering is low, not enough light is able to reach the imaging plane, making it harder to track the bead. This causes a decrease in the signal to noise ratio, which leads to an increase in tracking difference.

The results of how the aperture size affects the bead image are shown in figure 5.12. A balance between these effects results in an RMS tracking difference between illuminator pairs (see figure 5.10(b)). This aperture size is between 10 and 11 pixels wide, corresponding to a radius of approximately 1.4mm.

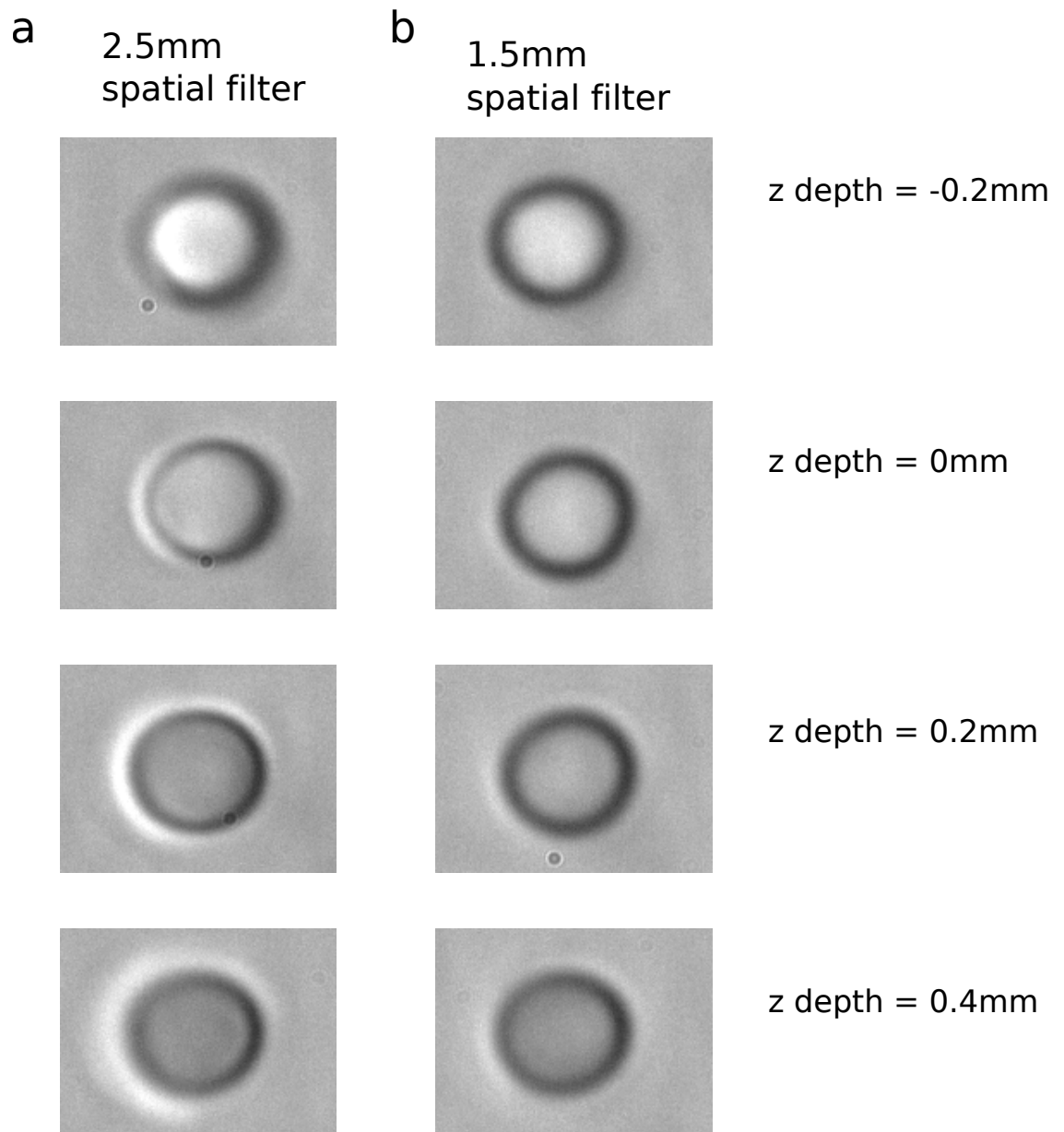


FIGURE 5.12: (a) shows a column of four images of a micro-bead at different heights with a spatial filter diameter of 2.5mm. (b) shows the same micro-bead with a reduced diameter spatial filter. In (b) the images are now more symmetrical, facilitating accurate tracking.

The reduction in the signal to noise ratio due to low light levels is also evident when the exposure time of the camera was varied. These results are shown in figure 5.10. We found that at shorter exposure times there was an increase in the RMS tracking difference between illuminator pairs. In our set-up the light level was limited by the diffraction efficiency of the SLM, so a 10 nm bandpass filter was used to reduce dispersion of light diffracted from the SLM. At exposure times less than $300\mu\text{s}$, we have RMS tracking differences of over 20nm in all dimensions. Despite this, we find that this RMS tracking difference levels off to around 10 nm in each dimension above exposure times of $663\mu\text{s}$, corresponding to a frame rate of 1508 frames/second. This issue can also be further improved by increasing the illumination intensity [42]. Figures 5.10(a) show a small difference in the minimum error for each dimension.

This is representative of the variation in measurements taken with our system, where the measured accuracy was dependent upon system alignment, and the state of the sample (for example, how perfectly spherical and optically clear the micro-bead of interest was). Throughout our measurements we obtained accuracies of 2-5 nm laterally, and 5-10 nm axially on a $5\mu\text{m}$ diameter optically trapped micro-bead [49].

We also found no strong argument to whether the override system to keep the bead in focus was an advantage to the system, while working within the focussing range (see figure 5.14). This was experimented on by moving the sample stage manually, producing a spike for our RMS graphs. We found that the accuracy of the tracking measurements is greater with the override mode switched off. This may be due to the SLM updating at a lower speed than the camera frame rate. Therefore, by the time the SLM has updated, the bead position has changed again, and this new position correspond to a new grating, meaning the SLM must be updated again. This would mean the override is reacting too slowly for the system. However, this is something that more research would have to go into, to help us understand this better. A fairer

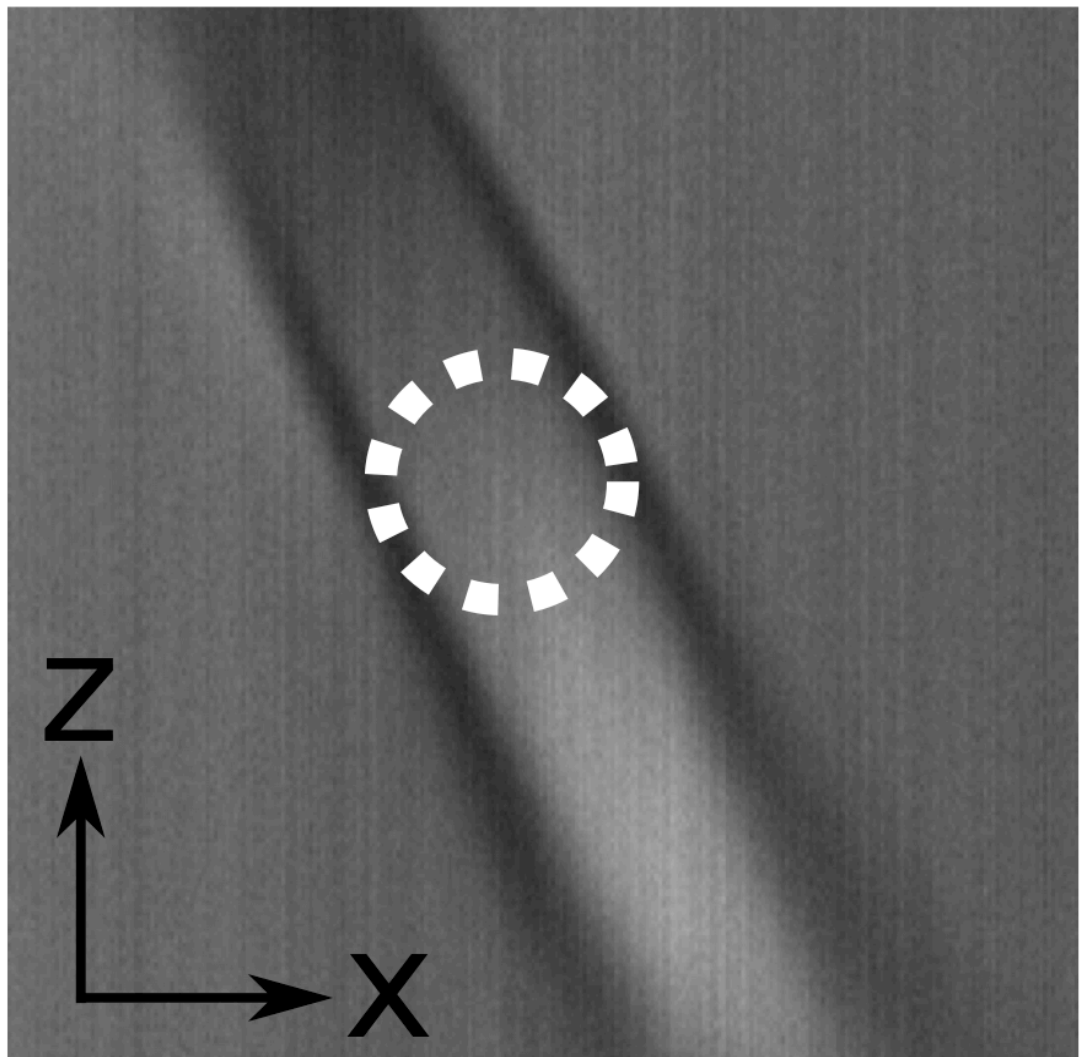


FIGURE 5.13: A vertical cross-section through a z -stack of images (200 images recorded at 100 nm height separations) of a $2\ \mu\text{m}$ diameter micro-bead illuminated by a single off axis illuminator. The approximate position of the micro-bead is marked with a dashed white circle. Optimum tracking is achieved by choosing the most symmetrical horizontal plane for centre of symmetry tracking.

way to evaluate the effects of the override is to make controlled movements of the stage rather than rely on manual movements, making all movements equal in size. It would also be helpful to vary the speed and the distance over which the stage is moved, to see how much this can effect the SLM update.

So we find that for the most accurate 3D tracking results we want an aperture size on the SLM of 10-11 pixels, corresponding to a radius of 1.4mm, and the camera working at an exposure time of over $600\mu\text{s}$.

We find that this method has advantages over other methods, such as interferometric techniques, and the use of QPDs. The stereo-microscopy system is easy to set up and has a simple calibration procedure, and although time was taken to adjust the position of the illuminations, after the first run of the experiment, it did not require further adjustment. Also, our stereo-microscopy allows the user to view live tracking of the sample, with the use of a CMOS camera. Unfortunately QPDs do not allow such luxuries, and so live video-tracking would not be possible for the other two methods mentioned. Although we use silica beads in our experiment, the sample does not necessarily need to be spherical nor symmetrical, unlike 3D tracking using QPDs. We are also able to track multiple particles at once, unlike when tracking not only with 3D but in 2D with QPDs.

Therefore, even though QPD methods may give similar results even at faster frame rates (10skHz rather than $\sim 2000\text{KHz}$ from the high-speed video tracking), there are reasons to suggest that the method explained in this chapter is a method that should be greatly considered when doing a tracking experiment.

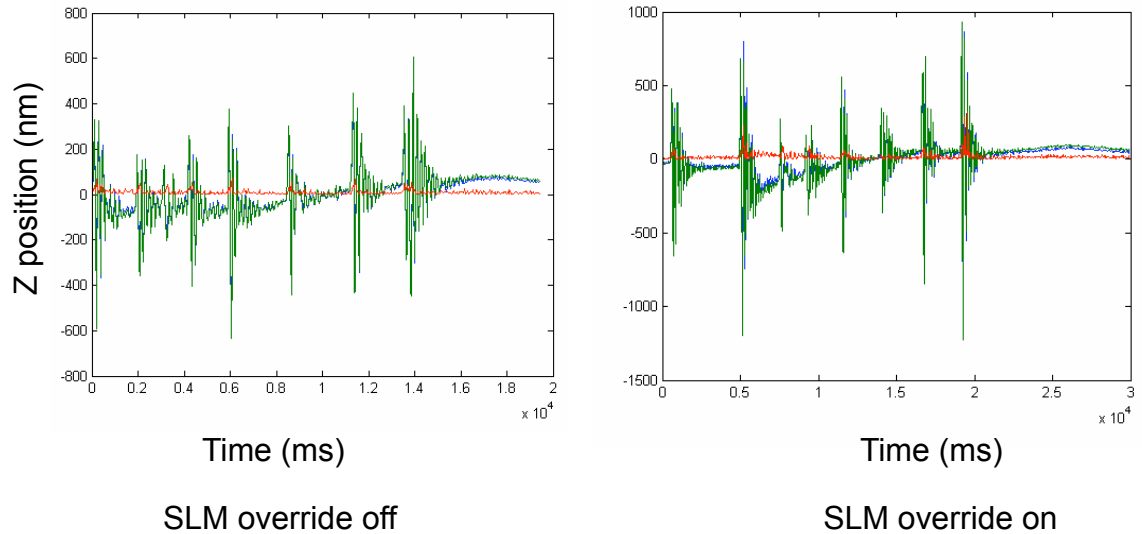


FIGURE 5.14: Graphs showing the trajectory paths of the tracked $2\mu\text{m}$ polystyrene bead in z , with the illuminators at approximately 30 degrees. Here, we have manually moved the stage axially over a large distance in a short period. The left graph corresponds to when the SLM override is switched off, and so the apertures are not changing with respect to the bead position. The right graph has the SLM override switched on, where the SLM is continually updating its apertures to allow the bead to always stay in focus. As with figure 5.10, each case the two independent measurements (green and blue lines) are overlaid. The red trace indicates the difference between the measurements. We see a bigger difference between measurements when the override is switched on.

5.5 Conclusion

In this work, we have shown how an SLM microscope can be used to provide a real-time evaluation of the 3D particle tracking accuracy in high-speed video stereo-microscopy. We have demonstrated an accuracy of better than 2.5% of the range of motion of a $2\mu\text{m}$ diameter optically trapped micro-bead, and shown how the error depends upon the degree of spatial filtering, and camera exposure time, allowing us to optimise the system. The illuminators on our system were set to be at a polar angle of $\sim 25^\circ$, and azimuthal angles of 90° . For the most optimum stereoscope system at this setup, we found that aperture sizes of $10\mu\text{m}$ and camera exposure times of over $600\mu\text{s}$ were favoured.

Knowledge of this error (RMS tracking difference) can also be factored into the trap stiffness calibration of optical tweezers so that we are able calculate more accurate force measurements, something that we talk about in Chapters 1 and 3. This in turn can be used to more accurately recover micro-rheological properties of a sample. As the error signal is generated in real-time, it can also be used to alert an operator during an experiment if anything was to cause problems with the data, for example an unwanted piece of detritus being attracted into an optical trap.

In future we would like to see if we could replace our Quad illuminator with a Digital Micro-mirror Device (DMD). It is a device made up of pixels which are electro-mechanical micro-mirrors. These micro-mirrors are bi-stable, meaning they can be in one of 2 stable states, which are at $\pm 12^\circ$. This means each pixel can either be on or off. They can also switch between states very quickly. Some models can switch at rates of up to 22kHz (much quicker than a liquid crystal SLM).

If we can control which pixels are switched on or off at high rates, we could possibly program our DMD to operate as four separate illuminations, instead of the LEDs. This would provide a means of programatically tuning or aligning the illumination setup. If the illuminations were to switch on and off separately in succession at high rates, the camera would be able to record the image for each illumination direction using just one camera frame. This means that the four images are recorded as a sequence, avoiding the need to separate the overlapping images in the Fourier plane. Such a scheme would rely on careful synchronising of the DMD to the triggering of the camera acquisition but would result in a system which is easier to optimise and which allows the use of the whole camera sensor.

Chapter 6

Conclusions

As stated, Optical Tweezers are a useful tool to manipulate and exert well-defined forces on microscopic particles. Tracking is a very important aspect of measuring these forces acting on the particles. We are always looking at how we can optimise tracking experiments so that we can optimise our force measurement results and apply these measurements to a range of different applications.

In Chapter 1, we reviewed the background on Optical Tweezers. We mentioned the importance of SLMs within the system and how they are used to produce multiple, independently controllable traps. By introducing an SLM in the Fourier plane, the setup becomes a Holographic Optical Tweezer.

‘The Meadowlark Cube’ is a commercial Holographic Optical Tweezer product. The product, designed at the University of Glasgow and Meadowlark Industries in Boulder is one cubed foot in shape, making it compact, stand-alone and portable. Although this is a unique selling point, there are some drawbacks to the design. For example, to save space, different sections of the same lens are used for both for the beam expander and the Fourier lens of the setup, causing the laser light not to travel through the centre of the lenses and off-axis, thus causing aberrations. The aberrations make

it harder to trap objects, as light cannot be as tightly focused and trap stiffness is reduced. With the current ‘Cube’ design, aberrations are corrected using the same SLM that controls trap position, causing a decrease in trap power and stiffness, and an increase in the chance of issues involving cross-talk, limiting the accuracy of the tracking data. Relying on the SLM for aberration correction can also be unhelpful in terms of diagnostic testing.

In chapter 2 we discussed the redesign of ‘The Cube’, to try and reduce the impact of the design drawbacks. We wanted to keep its same qualities (compact, stand-alone and portable), but we also wanted to remove the SLM aberration correction software dependancy, resulting in a system where it is easier to diagnose problems and where potential problems with cross-talk is reduced. Another aspect we wanted to add was the opportunity to use Fluorescence microscopy; a useful tool when using the Cube for biological experiments.

The new ‘Cuboid’ design separates the beam expander / Fourier lens into two individual lenses, allowing laser light to travel on-axis, reducing aberrations. This added $\sim 50\%$ to the width, however the setup no longer relies on an SLM, which can now be replaced by a mirror for diagnostic purposes. This helps to reduce errors and inaccuracies in tracking data. The extra space created also allowed us to replace the fibre coupled laser in the original Cube with a fixed solid-state laser. This provided the advantage of allowing the controller electronics and power supply to be easily detached from the optics for easy transportation of the tweezers.

In the Cuboid, the additional space also allowed us to introduce a cheap and simple fluorescence imaging system into the design, allowing us to image trapped beads in fluorescence, at low frame rates.

In Chapter 3 we extended the simple fluorescence tracking to high-speed fluorescence centroid tracking. The vast majority of video-tracking micro-rheology experiments

is performed using brightfield microscopy, as it is easy to implement, as long as the trapped particle is uniform and spherical. However, brightfield is not always the best option. One example is in biological experiments, where a trapped particle (such as a cell) is non-spherical. Rotational movement of such trapped particles can often be mistaken for lateral shifts, due to a change in its 2D image, the consequence of this being skewed and misleading displacement data for the particle.

Fluorescence microscopy is often used to overcome such issues. When a particle, such as a cell, is marked with a fluorescent dye, internal structures, such as organelles, are no longer visible. Therefore, the cell appears more uniform and opaque, than it would under brightfield microscopy, leading to an increase tracking data quality. The main setback when particle video-tracking with fluorescence microscopy is the significantly reduced light levels, resulting in higher exposure values and hence low tracking frame rates. When using the same CMOS camera as used in brightfield, we were able to track between 20-30 frames per second. This would allow us to calculate the variance of the Brownian motion, however due to the long frame rates, we would not be able to measure the MSD to a high enough standard. In this Chapter we were able to increase the frame rates using either an EMCCD camera or an sCMOS camera.

We compared the performances of the EMCCD and sCMOS cameras discussed previously, using a reduced region of interest and a frame rate of 250 frames per second, and discovered that both cameras agreed at some of the lowest limits of light levels. Also both cameras agreed with a standard CMOS camera using brightfield illumination, operating at a 10 times lower frame rate. Thus using a scientific camera significantly increased tracking data quality. This was at a light level of around 40 photons/pixel. This quality reduced until the particle could no longer be tracked at around 27 photons/pixel, even though the bead could still be imaged. This is useful information for those who are planning biological tracking experiments and want to

make the optimum choice of which camera to use.

In Chapter 4 we used Holographic Optical Tweezers to study microparticles in Low Reynolds number environments, and to consider the possibility of developing non-invasive hydrodynamic trapping. Reynolds number is the ratio between the inertial forces and viscous forces acting on an object. Most organisms live in high Reynolds number environments. However, most water-living bacteria live in low Reynolds number environments, as water is very viscous to microscopic objects, and so viscous forces dominate over the bacterium's inertial forces. Some water-living bacteria have evolved so that they do not need to rely on inertial forces to be able to move, such as cork-screwing motions. However, these techniques are not fully understood physically, as some must involve periodic deformations that break time-reversal symmetry.

We produced a very simple model of how bacteria at low Reynolds number environments may act, where we optically trapped a bead that is also hydrodynamically interacting with another bead. This was done by static optically trapping a probe bead, while driving a holographic optically trapped actuator bead at close proximity. The actuator firstly moves with circular motion, and then with horizontal motion, thus producing two different fluid flows. This was a very simple model of how some micro-swimmers may act under time-varying viscous hydrodynamic forces.

We quickly realised that the time-varying hydrodynamic forces, like those produced from the simple trapped bead in this experiment, were fairly weak, and hence, a more elaborate method of producing the forces was required in order to 'trap' a particle. There is opening research going on to develop specialised microtools for producing hydrodynamic forces capable of trapping particles.

We investigated the video tracking of the probe bead and explored the resulting trajectories that were executed by the probe under the two time varying configurations of the actuator path. We discovered that the probe's movement followed a closed

‘Lissajous-like’ trajectory, while experiencing time-varying oscillating hydrodynamic forces, produced by the actuator bead path.

We also found that these paths broke time-reversal symmetry, by which we mean the path would not be the same if the experiment was happening backwards in time. This is a consequence of the changing balance between the time-varying hydrodynamic force produced by the actuator and the optical restoring force of the static probe trap, that changes with respect to the probe’s position. This information could further aid the growing field of micro-robotics, and deepen our understanding of micro-swimmers and water living micro-organisms.

All of the tracking we had done thus far had involved 2D video tracking. In Chapter 5 we expanded this to video tracking optically trapped beads in real time in three dimensions. Stereomicroscopy allows 3D position tracking data to be retrieved by viewing the sample from different directions. If an object in the sample was to move axially, and is viewed at an angle, there is an observed lateral movement in the corresponding 2D image. By observing this lateral movement, and using parallax calculations, we are able to calculate the axial movement, as well as the lateral movement.

In previous work, instead of viewing the sample from two different angles, the sample was illuminated at two different angles, producing two separate images, which are superimposed in the objective lens. The superimposed images can be separated by placing an SLM in the Fourier plane of the imaging arm and uploading a diffraction grating for each image on its screen.

In Chapter 5, we demonstrated a stereo-microscope with four illumination directions rather than the usual two, allowing us to gain two independent sets of 3D tracking data of an optically trapped bead undergoing brownian motion. This was used to calculate the accuracy of the stereo-microscope. We were able to use this accuracy

measurement to further optimise the stereo-microscope's features, such as the angle of the illumination and exposure time.

We discovered that the optimum illumination polar angle was $\sim 25^\circ$ and azimuthal was 90° . Also, the optimum aperture size for each grating on the SLM was approximately $10\mu\text{m}$, and that camera exposure times larger than $600\mu\text{s}$ were favoured. We compared two independent results that were recorded, and demonstrated a tracking accuracy of better than 2.5% of the range of the bead's motion, in all three dimensions. This 2.5% corresponds to a RMS tracking difference of approximately 5nm; a measurement that was recorded in the z -axis.

The work in all the chapters have led to developments in optimising Optical Tweezers for Tracking and force measurement experiments, and is anticipated to be of major benefit to future work and collaborations.

6.1 Future work

There is much scope for the Cuboid design mentioned in Chapter 2. Due to its small and compact design, it is easily transported and exhibits good stability. There are plans for the Cuboid to be loaned to Exeter University for collaborative work with Dr. David Phillips, who will be investigating the world of micro-tools and micro-robotics. This work will be a continuation of the work mentioned in Chapter 4. There are also opportunities for future collaborations with other research groups at the University of Glasgow, including some in the life sciences

Various future improvements to the Cuboid have been considered. Combining the system with light-sheet or confocal microscopy can be used to remove the out of focus parts of the image, where the limited depth of field becomes problematic. Increasing the depth of field by adding an aperture to the Fourier plane of an imaging arm may

allow the system to be used to reconstruct 3D models of microscopic samples using a radon transform on a sequence of 2D images recorded from different views of the object.

As camera technology is constantly improving, future work in Chapter 3 could include using the very latest, scientific cameras. If camera technology allows us to image at fast enough frame rates, we could track live, instead of tracking pre-recorded video data. This would be a better comparison to the more generic live tracking in the brightfield. It would also be great to apply this technique to a biological experiment where the benefits of improved cell tracking can be realised.

There are already future plans for the work described in Chapter 4, as discussed. This work could help research into life at low Reynolds number environments and micro-robotics, and allow various hydrodynamic systems to be modelled. We could study how multiple time-varying hydrodynamic flows would effect trapped and untrapped particles, and see if, with the right setup of flows, whether it is possible to produce a hydrodynamic trap, for less invasive biological trapping experiments.

We have also discussed ideas for future work into Chapter 5 . We could replace our LED and light guide illumination with a Digital Micro-mirror Device (DMD). This would allows us to rapidly change the illumination angle such that the resulting images could be separated sequentially, without the need for an SLM in the Fourier plane. This would also make the system simpler to align and optimise.

Finally, we could also attempt to combine all the ideas mentioned in the separate chapters into one Stereo-microscope, which can be used to image and track biological samples in fluorescence with the possible use of hydrodynamic traps.

By making use of SLMs and DMDs to shape light, rather than using traditional optical elements, one can create microscope systems capable of multiple imaging and trapping modes with only minimal additional hardware.

Bibliography

- [1] Maria Dienerowitz, Laura V Cowan, Graham M Gibson, Rebecca Hay, Miles J Padgett, and Vernon R Phoenix. Optically trapped bacteria pairs reveal discrete motile response to control aggregation upon cell–cell approach. *Current microbiology*, 69(5):669–674, 2014.
- [2] RR Brau, JM Ferrer, H Lee, CE Castro, BK Tam, PB Tarsa, P Matsudaira, MC Boyce, RD Kamm, and MJ Lang. Passive and active microrheology with optical tweezers. *Journal of Optics A: Pure and Applied Optics*, 9(8):S103, 2007.
- [3] Arthur Ashkin. Forces of a single-beam gradient laser trap on a dielectric sphere in the ray optics regime. *Biophysical journal*, 61(2):569, 1992.
- [4] Scot C Kuo and Michael P Sheetz. Force of single kinesin molecules measured with optical tweezers. *Science*, 260(5105):232–234, 1993.
- [5] R F Hay, G M Gibson, S H Simpson, M J Padgett, and D B Phillips. Lissajous-like trajectories in optical tweezers. *Optics express*, 23(25):31716–31727, 2015.
- [6] Justin E Molloy and Miles J Padgett. Lights, action: optical tweezers. *Contemporary Physics*, 43(4):241–258, 2002.
- [7] Martin Andersson, Ashwin Madgavkar, Maria Stjerndahl, Yanrong Wu, Weihong Tan, Randy Duran, Stefan Nihren, Kamal Mustafa, Kristina Arvidson,

- and Ann Wennerberg. Using optical tweezers for measuring the interaction forces between human bone cells and implant surfaces: System design and force calibration. *Review of Scientific Instruments*, 78(7):074302, 2007.
- [8] GM Gibson, RW Bowman, A Linnenberger, M Dienerowitz, DB Phillips, DM Carberry, MJ Miles, and MJ Padgett. A compact holographic optical tweezers instrument. *Review of Scientific Instruments*, 83(11):113107, 2012.
- [9] Manlio Tassieri, Francesco Del Giudice, Emma J Robertson, Neena Jain, Bettina Fries, Rab Wilson, Andrew Glidle, Francesco Greco, Paolo Antonio Netti, Pier Luca Maffettone, et al. Microrheology with optical tweezers: Measuring the relative viscosity of solutions ?at a glance? *Scientific reports*, 5:srep08831, 2015.
- [10] MP Lee, A Curran, GM Gibson, M Tassieri, NR Heckenberg, and MJ Padgett. Optical shield: measuring viscosity of turbid fluids using optical tweezers. *Optics express*, 20(11):12127–12132, 2012.
- [11] Fiona Watts, Lay Ean Tan, Clive G Wilson, John M Girkin, Manlio Tassieri, and Amanda J Wright. Investigating the micro-rheology of the vitreous humor using an optically trapped local probe. *Journal of Optics*, 16(1):015301, 2013.
- [12] Arthur Ashkin. Applications of laser radiation pressure. *Science*, 210(4474):1081–1088, 1980.
- [13] Arthur Ashkin, JM Dziedzic, JE Bjorkholm, and Steven Chu. Observation of a single-beam gradient force optical trap for dielectric particles. *Optics letters*, 11(5):288–290, 1986.
- [14] Arthur Ashkin, James M Dziedzic, and T Yamane. Optical trapping and manipulation of single cells using infrared laser beams. *Nature*, 330(6150):769–771, 1987.

-
- [15] Arthur Ashkin. Optical trapping and manipulation of neutral particles using lasers. *Proceedings of the National Academy of Sciences*, 94(10):4853–4860, 1997.
- [16] Arthur Ashkin. History of optical trapping and manipulation of small-neutral particle, atoms, and molecules. *IEEE Journal of Selected Topics in Quantum Electronics*, 6(6):841–856, 2000.
- [17] Richard W Bowman and Miles J Padgett. Optical trapping and binding. *Reports on Progress in Physics*, 76(2):026401, 2013.
- [18] Alison Yao, Manlio Tassieri, Miles Padgett, and Jonathan Cooper. Microrheology with optical tweezers. *Lab on a Chip*, 9(17):2568–2575, 2009.
- [19] Alexander B Stilgoe, Timo A Nieminen, Gregor Knöener, Norman R Heckenberg, and Halina Rubinsztein-Dunlop. The effect of mie resonances on trapping in optical tweezers. *Optics express*, 16(19):15039–15051, 2008.
- [20] Arthur Ashkin. Acceleration and trapping of particles by radiation pressure. *Physical review letters*, 24(4):156, 1970.
- [21] Paul Langevin. Sur la théorie du mouvement brownien. *CR Acad. Sci. Paris*, 146(530-533), 1908.
- [22] Graham M Gibson, Jonathan Leach, Stephen Keen, Amanda J Wright, and Miles J Padgett. Measuring the accuracy of particle position and force in optical tweezers using high-speed video microscopy. *Optics Express*, 16(19):14561–14570, 2008.
- [23] Keir C Neuman and Attila Nagy. Single-molecule force spectroscopy: optical tweezers, magnetic tweezers and atomic force microscopy. *Nature methods*, 5(6):491, 2008.

-
- [24] Miles Padgett and Roberto Di Leonardo. Holographic optical tweezers and their relevance to lab on chip devices. *Lab on a Chip*, 11(7):1196–1205, 2011.
- [25] M Reicherter, T Haist, EU Wagemann, and HJ Tiziani. Optical particle trapping with computer-generated holograms written on a liquid-crystal display. *Optics Letters*, 24(9):608–610, 1999.
- [26] Yoshio Hayasaki, Masahide Itoh, Toyohiko Yatagai, and Nobuo Nishida. Non-mechanical optical manipulation of microparticle using spatial light modulator. *Optical review*, 6(1):24–27, 1999.
- [27] David G Grier. A revolution in optical manipulation. *Nature*, 424(6950):810–816, 2003.
- [28] Gregor Thalhammer, Richard W Bowman, Gordon D Love, Miles J Padgett, and Monika Ritsch-Marte. Speeding up liquid crystal slms using overdrive with phase change reduction. *Optics express*, 21(2):1779–1797, 2013.
- [29] J Liesener, M Reicherter, T Haist, and HJ Tiziani. Multi-functional optical tweezers using computer-generated holograms. *Optics Communications*, 185(1):77–82, 2000.
- [30] Jonathan Leach, Kurt Wulff, Gavin Sinclair, Pamela Jordan, Johannes Courtial, Laura Thomson, Graham Gibson, Kayode Karunwi, Jon Cooper, Zsolt John Laczik, et al. Interactive approach to optical tweezers control. *Applied optics*, 45(5):897–903, 2006.
- [31] Veit Elser, I Rankenburg, and P Thibault. Searching with iterated maps. *Proceedings of the National Academy of Sciences*, 104(2):418–423, 2007.
- [32] Roberto Di Leonardo, Francesca Ianni, and Giancarlo Ruocco. Computer generation of optimal holograms for optical trap arrays. *Optics Express*, 15(4):1913–1922, 2007.

-
- [33] Jens-Christian Meiners and Stephen R Quake. Femtonewton force spectroscopy of single extended dna molecules. *Physical Review Letters*, 84(21):5014, 2000.
- [34] Kirstine Berg-Sørensen, Erwin JG Peterman, Tom Weber, Christoph F Schmidt, and Henrik Flyvbjerg. Power spectrum analysis for optical tweezers. ii: Laser wavelength dependence of parasitic filtering, and how to achieve high bandwidth. *Review of scientific instruments*, 77(6):063106, 2006.
- [35] GV Soni, BM Jaffar Ali, Yashodhan Hatwalne, and GV Shivashankar. Single particle tracking of correlated bacterial dynamics. *Biophysical journal*, 84(4):2634–2637, 2003.
- [36] Lucien P Ghislain, Neil A Switz, and Watt W Webb. Measurement of small forces using an optical trap. *Review of Scientific Instruments*, 65(9):2762–2768, 1994.
- [37] Erik Schäffer, Simon F Nørrelykke, and Jonathon Howard. Surface forces and drag coefficients of microspheres near a plane surface measured with optical tweezers. *Langmuir*, 23(7):3654–3665, 2007.
- [38] Inge M Peters, Bart G de Grooth, Juleon M Schins, Carl G Figdor, and Jan Greve. Three dimensional single-particle tracking with nanometer resolution. *Review of scientific instruments*, 69(7):2762–2766, 1998.
- [39] A Pralle, M Prummer, Ernst-Ludwig Florin, EHK Stelzer, JKH Hörber, et al. Three-dimensional high-resolution particle tracking for optical tweezers by forward scattered light. *Microscopy research and technique*, 44(5):378–386, 1999.
- [40] Alexander Rohrbach, Christian Tischer, Dirk Neumayer, Ernst-Ludwig Florin, and Ernst HK Stelzer. Trapping and tracking a local probe with a photonic force microscope. *Review of Scientific Instruments*, 75(6):2197–2210, 2004.

-
- [41] S Keen, J Leach, G Gibson, and MJ Padgett. Comparison of a high-speed camera and a quadrant detector for measuring displacements in optical tweezers. *Journal of Optics A: Pure and Applied Optics*, 9(8):S264, 2007.
- [42] Oliver Otto, Fabian Czerwinski, Joanne L Gornall, Gunter Stober, Lene B Oddershede, Ralf Seidel, and Ulrich F Keyser. Real-time particle tracking at 10,000 fps using optical fiber illumination. *Optics express*, 18(22):22722–22733, 2010.
- [43] Richard W Bowman, Graham M Gibson, Anna Linnenberger, David B Phillips, James A Grieve, David M Carberry, Steven Serati, Mervyn J Miles, and Miles J Padgett. Red tweezers: Fast, customisable hologram generation for optical tweezers. *Computer Physics Communications*, 185(1):268–273, 2014.
- [44] Oliver Otto, Christof Gutsche, Friedrich Kremer, and Ulrich F Keyser. Optical tweezers with 2.5 khz bandwidth video detection for single-colloid electrophoresis. *Review of Scientific Instruments*, 79(2):023710, 2008.
- [45] Christopher D Saunter. Quantifying subpixel accuracy: an experimental method for measuring accuracy in image-correlation-based, single-particle tracking. *Biophysical journal*, 98(8):1566–1570, 2010.
- [46] John C Crocker and David G Grier. Methods of digital video microscopy for colloidal studies. *Journal of colloid and interface science*, 179(1):298–310, 1996.
- [47] Thierry Savin and Patrick S Doyle. Static and dynamic errors in particle tracking microrheology. *Biophysical journal*, 88(1):623–638, 2005.
- [48] Michael K Cheezum, William F Walker, and William H Guilford. Quantitative comparison of algorithms for tracking single fluorescent particles. *Biophysical journal*, 81(4):2378–2388, 2001.

-
- [49] RF Hay, GM Gibson, MP Lee, MJ Padgett, and DB Phillips. Four-directional stereo-microscopy for 3d particle tracking with real-time error evaluation. *Optics express*, 22(15):18662–18667, 2014.
- [50] Vicky Louise Morrison, Martyn John James, Katarzyna Grzes, Peter Cook, David Gavin Glass, Terhi Savinko, Hwee San Lek, Christian Gawden-Bone, Colin Watts, Owain Richard Millington, et al. Loss of beta2-integrin-mediated cytoskeletal linkage reprogrammes dendritic cells to a mature migratory phenotype. *Nature communications*, 5, 2014.
- [51] Glen R Kirkham, Emily Britchford, Thomas Upton, James Ware, Graham M Gibson, Yannick Devaud, Martin Ehrbar, Miles Padgett, Stephanie Allen, Lee D Buttery, et al. Precision assembly of complex cellular microenvironments using holographic optical tweezers. *Scientific reports*, 5, 2015.
- [52] Niall McAlinden, David G Glass, Owain R Millington, and Amanda J Wright. Accurate position tracking of optically trapped live cells. *Biomedical optics express*, 5(4):1026–1037, 2014.
- [53] J El Hobbie, R Jasper Daley, and STTI977 Jasper. Use of nuclepore filters for counting bacteria by fluorescence microscopy. *Applied and environmental microbiology*, 33(5):1225–1228, 1977.
- [54] Joost van Mameren, Mauro Modesti, Roland Kanaar, Claire Wyman, Gijs JL Wuite, and Erwin JG Peterman. Dissecting elastic heterogeneity along dna molecules coated partly with rad51 using concurrent fluorescence microscopy and optical tweezers. *Biophysical journal*, 91(8):L78–L80, 2006.
- [55] Rumelo Amor, Alison McDonald, Johanna Trägårdh, Gillian Robb, Louise Wilson, Nor Zaihana Abdul Rahman, John Dempster, William Bradshaw Amos,

- Trevor J Bushell, and Gail McConnell. Widefield two-photon excitation without scanning: Live cell microscopy with high time resolution and low photobleaching. *PloS one*, 11(1):e0147115, 2016.
- [56] Mark Stanford Robbins and Benjamin James Hadwen. The noise performance of electron multiplying charge-coupled devices. *IEEE Transactions on Electron Devices*, 50(5):1227–1232, 2003.
- [57] Lijian Zhang, Leonardo Neves, Jeff S Lundeen, and Ian A Walmsley. A characterization of the single-photon sensitivity of an electron multiplying charge-coupled device. *Journal of Physics B: Atomic, Molecular and Optical Physics*, 42(11):114011, 2009.
- [58] C Coates, B Fowler, and G Holst. scmos-scientific cmos technology: a high-performance imaging breakthrough. *White paper, Andor Technology, Fairchild Imaging and PCO AG*, page 171, 2009.
- [59] Comparing scmos - compare scmos with other detectors. URL <http://www.andor.com/learning-academy/comparing-scmos-compare-scmos-with-other-detectors>. Accessed: 2017-03-24.
- [60] Graeme Whyte, Graham Gibson, Jonathan Leach, Miles Padgett, Daniel Robert, and Mervyn Miles. An optical trapped microhand for manipulating micron-sized objects. *Optics express*, 14(25):12497–12502, 2006.
- [61] R Di Leonardo, J Leach, H Mushfique, JM Cooper, G Ruocco, and MJ Padgett. Multipoint holographic optical velocimetry in microfluidic systems. *Physical review letters*, 96(13):134502, 2006.
- [62] Silke R Kirchner, Spas Nedev, Sol Carretero-Palacios, Andreas Mader, Madeleine Opitz, Theobald Lohmüller, and Jochen Feldmann. Direct optical

- monitoring of flow generated by bacterial flagellar rotation. *Applied Physics Letters*, 104(9):093701, 2014.
- [63] Spas Nedev, S Carretero-Palacios, SR Kirchner, F Jäckel, and J Feldmann. Microscale mapping of oscillatory flows. *Applied Physics Letters*, 105(16):161113, 2014.
- [64] LA Hough and HD Ou-Yang. Correlated motions of two hydrodynamically coupled particles confined in separate quadratic potential wells. *Physical Review E*, 65(2):021906, 2002.
- [65] Christopher D Mellor, Melissa A Sharp, Colin D Bain, and Andrew D Ward. Probing interactions between colloidal particles with oscillating optical tweezers. *Journal of applied physics*, 97(10):103114, 2005.
- [66] M Atakhorrami, D Mizuno, GH Koenderink, TB Liverpool, FC MacKintosh, and CF Schmidt. Short-time inertial response of viscoelastic fluids measured with brownian motion and with active probes. *Physical Review E*, 77(6):061508, 2008.
- [67] Edward M Purcell. Life at low reynolds number. *Am. J. Phys*, 45(1):3–11, 1977.
- [68] John Happel and Howard Brenner. *Low Reynolds number hydrodynamics: with special applications to particulate media*, volume 1. Springer Science & Business Media, 2012.
- [69] Alfred Shapere and Frank Wilczek. Geometry of self-propulsion at low reynolds number. *Journal of Fluid Mechanics*, 198:557–585, 1989.
- [70] Jens Elgeti, Roland G Winkler, and Gerhard Gompper. Physics of microswimmers-single particle motion and collective behavior. *arXiv preprint arXiv:1412.2692*, 2014.

-
- [71] Ali Najafi and Ramin Golestanian. Simple swimmer at low reynolds number: Three linked spheres. *Physical Review E*, 69(6):062901, 2004.
- [72] Shoji Maruo, Hiroyuki Inoue, et al. Optically driven micropump produced by three-dimensional two-photon microfabrication. 2006.
- [73] Jonathan Leach, Hasan Mushfique, Roberto di Leonardo, Miles Padgett, and Jon Cooper. An optically driven pump for microfluidics. *Lab on a Chip*, 6(6):735–739, 2006.
- [74] DB Phillips, MJ Padgett, S Hanna, Y-LD Ho, DM Carberry, MJ Miles, and SH Simpson. Shape-induced force fields in optical trapping. *Nature Photonics*, 8(5):400–405, 2014.
- [75] Donald L Ermak and JA McCammon. Brownian dynamics with hydrodynamic interactions. *The Journal of chemical physics*, 69(4):1352–1360, 1978.
- [76] Jens Rotne and Stephen Prager. Variational treatment of hydrodynamic interaction in polymers. *The Journal of Chemical Physics*, 50(11):4831–4837, 1969.
- [77] Qiyi Zhang and Xun Xiang. A simple derivation of rotne-prager tensor and hydrodynamic interactions between two spheres. *Acta Physica Polonica B*, 43(1), 2012.
- [78] David B Phillips, Luke Debono, Stephen H Simpson, and Miles J Padgett. Optically controlled hydrodynamic micro-manipulation. In *Proc. SPIE*, volume 9548, page 95481A, 2015.
- [79] Harel Nagar and Yael Roichman. Collective excitations of hydrodynamically coupled driven colloidal particles. *Physical Review E*, 90(4):042302, 2014.

-
- [80] S Box, L Debono, DB Phillips, and SH Simpson. Transitional behavior in hydrodynamically coupled oscillators. *Physical Review E*, 91(2):022916, 2015.
- [81] Jennifer E Curtis, Brian A Koss, and David G Grier. Dynamic holographic optical tweezers. *Optics Communications*, 207(1):169–175, 2002.
- [82] Yohai Roichman, Bo Sun, Allan Stolarski, and David G Grier. Influence of nonconservative optical forces on the dynamics of optically trapped colloidal spheres: the fountain of probability. *Physical review letters*, 101(12):128301, 2008.
- [83] R Di Leonardo, L Angelani, D Dell’Arciprete, Giancarlo Ruocco, V Iebba, S Schippa, MP Conte, F Mecarini, F De Angelis, and E Di Fabrizio. Bacterial ratchet motors. *Proceedings of the National Academy of Sciences*, 107(21):9541–9545, 2010.
- [84] Claudio Maggi, Juliane Simmchen, Filippo Saglimbeni, Jaideep Katuri, Michele Dipalo, Francesco De Angelis, Samuel Sanchez, and Roberto Di Leonardo. Self-assembly of micromachining systems powered by janus micromotors. *Small*, 12(4):446–451, 2016.
- [85] Christian Maurer, Alexander Jesacher, Stefan Bernet, and Monika Ritsch-Marte. What spatial light modulators can do for optical microscopy. *Laser & Photonics Reviews*, 5(1):81–101, 2011.
- [86] MP Lee, GM Gibson, R Bowman, S Bernet, M Ritsch-Marte, DB Phillips, and MJ Padgett. A multi-modal stereo microscope based on a spatial light modulator. *Optics express*, 21(14):16541–16551, 2013.
- [87] MP Lee, GM Gibson, D Phillips, MJ Padgett, and M Tassieri. Dynamic stereo microscopy for studying particle sedimentation. *Optics express*, 22(4):4671–4677, 2014.

-
- [88] Thomas Andrew Waigh. Advances in the microrheology of complex fluids. *Reports on Progress in Physics*, 79(7):074601, 2016.
- [89] Manlio Tassieri, Graham M Gibson, RML Evans, Alison M Yao, Rebecca Warren, Miles J Padgett, and Jonathan M Cooper. Measuring storage and loss moduli using optical tweezers: broadband microrheology. *Physical Review E*, 81(2):026308, 2010.
- [90] Manlio Tassieri, RML Evans, Rebecca L Warren, Nicholas J Bailey, and Jonathan M Cooper. Microrheology with optical tweezers: data analysis. *New Journal of Physics*, 14(11):115032, 2012.
- [91] Kishan Dholakia and Peter Reece. Optical micromanipulation takes hold. *Nano today*, 1(1):18–27, 2006.
- [92] Dino Ott, S Nader, S Reihani, and Lene B Oddershede. Simultaneous three-dimensional tracking of individual signals from multi-trap optical tweezers using fast and accurate photodiode detection. *Optics express*, 22(19):23661–23672, 2014.
- [93] Karel Svoboda, Christoph F Schmidt, Bruce J Schnapp, and Steven M Block. Direct observation of kinesin stepping by optical trapping interferometry. *Nature*, 365(6448):721, 1993.
- [94] Michael Speidel, Lars Friedrich, and Alexander Rohrbach. Interferometric 3d tracking of several particles in a scanning laser focus. *Optics express*, 17(2):1003–1015, 2009.
- [95] Mehdi DaneshPanah and Bahram Javidi. Tracking biological microorganisms in sequence of 3d holographic microscopy images. *Optics express*, 15(17):10761–10766, 2007.

-
- [96] Pasquale Memmolo, Maria Iannone, Maurizio Ventre, Paolo Antonio Netti, Andrea Finizio, Melania Paturzo, and Pietro Ferraro. On the holographic 3d tracking of in vitro cells characterized by a highly-morphological change. *Optics express*, 20(27):28485–28493, 2012.
- [97] Pasquale Memmolo, Andrea Finizio, Melania Paturzo, Lisa Miccio, and Pietro Ferraro. Twin-beams digital holography for 3d tracking and quantitative phase-contrast microscopy in microfluidics. *Optics express*, 19(25):25833–25842, 2011.
- [98] Fook Chiong Cheong, Bo Sun Rémi Dreyfus, Jesse Amato-Grill, Ke Xiao, Lisa Dixon, and David G Grier. Flow visualization and flow cytometry with holographic video microscopy. *Optics express*, 17(15):13071–13079, 2009.
- [99] Zhipeng Zhang and Chia-Hsiang Menq. Three-dimensional particle tracking with subnanometer resolution using off-focus images. *Applied Optics*, 47(13):2361–2370, 2008.
- [100] Sang Joon Lee and Seok Kim. Advanced particle-based velocimetry techniques for microscale flows. *Microfluidics and Nanofluidics*, 6(5):577, 2009.
- [101] F Saglimbeni, S Bianchi, A Lepore, and R Di Leonardo. Three-axis digital holographic microscopy for high speed volumetric imaging. *Optics express*, 22(11):13710–13718, 2014.
- [102] Ivan R Perch-Nielsen, Peter John Rodrigo, and Jesper Glückstad. Real-time interactive 3d manipulation of particles viewed in two orthogonal observation planes. *Optics express*, 13(8):2852–2857, 2005.
- [103] Richard Bowman, Graham Gibson, and Miles Padgett. Particle tracking stereomicroscopy in optical tweezers: control of trap shape. *Optics express*, 18(11):11785–11790, 2010.

-
- [104] Richard Bowman, Daryl Preece, Graham Gibson, and Miles Padgett. Stereoscopic particle tracking for 3d touch, vision and closed-loop control in optical tweezers. *Journal of Optics*, 13(4):044003, 2011.
- [105] Ivan R Perch-Nielsen, Peter John Rodrigo, Carlo Amadeo Alonzo, and Jesper Glückstad. Autonomous and 3d real-time multi-beam manipulation in a microfluidic environment. *Optics express*, 14(25):12199–12205, 2006.
- [106] Kyoo Hyun Kim, Jonghee Yoon, and YongKeun Park. Simultaneous 3d visualization and position tracking of optically trapped particles using optical diffraction tomography. *Optica*, 2(4):343–346, 2015.
- [107] Jeppe S Dam, Ivan R Perch-Nielsen, Darwin Palima, and Jesper Glückstad. Three-dimensional imaging in three-dimensional optical multi-beam micromanipulation. *Optics express*, 16(10):7244–7250, 2008.
- [108] Yiwei Zhang, Graham M Gibson, Rebecca Hay, Richard W Bowman, Miles J Padgett, and Matthew P Edgar. A fast 3d reconstruction system with a low-cost camera accessory. *Scientific reports*, 5, 2015.
- [109] Jeppe Seidelin Dam, Ivan Perch-Nielsen, Darwin Palima, and Jesper Glückstad. Multi-particle three-dimensional coordinate estimation in real-time optical manipulation. *Journal of the European Optical Society-Rapid publications*, 4, 2009.
- [110] Malte Hasler, Tobias Haist, and Wolfgang Osten. Stereo vision in spatial-light-modulator-based microscopy. *Optics letters*, 37(12):2238–2240, 2012.
- [111] DB Phillips, GM Gibson, R Bowman, MJ Padgett, S Hanna, DM Carberry, MJ Miles, and SH Simpson. An optically actuated surface scanning probe. *Optics express*, 20(28):29679–29693, 2012.

-
- [112] C Alpmann, R Bowman, M Woerdemann, M Padgett, and C Denz. Mathieu beams as versatile light moulds for 3d micro particle assemblies. *Optics express*, 18(25):26084–26091, 2010.
- [113] SN Olof, JA Grieve, DB Phillips, H Rosenkranz, ML Yallop, MJ Miles, AJ Patil, S Mann, and DM Carberry. Measuring nanoscale forces with living probes. *Nano letters*, 12(11):6018–6023, 2012.